

Abstract

Title of Thesis: POLYMETALLIC MINERAL DEPOSITS OF THE
SYKESVILLE DISTRICT, MARYLAND: ORE-FORMING
PROCESSES IN THE APPALACHIAN OROGEN

John Michael Wilks, Master of Science, 2015

Thesis Directed by: Professor Philip Candela
Dr. Philip Piccoli
Department of Geology

Questions remain concerning the genesis and geological setting of the ultramafic rock-associated mineralization of the Sykesville District, Maryland, USA, which is located in the mid-Atlantic Appalachians. Best described as a mafic-ultramafic VMS deposit, the ores are polymetallic Fe-Cu-Co-Ni-Zn sulfides hosted within an iron oxide-quartz rock and tectonic mélangé that is everywhere in close proximity to ultramafic rocks. Optical microscopy, EDS, and WDS analyses of minerals in thin sections and epoxy mounts of rocks from drill core were performed to aid in understanding the deposit's formation and defining exploration vectors relevant to similar deposits. Monazite dating has been performed by WDS yielding dates broadly consistent with the Taconian orogeny. The mineralization of the Sykesville District contains textures possibly indicative of seafloor deposition in an environment analogous to an oceanic core complex. These markers may hold promise for identifying the timing, paragenesis, and lithological and mineralogical associations of other Appalachian VMS deposits.

POLYMETALLIC MINERAL DEPOSITS OF THE SYKESVILLE DISTRICT,
MARYLAND: ORE-FORMING PROCESSES IN THE APPALACHIAN OROGEN

by

John Wilks

Thesis submitted to the Faculty of the Graduate School of the
University of Maryland, College Park in partial fulfillment
of the requirements for the degree of
Master of Science
2015

Advisory Committee:
Professor Philip Candela
Professor Sarah Penniston-Dorland
Dr. Philip Piccoli

© Copyright by
John Wilks
2015

Table of Contents

Table of Contents	ii
List of Figures	iii
List of Tables	iv
1. Introduction	1
1.1 Regional Geologic History	2
1.2 The Sykesville Mining District	3
1.3 Recent Study	5
1.4 Mine History	8
2. Volcanogenic Massive Sulfide Deposits: Description, Ore Paragenesis, and Classification	10
2.1 Classification of Mineral Hill	12
3. Methods and Materials	15
3.1 Samples	15
3.2 Electron Probe Microanalysis	19
3.3 Monazite Dating	21
4. Results and Discussion	25
4.1 Mineralogy and Textures	25
4.2 Wavelength Dispersive Analyses	28
4.2.1 Sulfides	28
4.2.2 Tourmaline	34
4.2.3 Chlorite	48
4.2.4 Monazite	54
4.3 Mineral Deposit Analogs	60
4.4 Tectonic Interpretation	61
4.5 Conclusions	64
Appendix	68
Bibliography	118

List of Figures

1.1	Regional Map	2
3.1	Map of Mineral Hill	17
3.2	Drill Core Reproduction	18
4.1	Backscatter Electron Image of Electrum	26
4.2	Tourmaline Micrographs	38
4.3	Al-Fe-Mg Ternary Diagram for MH1 & MH2 Tourmaline	41
4.4	Ca-Fe-Mg Ternary Diagram for MH1 & MH2 Tourmaline	41
4.5	Al-Fe-Mg Ternary Diagram for Tourmaline Aggregates	44
4.6	Pseudo-colored BSE image of Tourmaline & Corresponding WDS Traverse	45
4.7	Al-Fe-Mg Ternary Diagram for Isolate Tourmaline	45
4.8	Al-Fe-Mg Ternary Diagram for MH1 Tourmaline	47
4.9	Fe/(Fe+Mg) in Chlorite Versus Depth	51
4.10	MH2 Fe and Al Variability in Chlorite and Tourmaline Versus Depth	53
4.11	BSE Image of Monazite in Sample MH1-11	55
4.12	Map of Monazite Locations on Sample MH2-17	56
4.13	Box and Whisker Plot of Monazite Dates	58
4.14	Monazite Age Relative to Kunk et al. (2004)'s Cooling Curve	59
A1	Monazite Grain Map of Sample MH1-11	116
A2	Monazite Grain Map of Sample MH2-15a	117

List of Tables

4.1	Representative Mineralogy of MH1 and MH2	27
4.2	Chalcopyrite WDS Analyses	29
4.3	Sphalerite WDS Analyses	30
4.4	Representative Tourmaline WDS Analyses	36
4.5	Representative Chlorite WDS Analyses	50
A1	Mineral Hill Mine	68
A2	Bou Azzer Mine	70
A3	Outokumpu	72
A4	Northern Eastern Metals	74
A5	Southern Eastern Metals	77
A6	Ishkinino	79
A7	Dergamysh	81
A8	Ivanovka	83
A9	Blackbird	85
A10	Limassol Forest	87
A11	Windy Craggy	88
A12	Sphalerite WDS Analyses	91
A13	Chalcopyrite WDS Analyses	92
A14	Tourmaline WDS Analyses	94
A15	Tourmaline WDS Traverse Analyses	100
A16	Chlorite WDS Analyses	102
A17	Monazite WDS Analyses	113
A18	Monazite Ages, Error, Grain Size, and Mineralogical Association	115

SECTION 1: Introduction

The Fe-Cu-Co-Zn-Ni deposits of the Sykesville District in Carroll County, Maryland occur within the eastern portion of the Piedmont province of the Appalachian orogen. Mineralization is hosted by an iron oxide-quartz rock, and is everywhere associated with ultramafic rock. These mineralized zones are hosted by the Cambrian-aged Liberty Complex that comprises the tectonic and sedimentary mélanges of the Morgan Run and Sykesville Formations. According to Candela et al. (1989) limited textural evidence present in rocks from Mineral Hill is consistent with the paragenetic sequence sphalerite-chalcopyrite-pyrite-siegenite. Co and Ni were most likely sourced dominantly from ultramafic rocks, with Cu, Zn, and Mn sourced dominantly from basalt, during the highest temperature stage of sea floor hydrothermal events. The $(\text{Cu}+\text{Zn})/\text{Pb}$ ratios suggest little or no involvement of continental crust, with the system itself perhaps representing the trace of a subducted spreading center proximal to continental crust. The banded iron-oxide quartz rock associated with the ultramafic material appear to be a result of chemical sedimentary processes, and everywhere they are observed, they are in contact with ultramafic rocks or their metasomatic equivalents. In this research, I attempt to better constrain the age and genesis of the deposit by analyzing monazite, tourmaline, and other minerals by EPMA.

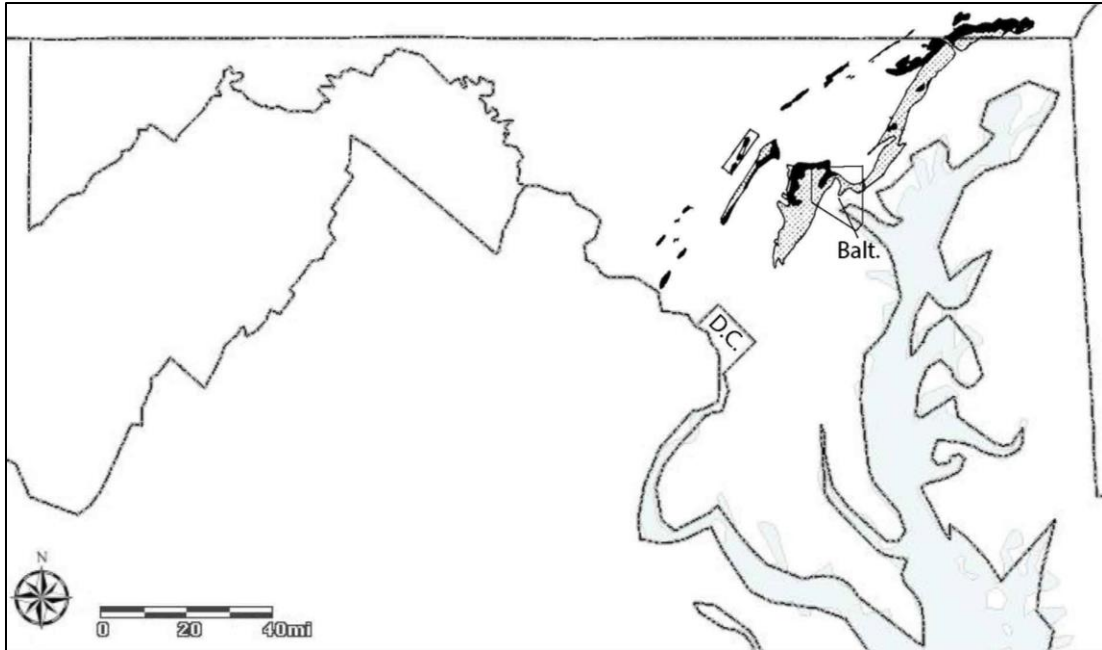


Figure 1.1: Map of the Sykesville District (boxed) and surrounding region. The areas colored in black are areas that contain ultramafic strata, and the shaded regions represent their interpreted extent. Map from the USGS National Map and ultramafic strata from Candela et al., 1989.

1.1 Regional Geologic History

The Appalachian orogen of the eastern North American continent extends from New Brunswick, Canada to Alabama in the United States. The orogen has undergone at least four major phases of mountain building encompassing over one billion years and two Wilson cycles. Approximately 1-1.2 Ga ago during the Grenville Orogeny, Africa collided with what would become the Appalachian region of the United States. This resulted in mountain building and the supercontinent Rodinia. The rifting of Rodinia, and creation of the incipient Iapetus Ocean, occurred ca. 800-850 Ma, and the event is recorded in the Catoctin flood basalts and the associated rift-drift siliciclastic-carbonate sequence of the Chilhowee Group. The drift phase ended ca. 502-419 Ma (Southworth et al., 2006) with the Taconian orogeny, which was the manifestation of the collision between the Chopawamsic/Arvonian volcanic terrane and Laurentia creating the Taconic

Mountains (remnants of which still exist today) and a basin inland of the mountain chain. The host rocks for the Sykesville mineralization formed, and were emplaced, during this orogenic phase. The Taconic Mountains were largely eroded by the time of the Acadian Orogeny ca. 421-395 Ma (Southworth et al., 2006), which obliquely accreted the Avalon terrane onto North America and expanded the Kaskaskia Sea into an epicontinental sea that covered most of North America. The last major stage of mountain building occurred ca. 330-270 with the Alleghanian Orogeny. The Alleghanian Orogeny closed the Iapetus Ocean, again colliding North America and Africa, and created Pangea. This orogeny brought about intense phases of metamorphism and structural deformation of what are now the Blue Ridge and Valley and Ridge provinces. The current drift phase began with the rifting of Pangea in the Jurassic Ma (Southworth et al., 2006).

1.2 The Sykesville Mining District

The ores of the Sykesville District are hosted by the Cambrian-aged Liberty Complex that comprises the Morgan Run and Sykesville Formations. It is important to note that the Sykesville District and Sykesville Formation are distinct, and the mineralization of the Sykesville District is hosted within the Morgan Run Formation. The Morgan Run Formation and Sykesville Formation are separated by the Plummers Island Thrust Fault (Southworth et al., 2006), and there have been several tectonic interpretations of the Liberty Complex. Based on petrographic observations, Muller et al. (1989) proposed that the Morgan Run Formation provided tectonically eroded clasts acting as a source to the Sykesville Formation in an accretionary prism or subduction mélangé. Drake (1989) proposed the Sykesville Formation formed from clasts shed by fault brecciation of the Morgan Run Formation. Kunk et al. (2005) later postulated that

the mélangé of the Sykesville Formation may be a result of subduction trench brecciation with prograde metamorphism occurring due to Taconian Orogeny magmatism. According to Kunk et al. (2005), the Sykesville Formation may represent the hanging wall of the Plummers Island Fault, and retrograde metamorphism may have occurred during the Acadian Orogeny through exhumation of the Sykesville Formation rocks as the Plummers Island Fault was extensionally reactivated. The Morgan Run Formation itself has been interpreted to be composed of the flysch detritus of a foreland basin leading to the creation of a tectonic mélangé of ultramafic and metapelitic material during accretion (Muller et al., 1989). Metamorphism occurred episodically in the form of multiple orogenies and locally may have reached a maximum of upper amphibolite facies (Kunk et al., 2005) during the Devonian Taconian Orogeny. Regional metamorphism can be interpreted as ending after the emplacement of the unmetamorphosed Guilford Intrusive Suite of Maryland, which has been dated to 362 Ma (Aleinikoff et al., 2002). Multiple phases of metamorphism make the depositional environment of the ore difficult to study due to the re-equilibration of minerals and destruction of many primary ore textures in most sulfides.

Mineralization occurs within the Morgan Run Formation which comprises 15 distinct lithologies. The major lithologies include: 1) pelitic schist composed of garnet, chlorite, quartz, magnetite, muscovite, plagioclase, and biotite, 2) quartzofeldspathic schist or metagraywacke, 3) amphibole-epidote quartzite and quartzitic granofels, 4) schistose to granoblastic amphibolite and amphibole schist, and 5) massive to schistose ultramafic rock composed of serpentinite and chlorite-actinolite and chlorite-talc metasomatic zones. The ore bodies were originally reported to be dominantly in the form

of veins, often in clusters and occasionally lenticular in nature. Some ore zones at Mineral Hill and Springfield were traceable for more than 1,000 feet (Heyl and Pearre, 1965). A reinterpretation by Candela et al. (1989) suggests that the sulfide-bearing mineralization occurs in association with exhalative banded iron oxide - quartz rock, and everywhere is in close proximity to ultramafic and metapelitic rocks, and their associated metasomatic blackwall zones. The mineralogy of the ore consists primarily of magnetite (\pm hematite) and quartz with disseminated chalcopyrite, bornite, pyrite, and sphalerite. The ores of the Sykesville District also contain minerals of the linnaeite series of Cu-Co-Ni sulfides that include siegenite and carrollite. There is a well-defined contact between the pelitic and ultramafic rocks represented by a transition from chlorite to actinolite in the blackwall zone (Candela et al., 1989).

1.3 Regional Geology & Recent Study

Contemporary research has investigated the regional deformational and tectonic history of the Maryland and Virginia Piedmont. Aleinikoff et al. (2002) used U/Pb sensitive high-resolution ion microprobe (SHRIMP) and thermal ionization mass spectrometry (TIMS) to analyze zircons from plutons that intrude the Sykesville Formation. From oldest to youngest, the plutons are the Dalecarlia Intrusive Suite, the Falls Church Intrusive Suite, the Georgetown Intrusive Suite, the Kensington Tonalite, and the Norbeck Intrusive Suite, and their ages range from 478 ± 6 Ma to 449 ± 7 Ma.

Following up this isotopic analysis, Schoenborn (2002) proposed, through kinematic analysis, that the Sykesville and Mather Gorge Formations had shared deformational histories. This hypothesis directly contrasts the results of Kunk et al. (2005) who argue the Morgan Run and Sykesville Formations had strongly contrasting

metamorphic histories. In contrast to Schoenborn's kinematic analysis, Kunk et al. (2005) used data collected from $^{40}\text{Ar}/^{39}\text{Ar}$ cooling ages taken from muscovite and amphiboles, zircon overgrowth dating, and fission track dating.

Their data appear to show that the Sykesville Formation experienced accelerated cooling relative to the Morgan Run Formation (their Mather Gorge Formation¹). When the Sykesville formation was at upper amphibolite facies the Morgan Run Formation was at Greenschist facies, and to close the temperature gap the Sykesville Formation had to experience accelerated cooling presumably by way of exhumation in the Devonian. Kunk et al. (2005) contend these data show that the Sykesville and Morgan Run Formations experienced different metamorphic, and thus cooling, histories separated by an estimated 55 Ma before reaching thermal equivalence (as defined by ages calculated using zircon fission track dating of muscovite closure). By assuming the difference in temperature and cooling rate are a function of depth, the 55 Ma difference in thermal history could represent 3-6 km of vertical displacement depending upon the prevailing geotherm.

Their suggestion is inconsistent with the model that the Morgan Run Formation was incorporated into the Sykesville Formation. Due to contrasting metamorphic histories, the authors contend that if clasts of the Morgan Run Formation exist in the Sykesville Formation, they are a product of overthrusting (perhaps akin to fault breccia) and not syngenetic assimilation (Kunk et al., 2005). Such a result is in contrast to prior work done in the area by Muller et al. (1989), Drake (1989), and Drake and Morgan

¹The Mather Gorge Formation can be approximated as the Virginia continuation of Maryland's Morgan Run Formation (Southworth and Burton, 2004), and for simplicity the Morgan Run Formation will be used in lieu of references to the Mather Gorge Formation. The usual regional distinction between the Mather Gorge and Morgan Run Formation is that the Morgan Run Formation is interpreted to overlie the Sykesville Formation north of the Great Falls corridor while the Mather Gorge underlies the Sykesville to the south.

(1981). Muller et al. (1989) performed a petrographic analysis and put forth that the bedrock of the Morgan Run Formation and the clasts and matrix of the Sykesville Formation share a striking correspondence (Drake, 1989) along with sharing various textural similarities. The authors proposed the Morgan Run Formation as a source for the clasts in the Sykesville Formation based on the close spatial relationship between the two formations and the size and character of the clasts in the Sykesville Formation.

Wintsch et al. (2010) refers to the Morgan Run, Sykesville, and Laurel Formations as the composite Potomac Terrane. They used the $^{40}\text{Ar}/^{39}\text{Ar}$ age spectrum method to analyze white mica, K-feldspar, and biotite from the Potomac terrane and the adjacent Westminster terrane in Maryland. The authors develop a cooling curve for the terranes through time, noting near anatectic metamorphic conditions in the Sykesville domain in the Ordovician. They also note the rocks that encompass the Morgan Run Formation and Sykesville Formations reach thermal equilibrium, thereby dating their tectonic assembly, by the Late Devonian. However, there are some anomalies with this study, such as detrital muscovite dated to ~830 Ma never exceeding the 350 °C closure temperature of muscovite. This is anomalous because these muscovite are located in terranes that have all experienced nearly double the closure temperature of muscovite at their peak metamorphic grades.

Horton et al. (2010) produced more evidence supporting a date of ca 479 Ma for the Dalecardia intrusive suite and also found several zircons of Grenville age (1.8-1.0 Ga) in the Sykesville Formation. The latter is consistent with the ideas expressed by Candela et al. 1989 that some continentally sourced material (i.e. from the supercontinent Rodinia) was present in the Morgan Run Formation. Drake and Lytle (1981) argue that

clasts of the Taconian-aged Chopawamsic terrane have also been incorporated into the Sykesville Formation rendering the age of the Chopawamsic Formation as a maximum age limit for the Sykesville Formation. However, the premise that there are clasts of the Chopawamsic Formation in the Sykesville Formation is not well-supported by evidence (Muller et al., 1989).

1.4 Mine History

The following summary of the mining history is modified from Heyl and Pearre (1965). The Mineral Hill, Springfield, Patapsco, and Carroll mines (in order of decreasing total tonnage) in the Sykesville District were mined episodically for more than a century. Production started during the Revolutionary War when copper was the primary ore product and lasted until 1916 when production shifted to specular hematite-quartz rock for ferrosilicon. At its peak during the 1860s, the Mineral Hill Mine employed more than one hundred people. The district is estimated to have produced 7,500 tons of metallic copper over its lifetime. Most of the reported tonnage was from very high grade (15-20%) chalcopyrite and bornite ore. Several thousand tons of specular hematite-quartz rock (\pm magnetite) were also mined, but the amount is unknown. The determination of the volume percent sulfide in the deposit is fraught with uncertainty, however crude estimates can be made based on mine records presented in Heyl and Pearre (1965). They report that the ore produced from the Mineral Hill mine had a minimum of 15% copper. Assuming that all the copper was present as chalcopyrite yields a chalcopyrite concentration in the ore of 45 volume %. Clearly this does not account for the presence of other copper-bearing sulfides or for sulfides that do not contain significant copper. We can consider two limiting cases: one where chalcopyrite is diluted by quartz and one

where chalcopyrite is diluted by magnetite. Given the commonly reported densities of these minerals, a minimum volume percent of chalcopyrite of 34% to 50% in the ore can be calculated. It is likely, therefore, that mined ore at Mineral Hill was semi-massive to massive sulfide (Taylor et al., 1995).

SECTION 2: Volcanogenic Massive Sulfide Deposits: Description, Ore Paragenesis, and Classification

Mineral Hill has been previously classified as an Outokumpu-type Volcanogenic Massive Sulfide deposit (Candela et al., 1989), but the methods for the identification of, and resultant exploration methods for, mineral deposits have changed through time. Volcanogenic Massive Sulfide (VMS) deposits represent a broad class of polymetallic, sulfide-rich ore deposits that are primarily mined for Cu, Zn, Pb, Au, and Ag (all of which may vary greatly in grade both within and between deposits). VMS deposits are found worldwide and range in age from Archean deposits, to incipient deposits in present day areas of rifting (e.g. the Red Sea), and at mid-ocean ridges (e.g. the Rainbow Field Vents) where there is thought to be current mineral deposition and formation (Galley et al., 2007). They are often stratiform due to their occurrence at, or immediately below, the seafloor and can be pod-like, sheet-like, or lens-like accumulations (Shanks and Koski, 2012) of massive sulfides (>60 volumetric % sulfide minerals [Taylor et al., 1995]). The deposits usually occur in areas of tectonic extension, typically back-arc basins and mid-ocean ridges, although they may also form in island arcs². The deposits range in size from less than a ton to supergiant deposits containing more than 1.5 billion tons of ore. The models for their formation usually possess a magmatic heat source that drives fluid convection in tectonically-brecciated or otherwise sheared environments (synvolcanic faults and fissures, etc.). The hot, metal-rich fluids then rise to the seafloor and precipitate minerals after being discharged from the underwater hot springs (Gibson et al., 2007). The mineralization of VMS systems is then typically syngenetic with much of the ore-

² An arc may be considered to be in extension when the subduction rate exceeds the convergence rate, forcing the retreat of the subduction boundary, producing extensional stress.

related material derived from leaching of the footwall. Well-defined alteration zones can be produced surrounding a black smoker vent system, the size and extent of which may be dictated by the permeability of the surrounding lithofacies (Gibson et al., 2007). Many deposits may also contain a volcanoclastic or siliciclastic component, either through column-collapse or as a function of their depositional environment as in epicontinental back-arcs (Shanks and Koski, 2012).

The classification of VMS deposits have evolved through time. One of the first methods of VMS classification was proposed by Sawkins (1976) and utilized the tentative tectonic setting for the deposits. Sangster and Scott (1976) utilized the host-rock lithology. In the 1980s, Cox and Singer (1986) seemed to reconcile the two, and the paradigm for that time was to classify VMS deposits based on mining localities that correlated to specific host-rock lithologies and inferred tectonic setting. For example, the Besshi mining district in Japan gave rise to the Besshi-type deposit with associated siliciclastic-mafic host-rocks in a back-arc setting. Another common method of classifying VMS deposits derives from their base metal content, which is often a function of their host-rock lithology. The classification system used by Barrie and Hannington (1999), which was subsequently modified by Franklin et al. (2005), Galley et al. (2007), Mosier et al. (2009), and Shanks and Thurston (2012), features classifications based on the host lithology of the associated VMS deposit. The base metal classification system of Hutchinson (1973) was iterated upon by Franklin et al. (1981), Large (1992), and still others in subsequent years. However, this technique seems to rely upon extensive coring, sampling, and assaying of a deposit to be a valid means of classification.

The method of classification used here will be taken from Shanks and Thurston (2012) as it represents one of the most recent compendiums on the subject of VMS deposits and their mineral resource assessment. The Shanks and Thurston (2012) classification system was created to improve predictive capacity in field studies and to better associate tectonic setting with lithostratigraphic assemblages. The system uses five designations, each associating lithology to tectonic setting: mafic in mid-ocean ridges or mature intraoceanic back-arcs; pelitic-mafic rocks in sediment-covered back-arcs; bimodal-mafic rocks in rifted intraoceanic volcanic arcs; bimodal-felsic rocks in continental margin arcs and back-arcs; and felsic-siliciclastic rocks in mature epicontinental back-arcs.

2.1 Classification of Mineral Hill

The siliciclastic-mafic type and ultramafic-mafic type deposits are contemporary VMS deposit classifications created by Shanks and Koski (2012). The siliciclastic-mafic type VMS deposits are composed of lithofacies that range from subequal basalt and pelitic sediments to pelite-dominated sequences and roughly correspond to the Cox and Singer (1986) Besshi-type deposit. The usual mode of formation is caused by the intrusion of argillites and mudstones by basaltic sills. The deposits typically form in rifted continental margin arcs or back-arcs (Shanks and Koski, 2012).

The mafic-ultramafic type of Shanks and Koski (2012) is most similar to the Cyprus deposit (ultramafic rocks in mineralized ophiolites) of Cox and Singer (1986), and the typing was formed partially in response to the discovery of Mid-Atlantic Ridge massive sulfides. The mafic-ultramafic type VMS deposit is characterized by mafic-ultramafic suites containing <10 percent sediment that form in intra-oceanic back-arcs,

fore-arc basins, or oceanic ridges. This deposit type is often found in association with ophiolite suites, occasionally pillow basalts, and, more uncommonly, with komatiitic flows (e.g. Kidd Creek) (Barrie and Hannington, 1999). Both siliciclastic-mafic and mafic-ultramafic are thought to be related to ocean-ocean subduction processes (Shanks and Koski, 2012).

The above classifications were designed by Shanks and Koski (2012) to make the types more broadly encompassing in terms of lithology. For example, “siliciclastic-mafic” was chosen to allow for the inclusion of a broad range of graywackes, siltstones, argillites, and other noncarbonate sedimentary rocks. Still, due to the variation inherent to VMS deposits, these types are still not all-encompassing. Therefore if Mineral Hill is not well-categorized by these broader classifications, the more specific VMS deposits, such as the Atlantic-type and Outokumpu-type, may apply.

The somewhat esoteric Atlantic-type deposit originated from Zaykov et al. (2000). The type-locality for this deposit class is located in the Main Uralian fault zone and is characterized by an ultramafic footwall association, high concentrations of Ni and other PGE elements, and high degrees of deformation. They owe their name to modern sulfide mounds, perhaps proto-VMS deposits, forming in serpentinite in the Mid-Atlantic (e.g. Logatchev Field). However, as noted by Herrington et al. (2005), there is a distinct lack of agreement between Russian authors on how Urals deposits are classified, and the authors further propose that the Atlantic-type may be a subcategory of Cyprus VMS deposits.

Somewhat similarly, there has been no clear consensus on classifying the enigmatic VMS deposits of Outokumpu, Finland. To this end, Peltonen et al. (2006)

proposed a new classification: the Outokumpu-type deposit. In the view of the authors, Outokumpu originated by way of mantle plume-derived heating in an ultramafic seafloor environment. The heat and resultant crustal extension created fault conduits for seawater allowed for the seafloor precipitation of a Cu-rich, Pb-poor proto-ore. The proto-ore was eventually obducted onto a continental margin followed by intense carbonation and silicification. This alteration may have mobilized Ni from the peridotite host rock, leading the authors to postulate that Outokumpu and similar deposits are the result of the end member mixing of “(1) A pre-tectonic Cu-rich proto-ore and (2) syntectonic Ni-rich sulphide disseminations in the quartz rocks” (Peltonen et al., 2006). More broadly, the deposit type can also be categorized as an oceanic Cu-Zn-Co-Au VMS deposit, in accordance with the scheme of Fouquet et al. (2010).

Due to the varied nature of its lithostratigraphic components, Mineral Hill could fall in or between several categories of various classification schemes. The issue is then lumping versus splitting, or genetic versus empirical models. The main goal of a genetic model, or the type of model most relevant to exploration, should be to aid in finding other similar deposits. With the goal of a genetic classification in mind, and although Mineral Hill contains notable sedimentary and exhalative components, the deposit is best categorized as a mafic-ultramafic VMS deposit under the scheme of Shanks and Koski (2012). Mineral Hill also bears characteristics of siliciclastic-mafic (Besshi) deposits due to the incorporation of pelitic components in the deposit. However, because the ore horizons are in all observed locations in contact with ultramafic rock and not necessarily the metapelites, the Besshi classification does not apply.

SECTION 3: Methods and Materials

3.1 Samples

This study uses drill core collected by Noranda Explorations, Inc. in 1979. The core was donated to the Maryland Geological Survey (MGS) upon the completion of their project and a portion given subsequently to the University of Maryland. Core was recovered from two holes (Figure 3.1) drilled in close proximity to the Mineral Hill Mine (denoted as MH1 and MH2) and represent a combined length of ~300 m. The core penetrates ore and host rocks dipping at approximately 70° SE (Burke, 1987). Unfortunately, at both locations the drill cores also intersect timbering from mine shafts. The location of the drill cores and a reproduction of the drill core log and the associated legend are shown below in Figure 3.2.

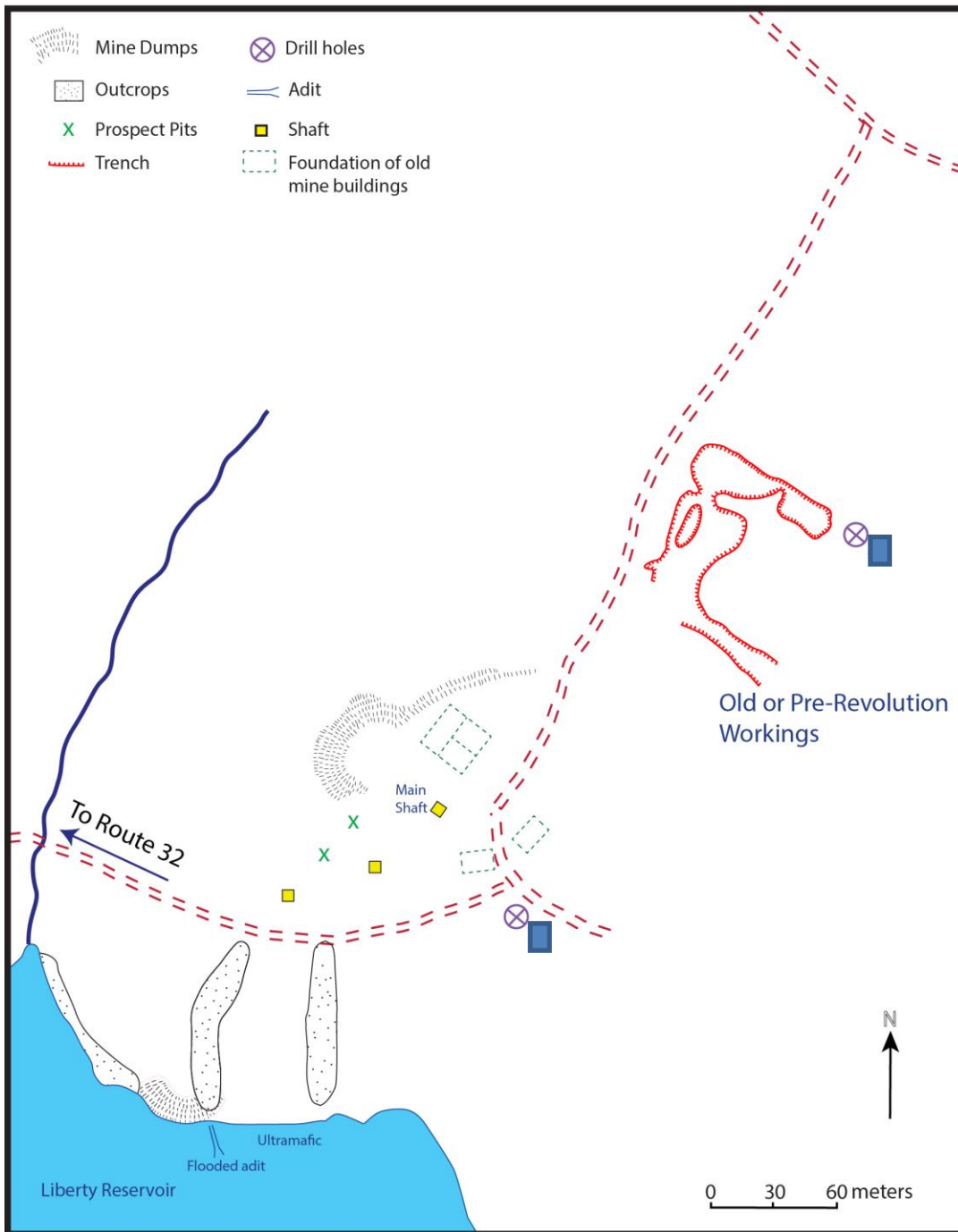
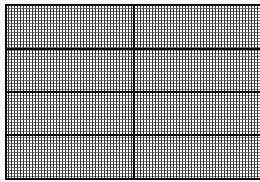
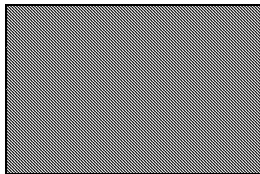


Figure 3.1: Map of the Mineral Hill region modified from Candela et al. (2015). Location of outcrops, surficial mining remnants, and drill core locations at the Mineral Hill mine are displayed.



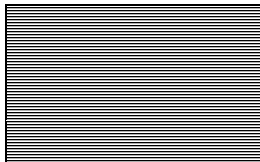
Serpentine + talc + carbonate



Actinolite + talc + chlorite



Chlorite + epidote ± apatite



Muscovite + quartz + biotite +
Chlorite + epidote +
plagioclase
+ tourmaline



Talc + actinolite +
chlorite +
carbonate

Figure 3.2 is a reproduction of the rough drill core log and legend created by Burke (1987) depicting a portion of the Mineral Hill 1 and 2 cores. Depths beneath the surface are labeled in feet as well as the location of timbering.

There were 36 epoxy mounts and 60 thin sections available as part of this study. Thin sections correlate to depths along the drill core, and epoxy mounts come from the Mineral Hill, Springfield, Patapsco, and Carroll Mine tailings as well as the Mineral Hill drill cores.

3.2 Electron Probe Microanalysis

The JEOL JXA-8900R electron probe microanalyzer (EPMA) at the University of Maryland was used to characterize the chemistry of mineral phases. Preliminary study of the thin sections and epoxy mounts began with electron dispersive spectrometry (EDS). EDS, as it is applicable to mineralogy, allows for the qualitative analysis of the characteristic X-rays emitted by solid materials. When the microanalyzer is focused upon a mineral grain, an EDS spectra displays a range of X-ray energies, where peaks at a given energy correspond to specific chemical elements. The X-ray counts generated are a function of the concentration of an element present. Difficulties associated with the use of EDS include the inability to readily identify H, He, and Li, peak (energy) overlap, and large error.

Backscattered electron (BSE) imaging was used to observe mineral grain boundary relationships (e.g. inclusions, zoning) and textures in both thin sections and epoxy mounts. BSE images are a visual display of the relative amount of incident beam electrons scattered away from the sample as a function of their atomic number. It is particularly useful in identifying ore minerals (i.e. those containing metals) as the brighter a sample is in BSE, the higher its mean atomic number is.

Wavelength dispersive spectrometry (WDS) techniques were used for quantitative analysis. WDS analysis improves sensitivity by an order of magnitude relative to EDS,

with detection limits ranging from ~30-300 ppm (highly dependent on the material). The improvements in sensitivity result in better resolution of overlapping X-ray peaks meaning elements that may overlap in EDS, such as Pb and Mo, may be readily identified and differentiated. A difficulty with WDS analysis is the time and skill needed to perform it.

Further, due to uncertainty (e.g. instrumental error, counting statistics), variability in surface topography (e.g. chlorite), and the inability to measure certain elements or molecules (e.g. water), testing criteria were established to maintain data quality. In the case of chlorite, wt % totals of less than 84% were not used. An additional test was employed for chlorite: analyses with >1 wt % potassium were not used due to the possibility of biotite or muscovite intergrowth and contamination. Sulfide analyses with wt % totals of less than 98% were discarded.

During the collection of WDS data, an accelerating voltage of 15 kV was used along with 20 nA cup current for chlorite samples, 15kV and 20 nA cup current for tourmaline samples, and 15 kV and 50 nA cup current for sulfides. The probe beam diameter, which determines the area that is sampled, varied from 1 to 20 microns. An atomic number, absorption, and fluorescence (ZAF) correction factor was used to calculate elemental concentrations. When analyzing tourmaline, Al, Si, B, Fe, F, and Na were standardized on San Luis Potosi tourmaline (buergerite: USGS TSLP), whereas Ca and Mg were standardized on garnet (12442/USGS GTAL), and K on microcline. Mn, Zn, Ti, and Cr were also measured. When analyzing chlorite, Mg and Fe were standardized on hornblende (Engel's Amphibole), and Si and Al were standardized on orthoclase (Benson Mines). Na, Mn, K, Ca, and Ti were also measured. When analyzing

chalcopyrite, Fe, Cu, and S were standardized on FeCuS₂, and pure metal/alloys In, As (InAs), Cd, Ag, Zn, Pb, Sn, Co, and Mn were also measured. When analyzing sphalerite, Zn and S were standardized on synthetic ZnS, and In, As, Cd, Ag, Fe, Pb, Sn, Co, Mn, and Cu were also measured.

3.3 Monazite Dating

Monazite is a dominantly light rare earth element-bearing phosphate that is notable for its high melting and closure temperatures. Monazite incorporates U and Th into its structure while initially excluding significant Pb. By determining the U, Th and Pb concentrations in the monazite, a crystallization/resetting age of the monazite can be determined. As mentioned, monazite has a high closure temperature ~1000°C (Flowers et al., 2005) and is also not readily recrystallized or melted in most sedimentary and crustal environments. Assuming no diffusive gain or loss of U, Th, and Pb the associated mineral age will record the time of formation. However, monazite tends to grow during metamorphism, and as demonstrated by Spear and Pyle (2010) and studies referenced therein, monazite grains in a sample do not generally give a single age, but rather, a continuum of ages lasting the duration of the metamorphic event. One factor that may influence monazite growth is the bulk rock chemistry which may constrain the availability of Y, REE, and phosphate. Another factor is the local transport mechanisms for hydrothermal fluids (e.g. matrix diffusion vs. channelized flow) which may also be affected by the partitioning of strain in the rock (i.e. the stratum's porosity and permeability). Prograde processes such as the diffusive loss of Y in garnet, the stability of xenotime, allanite, and apatite, and crystal growth during metamorphism may adversely affect the accuracy of dating. Retrograde processes may also affect dating by causing

either the growth or dissolution of monazite (Spear and Pyle, 2010; Wing et al., 2003; Kohn and Malloy, 2004; Ayers et al., 1999).

The JEOL JXA-8900R electron probe micro-analyzer was used at the University of Maryland for *in-situ* monazite dating. The monazite grains were first identified in BSE and EDS. Due to the small size of the monazite grains, compositional mapping of elemental domains within the monazite was not performed; not having compositional maps will hinder the efficacy of identifying peak and background interference, as well as negate the possibility of differentiating domain dates. The small size also affects the quality of analysis because some monazites may be smaller than the probe beam diameter resulting in variable amounts of contamination from other phases. The possibility of contamination was accounted for by discarding monazite analyses with wt % totals of less than 90%, as well as the analyses displaying contamination of non-standard elements of 5 wt % or more. Each monazite analysis took approximately 9 minutes with measurement time being a function of count time for Pb. In each analysis, Pb was counted for 240 seconds plus 120 seconds on each background position.

Monazite analysis used an accelerating voltage of 15 kV, a cup current of 200 nA, and a beam diameter of 3 to 5 μm . Th, Si, U, and Pb were standardized on ThSiO_4 , UO_2 , and PbCO_3 , whereas Y, P, and Ce were standardized on YPO_4 and CePO_4 , while Ca was standardized on garnet (12442/USGS GTAL). Quantitative analysis was then performed on each individual grain in addition to measuring La, Nd, S, Si, Sm, Pr, Gd, Dy, and Fe. This study utilized the well-characterized, approximately 500 Ma old GSC-8153 monazite as a quality control check (Reno et al., 2012).

Ages and uncertainty were calculated using a program written in C by Reno et al. (2009). The program uses an age equation based on a modified equation from Montel et al. (1996):

$$Pb = \frac{Th \cdot Ma_{Pb208}}{Ma_{Th232}} (e^{\lambda_{Th232}t} - 1) + \frac{U \cdot Ma_{Pb206}}{Ma_U} \cdot \frac{137.88}{137.88} (e^{\lambda_{U238}t} - 1) + \frac{U \cdot Ma_{Pb207}}{Ma_U} \left(1 - \frac{137.88}{137.88}\right) (e^{\lambda_{U238}t} - 1)$$

where Pb, Th, and U are total element concentrations, Ma is the atomic mass of the element, λ is the decay constant for an isotope and t is time. Microprobe monazite dating uses total U and Pb concentrations, and Th is assumed to be mononuclidic. The calculated age is then a mixture of $^{207}\text{Pb}/^{235}\text{U}$, $^{206}\text{Pb}/^{238}\text{U}$ and $^{208}\text{Pb}/^{232}\text{Th}$ ages, with each contributing to the resultant chemical age based on the concentrations of U and Th in the monazite grain (Reno et al., 2009).

Uncertainty on each individual date was obtained by first calculating the absolute error of each element and then propagating those values through the error equation along with the calculated date and concentration of each element, using the equation derived by Reno et al. (2009):

$$\sigma_t = \sqrt{\frac{\sigma_{Pb}^2 - \left(\frac{A_{Pb208}}{A_{Th232}} \cdot e^{\lambda_{Th232}t} - \frac{A_{Pb208}}{A_{Th232}}\right)^2 \cdot (\sigma_{Pb})^2 - \left[\left(\frac{A_{Pb206}}{A_U} \cdot \frac{137.88}{137.88} \cdot e^{\lambda_{U238}t} - \frac{A_{Pb206}}{A_U} \cdot \frac{137.88}{137.88}\right) + \left(\frac{A_{Pb207}}{A_U} \cdot \left(1 - \frac{137.88}{137.88}\right) \cdot e^{\lambda_{U238}t} - \frac{A_{Pb207}}{A_U} \cdot \left(1 - \frac{137.88}{137.88}\right)\right)^2 \cdot \sigma_U^2}{\left(\frac{A_{Pb208}}{A_{Th232}} \cdot e^{\lambda_{Th232}t} \cdot Th \cdot \lambda_{Th232} - \frac{A_{Pb206}}{A_U} \cdot \frac{137.88}{137.88} \cdot e^{\lambda_{U238}t} \cdot U \cdot \lambda_{U238} + \frac{A_{Pb207}}{A_U} \cdot \left(1 - \frac{137.88}{137.88}\right) \cdot e^{\lambda_{U238}t} \cdot U \cdot \lambda_{U235}\right)^2}}$$

where A is atomic mass of an isotope or element, λ is the associated decay constant, σ is the error on a quantity, and t is time. Th, U, and Pb all represent element concentrations

in ppm. Data tables of monazite composition, age, and uncertainty are reported in the appendix (Tables A17-A18).

SECTION 4: Results and Discussion

4.1 Mineralogy and Textures

When petrographic studies were performed by Candela et al. (1989), BSE and EDS technology was not available on the instrument used at that time. Moreover, for particular minerals that undergo solid solution, such as the locally abundant linnaeite mineral group, EPMA is a practical solution to observing and recording accurate compositional variance. In this study, examination of thin sections previously prepared from drill core were examined first by polarized light microscopy (PLM), and then by BSE and EDS techniques. Consequently, some new phases were identified by EPMA in the course of this study. Further, more extensive EPMA analysis by WDS was performed to augment the data collected in the previous study.

The results of the combined PLM and EDS analysis of mineral phases is summarized in Tables 4.1a-b. The results of select thin sections and epoxy mounts from the MH1 and MH2 cores are in good agreement with prior mineralogical and petrographic analysis performed by Burke (1987). Several additional minerals have been noted such as hessite, electrum, monazite, allanite, and arsenopyrite. These trace minerals allow for a more complete comparison of Mineral Hill to similar mineral deposits elsewhere. For example, the silver telluride hessite has also been found in a variety of VMS deposits in the Southern Urals (Herrington et al., 1998). Therefore, its occurrence at Mineral Hill is not unusual given the former.

Flakes of native gold were found in outcrops of iron oxide - quartz rock by Heyl and Pearre (1965), and this is the only report of gold from the peer-reviewed literature that we have found. Electrum was identified in two thin sections from drill core MH2,

and an example is shown in Figure 4.1. The electrum is the first documented modern report of gold and silver minerals at Mineral Hill.

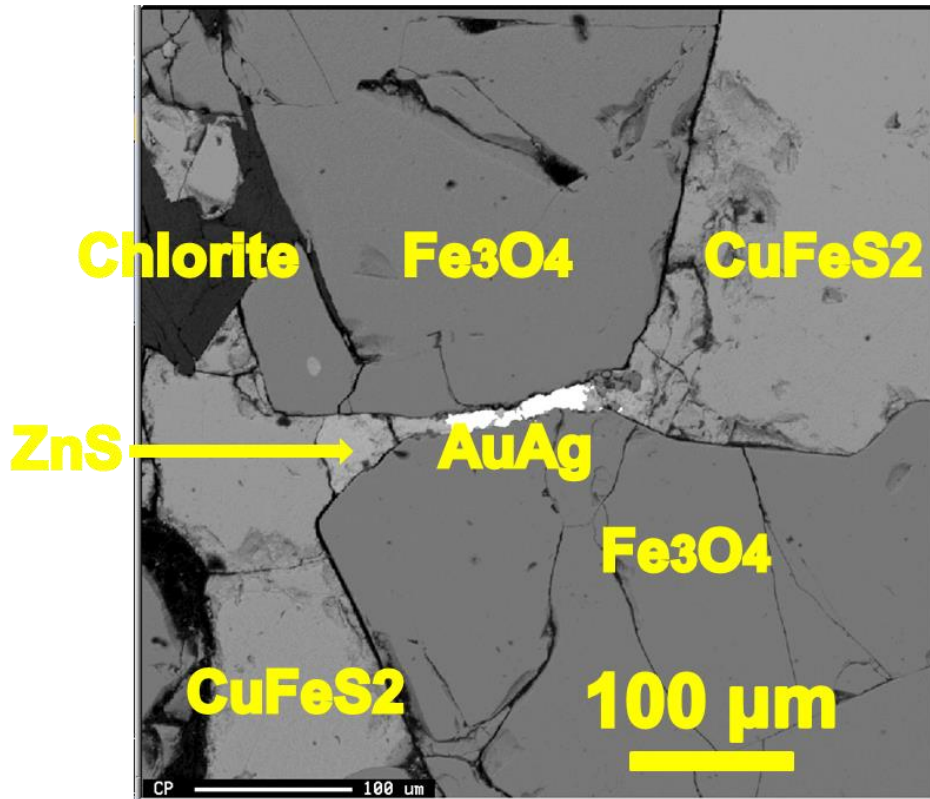


Figure 4.1: Backscattered electron image of a region of sample MH2-06 showing an area with a sulfides and magnetite-rich domain, with a small amount of intergranular electrum.

Distance From Surface (m)		72	75	77	79.5	85
Slide		MH1-13	MH1-24	MH1-30	MH1-32	MH1-45
Silicates	Quartz					
	Talc					
	Chlorite					
	Biotite					
	Plagioclase					
	Muscovite					
	Garnet					
	Epidote					
	Serpentine					
	Actinolite					
Carbonates	Dolomite					
Oxides	Magnetite					
	Ilmenite					
	Chromite					
Sulfides	Pyrite					
	Arsenopyrite					
	Chalcopyrite					
	Bornite					
	Sphalerite					
REE	Monazite					
	Allanite					
	Apatite					
Misc	Zircon					
	Tourmaline					

Distance From Surface (m)		58	61	64	65	66
Slide		MH2-33	MH2-43	MH2-06	MH2-11	MH2-15
Silicates	Quartz					
	Talc					
	Chlorite					
	Biotite					
	Muscovite					
	Plagioclase					
	Epidote					
	Serpentine					
	Actinolite					
	Carbonates	Dolomite				
Oxides	Magnetite					
	Ilmenite					
	Chromite					
Sulfides	Pyrite					
	Chalcopyrite					
	Sphalerite					
	Siegenite					
REE	Monazite					
	Allanite					
	Apatite					
Misc	Zircon					
	Hessite (Ag₂Te)					
	Electrum (AuAg)					
	Tourmaline					

Table 4.1a-b: Summary of mineralogical data obtained by PLM and EDS of thin sections taken from the MH1 core on the left (Table 4.1a) and MH2 drill core on the right (Table 4.1b). The colors represent various mineral families (silicates, oxides, etc.) and those containing rare earth elements (REE). Minerals that were not identified by Burke (1987) are in bold.

4.2 Wavelength Dispersive Analyses

4.2.1 Sulfides

WDS traverses of chalcopyrite (Table 4.2) and sphalerite (Table 4.3) grains were performed to analyze mineral chemistry and to check for chemical zoning. Although no zoning was observed among the elements analyzed, there were chemical trends between sample sites best demonstrated by cadmium in sphalerite. The lack of zoning may indicate the minerals were in equilibrium in their depositional environment post-precipitation.

Sample	Fe	In	S	As	Cd	Ag	Zn	Pb	Cu	Sn	Co	Mn	Total
MH2Y5-1	30.09	0.00	34.15	0.00	0.00	0.02	0.02	0.10	35.43	0.01	0.02	0.00	99.85
MH2Y5-3	30.63	0.00	34.46	0.00	0.00	0.02	0.02	0.09	35.21	0.01	0.03	0.00	100.48
MH2Y5-2 [†]	31.04	0.00	34.57	0.00	0.00	0.02	0.02	0.09	35.28	0.01	0.03	0.00	101.07
MH2Y5-2 [†]	30.97	0.01	34.69	0.00	0.01	0.01	0.02	0.10	35.31	0.01	0.04	0.00	101.15
MH2Y5-2 [†]	31.08	0.00	34.49	0.00	0.00	0.02	0.03	0.09	35.27	0.00	0.02	0.00	101.00
MH2Y5-2 [†]	30.92	0.00	34.45	0.00	0.01	0.03	0.03	0.09	35.35	0.01	0.03	0.00	100.92
SpringX2-1	30.79	0.00	34.18	0.00	0.00	0.02	0.03	0.09	35.13	0.01	0.03	0.00	100.28
SpringX2-1	30.64	0.01	34.27	0.00	0.00	0.00	0.04	0.09	35.32	0.00	0.03	0.00	100.41
MH2-06-1	29.53	0.00	33.16	0.00	0.00	0.01	0.00	0.09	35.40	0.02	0.04	0.00	98.26
MH2-06-2 [†]	31.05	0.00	34.37	0.00	0.00	0.06	0.03	0.09	35.20	0.00	0.03	0.00	100.83
MH2-06-2 [†]	30.95	0.01	34.20	0.00	0.00	0.06	0.02	0.10	35.19	0.00	0.03	0.00	100.57
MH2-06-2 [†]	30.89	0.00	34.52	0.00	0.00	0.05	0.03	0.09	35.26	0.00	0.04	0.01	100.89
MH2-06-2 [†]	30.93	0.01	34.47	0.01	0.00	0.01	0.02	0.09	35.42	0.01	0.03	0.00	100.99
MH2-06-2 [†]	30.87	0.01	34.21	0.01	0.00	0.01	0.03	0.11	35.20	0.01	0.04	0.00	100.48
MH2-06-2 [†]	30.69	0.00	34.19	0.01	0.00	0.03	0.02	0.12	35.31	0.00	0.03	0.00	100.41
MH2-06-2 [†]	30.74	0.00	34.24	0.00	0.00	0.00	0.02	0.08	35.41	0.01	0.03	0.01	100.55
MH1-32-1	30.32	0.00	34.01	0.00	0.00	0.01	0.03	0.09	35.12	0.00	0.03	0.00	99.62
MH1-32-2	30.14	0.01	33.85	0.00	0.00	0.00	0.02	0.10	35.20	0.00	0.03	0.00	99.37
MH1-32-3	30.40	0.00	33.96	0.02	0.00	0.00	0.03	0.10	35.52	0.00	0.04	0.00	100.08
MH1-32-4	30.27	0.01	33.92	0.00	0.00	0.00	0.05	0.10	35.32	0.00	0.04	0.00	99.70
MH1-32-5	30.22	0.01	33.84	0.00	0.00	0.00	0.05	0.10	35.20	0.01	0.03	0.00	99.45

Table 4.2: Composition of chalcopyrite from four samples: two epoxy mounts and two thin sections from Mineral Hill (MH2-06, MH1-32, MH2Y5) and the Springfield mine tailings (SpringX2). [†] indicates a traverse. The measurements were collected using quantitative WDS analysis, and the tables show weight percentages for various elements in chalcopyrite.

Sample	Fe	In	S	As	Cd	Ag	Zn	Pb	Cu	Sn	Co	Mn	Total
MH2Y5-1	2.09	0.00	31.58	0.00	8.04	0.03	55.41	0.06	1.45	0.00	0.06	0.00	98.72
MH2Y5-1	2.48	0.00	31.53	0.00	7.85	0.02	55.31	0.09	1.92	0.00	0.04	0.00	99.23
MH2Y5-2	1.90	0.00	31.28	0.00	8.72	0.01	56.12	0.07	1.24	0.00	0.04	0.00	99.38
MH2Y5-4	4.52	0.03	32.37	0.00	5.01	0.05	54.14	0.08	5.67	0.00	0.02	0.01	101.90
MH2Y5-4	1.84	0.00	31.54	0.00	8.90	0.00	57.08	0.05	1.27	0.00	0.05	0.00	100.72
MH2Y5-4	1.35	0.01	31.84	0.00	7.02	0.02	58.97	0.07	0.84	0.03	0.04	0.01	100.18
MH2Y5-5	1.54	0.00	31.52	0.01	7.54	0.09	58.06	0.07	0.93	0.00	0.04	0.00	99.79
SpringX2-1	5.91	0.01	32.92	0.00	0.12	0.00	58.65	0.07	0.06	0.01	1.05	0.15	98.95
SpringX2-1	5.74	0.00	32.79	0.00	0.12	0.00	58.90	0.08	0.03	0.00	1.01	0.14	98.81
SpringX2-2	6.56	0.01	33.25	0.02	0.14	0.00	57.73	0.07	0.17	0.02	1.05	0.16	99.18
SpringX2-2	6.91	0.00	33.57	0.00	0.15	0.00	56.18	0.05	3.27	0.01	0.77	0.06	100.98
SpringX2-4	7.05	0.01	33.17	0.00	0.13	0.01	56.88	0.08	1.60	0.01	1.07	0.13	100.14
SpringX2-5	4.51	0.00	32.66	0.01	0.11	0.00	59.74	0.08	0.16	0.01	0.81	0.05	98.13
SpringX2-7	6.73	0.00	32.95	0.01	0.13	0.00	58.07	0.07	0.21	0.01	1.09	0.14	99.40
SpringX2-8	6.50	0.00	32.94	0.00	0.13	0.00	58.31	0.08	0.21	0.00	1.03	0.15	99.36
SpringX28	5.68	0.01	33.00	0.01	0.12	0.00	59.47	0.07	0.06	0.01	1.05	0.14	99.62
SpringX2-9	6.32	0.01	33.30	0.00	0.12	0.00	58.56	0.07	0.08	0.00	1.04	0.16	99.67
SpringX2-10	6.29	0.00	33.29	0.00	0.12	0.00	59.08	0.09	0.06	0.01	1.06	0.16	100.15
SpringX2-1	7.53	0.00	35.73	0.00	0.09	0.00	52.24	0.05	1.72	0.01	1.00	0.15	98.51
MH2-06-1	1.01	0.00	31.74	0.04	6.12	0.01	60.19	0.07	0.58	0.00	0.08	0.01	99.85
MH2-06-2	1.08	0.00	32.09	0.00	5.21	0.00	60.92	0.07	0.62	0.00	0.18	0.00	100.16
MH2-06-3	0.93	0.00	31.82	0.00	5.27	0.00	60.77	0.06	0.56	0.00	0.19	0.00	99.61
MH2-06-4	1.02	0.00	32.01	0.00	6.01	0.01	60.11	0.05	0.52	0.00	0.06	0.00	99.80
MH2-06-5	0.64	0.00	31.95	0.00	6.11	0.00	60.57	0.05	0.28	0.00	0.05	0.00	99.67
MH2-06-6	1.14	0.00	31.85	0.00	6.72	0.01	59.65	0.05	0.67	0.00	0.06	0.00	100.15
MH2-06-7	1.64	0.00	31.69	0.00	7.74	0.01	58.24	0.04	1.04	0.00	0.04	0.00	100.44
MH1-32-1	5.79	0.00	32.66	0.00	0.30	0.00	59.13	0.07	0.29	0.00	0.32	0.08	98.65

MH1-32-2	5.65	0.01	32.72	0.00	0.31	0.00	59.25	0.08	0.28	0.00	0.30	0.07	98.66
MH1-32-3	5.95	0.00	32.70	0.00	0.29	0.00	58.81	0.07	0.83	0.00	0.25	0.05	98.95
MH1-32-4	5.33	0.00	32.73	0.00	0.25	0.00	59.66	0.07	0.10	0.00	0.51	0.08	98.76
MH1-32-5	6.31	0.00	33.04	0.00	0.32	0.00	58.06	0.05	0.89	0.00	0.28	0.05	99.00

Table 4.3: The table displays chemical composition (WDS) in weight percent of sphalerite from samples MH2-06, MH1-32, MH2Y5) and the Springfield mine tailings (SpringX2). From an original 66 data points, 53 were used using criteria described in the Electron Probe Microanalysis section.

The chalcopyrite contains up to 1,000 ppm Pb, although there is no Pb-rich phase noted at Mineral Hill or the Sykesville District, as well as several hundred ppm Co, Ag, and Zn. Sphalerite from the same samples that contained the chalcopyrite contain comparable amounts of Pb, however, there appears to be a spatial component to Co and Cd. Cd and Co are both elevated in MH2 and occur in concentrations of up to 8 wt % and 1100 ppm, respectively. Although cadmium substitutes isostructurally for Zn in sphalerite, 8 wt % cadmium in sphalerite is above average. No cadmium-bearing phase (e.g. greenockite) was noted. This differential enrichment appears to be at the cost of Fe and Mn, both of which are elevated relative to Co and Cd at Springfield and MH1. Sphalerites with high cadmium concentrations occur as small grains usually enveloped in a chalcopyrite matrix. In the MH1 core this chalcopyrite-sphalerite assemblage forms along the contact between metasomatized ultramafic rock and metasomatized pelitic rock (chlorite and actinolite zones respectively). A review by Jolly and Heyl (1968) studies of sphalerite from Kentucky, Tennessee, and the Appalachian Zinc deposits record maximum concentrations of cadmium in sphalerite of approximately 2 wt %. The review by Schwartz (2000) includes a mean concentration of cadmium in sphalerite from 86 VMS deposits of up to 1 wt %. Dobbe (1991) recorded Cd in sphalerite concentrations at Tunaberg, Sweden of up to 12.1 wt %. Tunaberg is part of the Bergslagen District and thought to have formed by exhalative processes, although the district's mode of formation has not been resolved and may not be VMS-related. Dobbe also noted Ross Mine in Ontario, Canada (part of the Timmins District, and therefore not a VMS deposit) had sphalerites with cadmium concentrations of up to 9 wt %.

Schwartz (2000) studied the thermodynamics of cadmium partitioning between sphalerite and aqueous solutions of massive sulfide and MVT deposits. Schwartz suggested that a number of variables, including temperature, pH, and chloride activity influence the distribution coefficient (K) of Cd in sphalerite: $K_{(ZnS,CdS)} = \frac{a_{\Sigma Zn(aq)}/a_{\Sigma Cd(aq)}}{a_{ZnS(s)}/a_{CdS(s)}}$ where $a_{\Sigma Zn(aq)}$ and $a_{\Sigma Cd(aq)}$ denote the sum of the activities of aqueous Zn and Cd species, respectively. Due to differences between the strength of the various chloride and sulfide complexes of the two cations, Schwartz suggests that the ΣS_{Red} (total activity of reduced sulfur) and pH are inversely correlated with the distribution coefficient of cadmium, whereas temperature (in the presence of complexing agents) and the Cd/Zn ratio of the fluid are directly correlated. Variations in Cd/Zn of sphalerite could then be due to variances in the depositional environments between MH1 and MH2.

The case may be that sphalerite and chalcopyrite at Mineral Hill did not come from the same fluid, and the sphalerite-in-chalcopyrite texture is a result of incomplete replacement caused by zone refining (as opposed to exsolution). In the process of zone refining higher temperature fluids at the bottom of a sulfide lens typically precipitate chalcopyrite (i.e. copper) at the base or interior of the lens while sphalerite (i.e. zinc) is remobilized and precipitated progressively outward. Sphalerite occurs paragenetically early at Mineral Hill (Candela et al., 1989), and that order is typical of many VMS deposits. At Mineral Hill the high-cadmium sphalerite may then be a byproduct of incomplete replacement by chalcopyrite. Consider the case of a late stage, high temperature, high hydrothermal fluid. Such a fluid could precipitate chalcopyrite while creating conditions favorable for cadmium partitioning with sphalerite. The fluid would react with sphalerite to mobilize the majority elsewhere in the deposit, but assuming there

is incomplete replacement, the remnant sphalerite would become enriched in cadmium as it equilibrates with the fluid.

The local variation in cadmium abundance in the MH1 and MH2 cores is harder to explain and could be the result of a number of factors. Assuming the sphalerite from both locations are roughly coeval, in addition to the factors influencing $K_{(ZnS,CdS)}$ listed prior, chemical variation resulting from deposit structure (e.g. location in a sulfide lens, depth of deposition, proximity to the footwall, etc), morphological features (e.g. vein size), and a host of other factors could all influence cadmium abundance in the ore fluid on a smaller scale. Due to the complicated stratigraphic relationships at Mineral Hill, complex metamorphic history, and the limited data available, defining the cause for the spatial relationship is beyond the scope of this paper.

4.2.2 Tourmaline

When present, tourmaline is commonly analyzed in ore deposits to aid in petrologic and paragenetic characterization. Tourmaline is a piezoelectric, rhombohedral borosilicate of the generalized structural formula $(X)(Y_3)(Z_6)T_6O_{18}(BO_3)_3(V)_3W$ (Dutrow and Henry, 2011). The mineral supports a wide array of solid solution. Commonly Na^{1+} and Ca^{2+} occupy the X-site, Fe^{2+} and Mg^{2+} occupy the Y-site, Al^{3+} occupies the Z-site, Si^{4+} occupies the T-site, and OH^- and O^{2-} occupy the V-site, and O^{2-} , OH^- , and F^- occupy the W-site. Schorl-dravite, with variation along the $FeMg_{-1}$ exchange vector, and schorl-elbaite, with variation along the $LiAlFe^{+2}_{-2}$ exchange, are some of the most commonly found natural tourmalines and are thus variations in common tourmaline can be represented on a ternary Fe-Mg-Li diagram.

The tourmaline family of minerals has been used as a means of fingerprinting ore deposits in exploration (Slack and Coad, 1989; Slack, 1996; Slack and Trumbull, 2011), and more generally as a means of geochemically recording its environment of formation, (Henry and Guidotti, 1985, Henry and Dutrow, 1996, van Hinsberg et al., 2011(a), van Hinsberg et al., 2011(b)) usually by way of its characteristic zoning. This zoning is typically maintained through time as diffusion rates for major and trace elements are negligible at temperatures beneath 700° (Henry and Dutrow, 1996).

The formula for a representative selection of tourmaline from MH1 and 2 (Table 4.4) were calculated using a Microsoft Excel™ spreadsheet developed by Selway and Xiong and is available at <http://www.open.ac.uk/earth-research/tindle/AGTWebPages/AGTSoft.html>. The tourmaline are dominantly dravite-schorl solid solution in the alkali group of Hawthorne and Henry (1999). Although the tourmaline shows a very wide compositional range in Fe/(Fe+Mg) ratios of 0.07-0.87, nearly endmember dravite and schorl, the average concentration is 0.44. Ca is not prevalent, yielding Na/Ca+Na concentrations of 0.63-0.99 with an average of 0.83. The tourmaline are often both chemically and optically zoned (teal blue cores to green rims) with most of the variation along the Y-site MgFe₁ exchange vector. In the MH2 core, the tourmaline forms as either: A) coarse, intergrown, or pod-like aggregates confined to particular layers (Figure 4.2e-f); or B) fine, disseminated grains (Figure 4.2a), which may also occur in small stringers (Figure 4.2b). In the MH1 core, the tourmaline share a more uniform morphology and occur as isolated, rounded, <50 µm grains in which zoning cannot be easily detected optically or on BSE images (Figure 4.2c-d).

Sample Position	MH1-03-1	MH1-19-4		MH1-14-2		MH1-13-2		MH1-07-1		MH1-43-1	MH2-15a-5		MH2-43-5		MH2-17-1		MH2-15b-1	
	Grain	Core	Rim	Core	Rim	Core	Rim	Core	Rim	Grain	Core	Rim	Core	Rim	Core	Rim	Core	Rim
SiO ₂	34.71	35.30	35.08	34.08	35.27	35.51	35.02	34.22	31.73	35.30	35.49	34.66	35.00	35.89	35.31	35.34	35.42	35.15
TiO ₂	0.60	0.13	0.46	0.58	0.40	0.28	0.47	0.36	0.42	0.28	0.06	0.59	0.95	0.42	0.13	0.43	0.42	0.58
Al ₂ O ₃	32.68	33.60	32.29	30.74	33.03	33.39	32.28	32.22	29.81	33.17	33.67	30.24	33.20	32.59	32.33	31.59	32.15	31.24
Cr ₂ O ₃	0.03	0.06	0.04	0.01	0.01	0.01	0.01	0.01	0.02	0.11	0.00	0.02	0.01	0.00	0.01	0.00	0.03	0.01
FeO	9.59	9.15	8.40	8.80	7.08	9.53	8.86	6.43	6.76	5.77	5.18	9.05	7.56	6.50	7.86	7.20	6.60	8.25
MgO	5.38	5.10	6.69	6.74	7.43	5.12	6.29	7.26	7.27	7.75	6.94	5.95	5.03	7.09	5.52	6.85	7.13	6.24
CaO	0.95	0.03	0.67	1.04	1.10	0.26	0.92	0.86	0.88	0.50	0.37	0.51	0.36	0.82	0.58	1.02	1.02	0.80
MnO	0.03	0.00	0.04	0.02	0.02	0.02	0.03	0.05	0.04	0.08	0.02	0.01	0.03	0.02	0.01	0.04	0.03	0.03
ZnO	0.03	0.02	0.00	0.02	0.05	0.03	0.01	0.04	0.04	0.45	0.01	0.01	0.02	0.03	0.03	0.03	0.02	0.03
Na ₂ O	1.66	1.52	2.00	1.79	1.71	1.80	1.84	1.71	1.58	2.09	1.61	2.18	1.94	1.80	1.74	1.91	1.92	2.00
K ₂ O	0.02	0.04	0.05	0.08	0.05	0.02	0.02	0.01	0.02	0.05	0.03	0.03	0.04	0.02	0.03	0.02	0.01	0.02
F	0.27	0.00	0.20	0.19	0.34	0.17	0.23	0.32	0.47	0.17	0.00	0.00	0.16	0.08	0.00	0.03	0.00	0.00
H ₂ O*	3.47	3.60	3.52	3.43	3.50	3.55	3.50	3.39	3.10	3.57	3.61	3.50	3.52	3.61	3.56	3.58	3.62	3.57
B ₂ O ₃ *	10.42	10.43	10.48	10.20	10.60	10.51	10.46	10.27	9.64	10.58	10.46	10.14	10.42	10.57	10.32	10.41	10.49	10.34
Li ₂ O*	0.04	0.00	0.00	0.00	0.00	0.00	0.01	0.00	0.00	0.00	0.09	0.08	0.30	0.14	0.18	0.17	0.17	0.14
Total	99.87	98.99	99.93	97.70	100.59	100.20	99.95	97.17	91.77	99.86	97.53	96.96	98.56	99.55	97.61	98.62	99.00	98.39
Structural formulae based on 31 anions (O ²⁻ , OH, F)																		
T: Si	5.79	5.88	5.82	5.81	5.78	5.87	5.82	5.79	5.72	5.80	5.90	5.94	5.84	5.90	5.95	5.90	5.87	5.91
Al	0.21	0.12	0.18	0.19	0.22	0.13	0.18	0.21	0.28	0.20	0.10	0.06	0.16	0.10	0.05	0.10	0.13	0.09
Z: Al	6.00	6.00	6.00	5.99	6.00	6.00	6.00	6.00	6.00	6.00	6.00	6.00	6.00	6.00	6.00	6.00	6.00	6.00
Y: Al	0.21	0.48	0.13	0.00	0.16	0.38	0.14	0.21	0.06	0.22	0.49	0.05	0.36	0.22	0.36	0.11	0.15	0.10
Ti	0.08	0.02	0.06	0.07	0.05	0.03	0.06	0.05	0.06	0.03	0.01	0.08	0.12	0.05	0.02	0.05	0.05	0.07
Cr	0.00	0.01	0.01	0.00	0.00	0.00	0.00	0.00	0.00	0.01	0.00	0.00	0.00	0.00	0.00	0.00	0.00	0.00
Mg	1.34	1.27	1.66	1.70	1.81	1.26	1.56	1.83	1.96	1.90	1.72	1.52	1.25	1.74	1.39	1.70	1.76	1.56
Mn	0.00	0.00	0.01	0.00	0.00	0.00	0.00	0.01	0.01	0.01	0.00	0.00	0.00	0.00	0.00	0.01	0.00	0.00
Fe ²⁺	1.34	1.27	1.17	1.25	0.97	1.32	1.23	0.91	1.02	0.79	0.72	1.30	1.06	0.89	1.11	1.00	0.92	1.16
Zn	0.00	0.00	0.00	0.00	0.01	0.00	0.00	0.00	0.01	0.05	0.00	0.00	0.00	0.00	0.00	0.00	0.00	0.00

Sample Position	MH1-03-1	MH1-19-4		MH1-14-2		MH1-13-2		MH1-07-1		MH1-43-1	MH2-15a-5		MH2-43-5		MH2-17-1		MH2-15b-1	
	Grain	Core	Rim	Core	Rim	Core	Rim	Core	Rim	Grain	Core	Rim	Core	Rim	Core	Rim	Core	Rim
Li*	0.03	0.00	0.00	0.00	0.00	0.00	0.00	0.00	0.00	0.00	0.06	0.06	0.20	0.09	0.12	0.11	0.11	0.10
X: Ca	0.17	0.01	0.12	0.19	0.19	0.05	0.16	0.15	0.17	0.09	0.07	0.09	0.06	0.14	0.10	0.18	0.18	0.14
Ba	0.00	0.00	0.00	0.00	0.00	0.00	0.00	0.00	0.00	0.00	0.00	0.00	0.00	0.00	0.00	0.00	0.00	0.00
Na	0.54	0.49	0.64	0.59	0.54	0.58	0.59	0.56	0.55	0.67	0.52	0.72	0.63	0.57	0.57	0.62	0.62	0.65
K	0.00	0.01	0.01	0.02	0.01	0.00	0.00	0.00	0.01	0.01	0.01	0.01	0.01	0.00	0.01	0.00	0.00	0.00
Vacancy	0.29	0.49	0.23	0.20	0.25	0.37	0.24	0.28	0.27	0.23	0.41	0.18	0.30	0.28	0.32	0.19	0.20	0.20
OH	3.86	4.00	3.89	3.90	3.82	3.91	3.88	3.83	3.73	3.91	4.00	4.00	3.91	3.96	4.00	3.99	4.00	4.00
F	0.14	0.00	0.11	0.10	0.18	0.09	0.12	0.17	0.27	0.09	0.00	0.00	0.09	0.04	0.00	0.01	0.00	0.00
Fe/(Fe+Mg)	0.50	0.50	0.41	0.42	0.35	0.51	0.44	0.33	0.34	0.29	0.30	0.46	0.46	0.34	0.44	0.37	0.34	0.43
Ca/(Ca+Na)	0.24	0.01	0.16	0.24	0.26	0.08	0.22	0.22	0.24	0.12	0.11	0.11	0.09	0.20	0.16	0.23	0.23	0.18

Table 4.4: The table shows representative compositions of tourmaline at Mineral Hill. Mineral formulas calculated on the basis of 31 anions. *Because boron is difficult to analyze with the EPMA, and lithium and water cannot be analyzed, they are all calculated in the table through stoichiometry. Despite this difficulty, measured quantities of boron demonstrate good agreement with the theoretical stoichiometric quantities of boron, and the measured quantities of all elements analyzed in tourmaline are reported in the Appendix (Table A14).

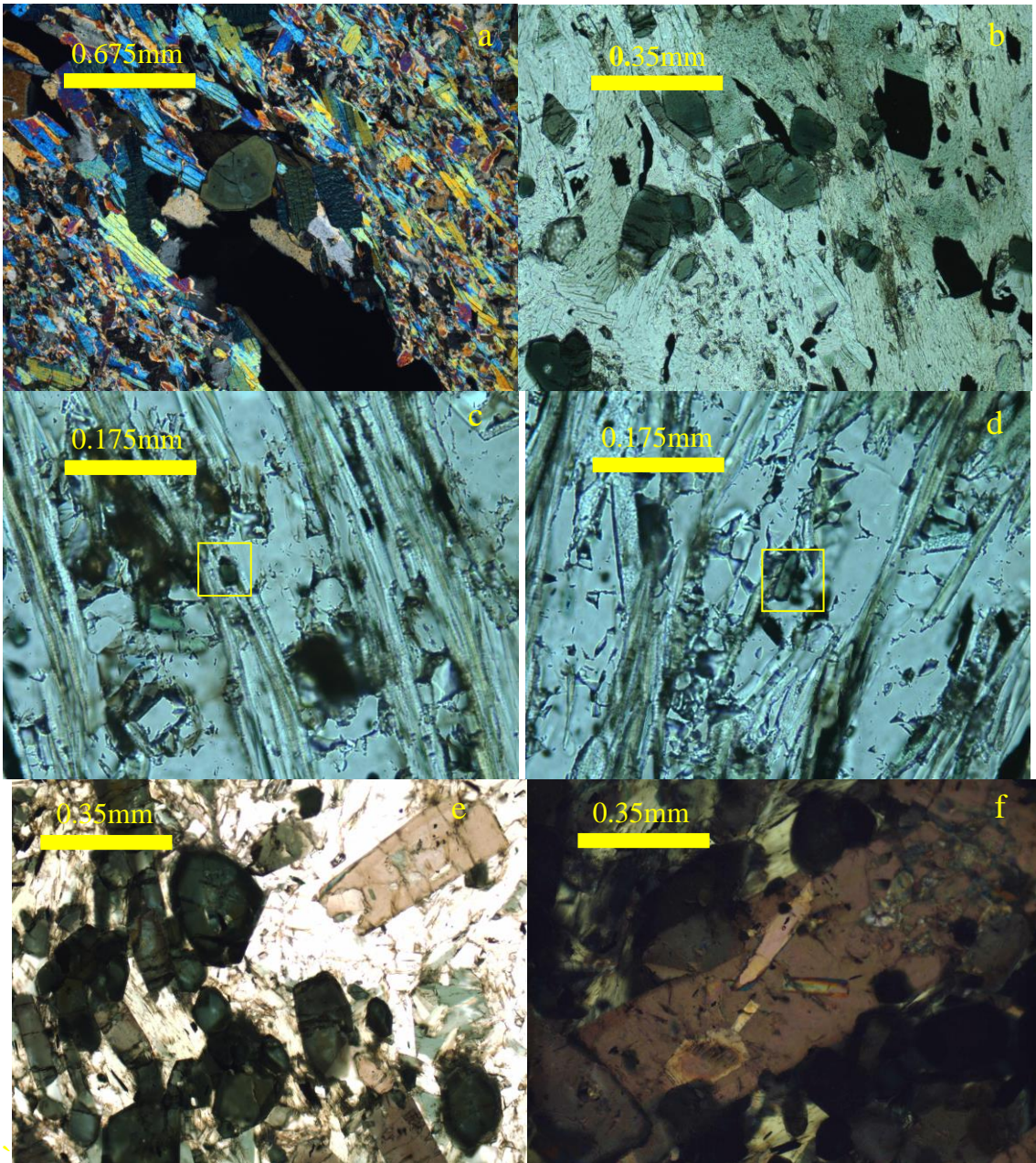


Figure 4.2a-f: Optical photomicrographs depicting the contrasting morphologies of tourmaline present in this study.

Figure 4.2a shows a representative, euhedral, zoned tourmaline grain from MH2-17 under plane polarized light. The grain is surrounded by a schistose chlorite and muscovite matrix with magnetite. b) This photo shows a stringer of tourmaline from MH2-17 with variably deformed and zoned tourmaline in a schistose matrix of chlorite, muscovite, and magnetite. c) Fine grained tourmaline from MH1-13 is shown boxed in

yellow under plain-polarized light (ppl). The matrix is composed of muscovite, chlorite, and quartz. d) MH1-04 micrograph shows a tabular tourmaline grain (yellow box) in a matrix of chlorite, quartz, and muscovite in ppl. e) Part of a tourmaline aggregate in a chlorite and muscovite matrix is shown in ppl. f) Depicts the central portion of a tourmaline aggregate wherein tourmaline is intergrown in a matrix of tourmaline and chlorite in cross-polarized light.

Tourmaline in the rocks of Mineral Hill will likely bear chemical characteristics of both the host environment and the influence of hydrothermal fluid input. The extent to which each of these factors influences the composition of tourmaline will be a function of the water-rock ratio (Slack and Trumbull, 2011). In the limit where the bulk composition of tourmaline is strongly influenced by the composition of the protolith, the composition of tourmaline will conform to those typically associated with rocks of a given chemical composition as discussed by Henry and Guidotti (1985). As the influence of a hydrothermal fluid on the composition grows one would expect to see significant departures from the scheme of Henry and Guidotti (1985).

Figures 4.2a-f show the variability in tourmaline morphology at Mineral Hill, with some grains appearing euhedral whereas others appear to be sub- to anhedral. However, no tourmaline grains have been found exhibiting characteristics of a detrital nature (e.g., terminated growth zones and irregular boundaries), and therefore the grains do not appear to be detrital. Moreover, tourmaline cores and rims appear to form continuous trends in tourmaline composition space (e.g., on the diagrams of Henry and Guidotti, 1985), again suggesting that the tourmalines at Mineral Hill grew in situ. Tourmaline from Mineral Hill plot dominantly in the field for metapelites and

metapsammites (Figure 4.3, 4.4), whereas detrital tourmaline would likely show wider compositional variation. The tourmaline are unlikely to be authigenic and do not have the composition (foititic) and characteristics of authigenic tourmaline shown by Henry and Dutrow (2012).

The boron source for tourmaline growth is unknown. Minerals such as illite (100–2000 µg/g), glauconite (250–2000 µg/g), muscovite (10–1340 µg/g), serpentine minerals (12–330 µg/g), montmorillonite (5–300 µg/g), plagioclase (1–20 µg/g) and chlorite (3–221 µg/g) (Henry and Dutrow, 1996; Hezel et al., 2011; Kaliwoda et al., 2011; and Vils et al., 2011) may all contain boron, although tourmaline is the mineral most stable during metamorphism with the other minerals tending to lose boron and water during progressive prograde metamorphism.

Chlorite and muscovite at MH2 appear to occur with talc. Talc most likely occurs in these rocks as a breakdown component of ultramafic material. As such, the appearance of talc may indicate the presence of an ultramafic component to the original sediment if minerals such as chlorite and muscovite are indicative of a pelitic component. If the occurrence of pelitic and ultramafic material are related to a seafloor depositional environment, and the associated minerals are known to sequester measurable concentrations of boron, then they may act as boron reservoirs for the growth of tourmaline if the tourmaline is metamorphic.

However, in the case of aggregated tourmaline, formation via purely metamorphic processes is unlikely. To address the implausibility of creating a rock with ~10 vol % tourmaline (a minimum as far as the aggregated tourmaline host rock is concerned) from metamorphic processes, consider the following scenario: in a 1 kg rock that has 500 g of

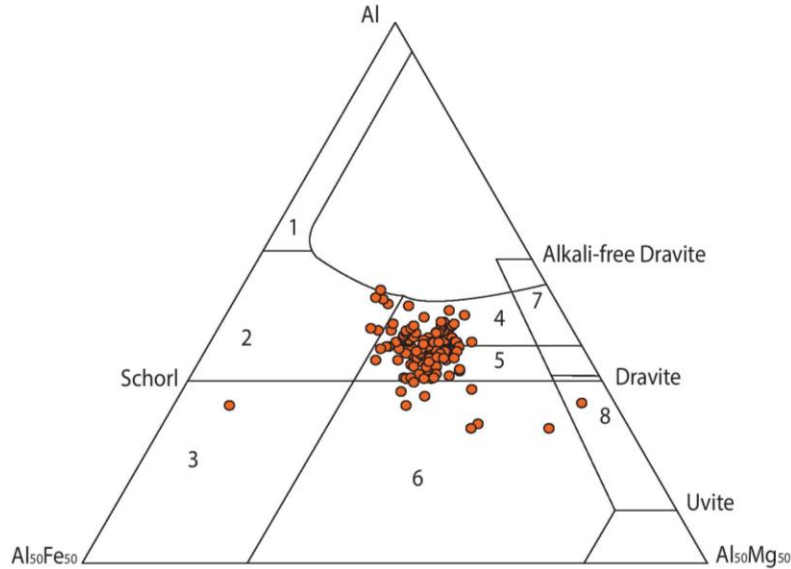


Figure 4.3: Al-Fe-Mg ternary diagram with analysis of all tourmalines from drill cores MH1 and 2 plotted on a Henry and Guidotti (1985) tourmaline composition versus rock-type diagram. The field are as follows: (1) Li-rich granitoid pegmatites and aplites, (2) Li-poor granitoids and their associated pegmatites and aplites, (3) Fe^{3+} -rich quartz-tourmaline rocks (hydrothermally altered granites), (4) metapelites and metapsammites coexisting with an Al-saturating phase, (5) metapelites and metapsammites not coexisting with an Al-saturating phase, (6) Fe^{3+} -rich quartz-tourmaline rocks, calc-silicate rocks, and metapelites, (7) low-Ca metaultramafics and Cr, V-rich metasediments, and (8) metacarbonates and meta-pyroxenites. Table A13 in the Appendix includes the comprehensive data set of the microprobe-derived chemistry for all tourmaline analyses.

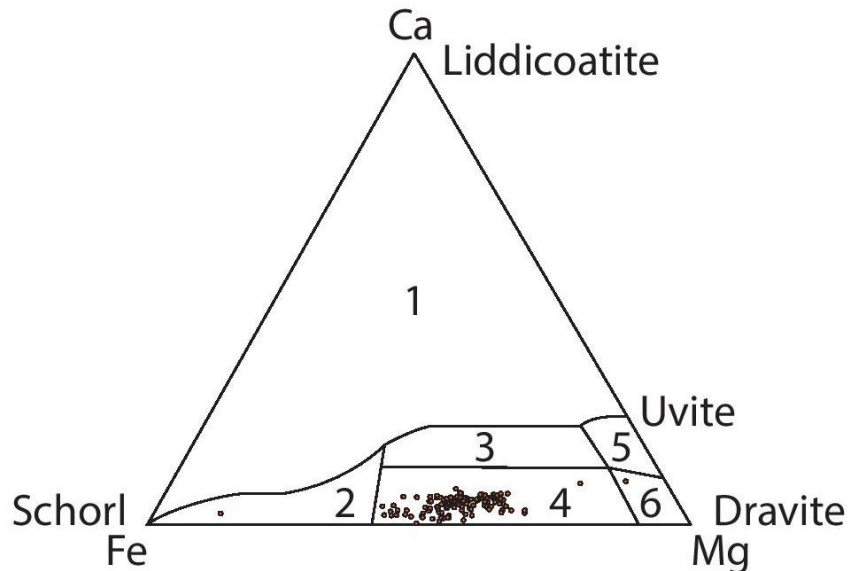


Figure 4.4: Ca-Fe-Mg diagram with analysis of all tourmalines from drill cores MH1 and 2 plotted on a Henry and Guidotti (1985) tourmaline composition versus rock-type diagram, showing the low calcium concentrations in Mineral Hill tourmaline. The field are as follows: (1) Li-rich granitoid pegmatites and aplites, (2) Li-poor granitoids

and their associated pegmatites and aplites, (3) Ca-rich-metapelites, metapsammites, and calc-silicate rocks, (4) Ca-poor metapelites, metapsammites, and quartz-tourmaline rocks, (5) metacarbonates, and (6) metaultramafics.

chlorite, and 500 g illite (a simple metapelite), chlorite and illite can host, at maximum, ~200 $\mu\text{g/g}$ and 2000 $\mu\text{g/g}$ of boron, respectively. These concentrations result in approximately 1 g of boron locked away in the minerals per kilogram of rock. To create a 1 kg rock that has 10% tourmaline you would need approximately 4 g of boron (assuming ~12 wt % boron in the tourmaline), resulting in a roughly 4:1 ratio of pelite to 10% tourmaline rock. Consider also that the boron-rich pelite outlined above would be highly anomalous given that the average pelite hosts approximately 150 $\mu\text{g/g}$ of boron (Leeman and Sisson, 1996). In hydrothermal environments of high-water rock ratios, where channelized fluid flow could occur along veins or faults, accumulating large concentrations of boron seems more feasible. However, using metamorphic processes to derive tourmaline-bearing rock with <1 vol % tourmaline (as in the case of disseminated tourmaline) seems more plausible if liberating boron trapped within mineral phases.

Metamorphic overgrowths on tourmaline may be generated by the progressive release of boron from boron reservoir minerals such as illite and serpentine. Serpentine occurs frequently in the MH1 core so the titration of the sediment source area with serpentine, and the resultant breakdown of serpentine, is not unlikely. Its reaction with quartz and other phases could provide essential boron as a nutrient for tourmaline growth. As a hydrothermal fluid circulated in, variably, a pelitic ooze, ultramafic detritus, and continent-derived sediment the fluid may have enriched protolith phases in boron, or formed small grains of tourmaline (i.e. the disseminated tourmaline in MH1 and MH2). Further nucleation and growth could then occur during breakdown of various reservoir

minerals along a prograde metamorphic path, and this method of formation does not exclude the possibility of later retrograde growth from metasomatic fluids.

The aggregated tourmaline is concentrated in approximately 6 inches of drill core in MH2. As indicated in Figure 3.2, although MH2 sits structurally higher than MH1, MH2 is not necessarily stratigraphically higher due to the highly deformed nature of the region. Aggregated tourmaline have average Fe/(Fe+Mg) core and rim concentrations of 0.36 to 0.42 mole fraction (Table 4.4), respectively, showing an apparent trend of decreasing aluminum in favor of iron relative to the dravite-schorl solid solution. As indicated by Figure 4.3, the tourmaline at Mineral Hill appear to be related to metapelites and metapsammites, and in conjunction with Figure 4.4, may have been Ca-poor. What is not seen in Figures 4.3-4.4 are significant excursions into fields 8 and 6, respectively, which are tourmaline related to ultramafic rocks.

Aggregated tourmaline occurs with muscovite, epidote, chlorite, and accessory talc as the silicate phases with magnetite, ilmenite, and trace chromite as the oxide phases. There is also trace apatite, zircon, chalcopyrite, pyrite, allanite, and monazite. The aggregated tourmaline appear to exhibit a core to rim trend of increasing iron at the cost of aluminum (Figure 4.5), meaning the concentration of Fe-rich fluid likely increased relative to magnesium with time. Aggregated tourmaline may have first formed in equilibrium with ultramafic detritus and seawater near the deposit's paleo-footwall where porosity was high, which would account for originally Mg-rich cores. Later circulation of Fe-rich hydrothermal fluid coupled with higher water-rock ratios would result in Fe-rich rims as well as increased abundance of boron allowing for the intergrowth of tourmaline (Slack and Coad, 1989; Slack and Trumbull, 2011). If this

trend of increasing iron relative to magnesium is an indication of higher hydrothermal fluid flux, it is possible that it could serve as an exploration vector for mineralization.

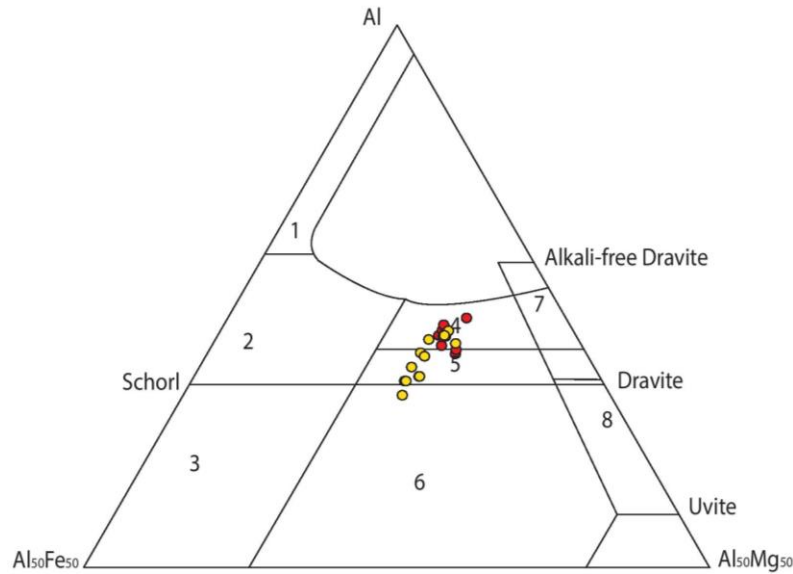


Figure 4.5: Plot of a subset of the tourmaline data representing the tourmaline aggregates from samples MH2-15a and MH2-15b and their associated core (red) and rim (yellow) data. Any intermediate zones between the core and rim are excluded.

The isolated tourmaline occur throughout drill cores MH1 and MH2. In Figure 4.6, the variation in the composition space of MH2 isolated tourmaline grains can be most easily described as aluminum substitution for magnesium in dravite-schorl solid solution. This Al/Mg trend is opposite to the trend for the aggregated tourmaline of MH2. There does not appear to be a trend relating Ca/Na/vacancies in tourmaline to the substitution of Al for Mg.

Figure 4.7 below demonstrates the zoning that is characteristic of isolated tourmaline from MH2 on a pseudo-colored BSE image with its associated Fe-Mg variation. Concentrations of Fe/(Fe+Mg) in the core average 0.44 and the rims average 0.38 (Table 4.4).

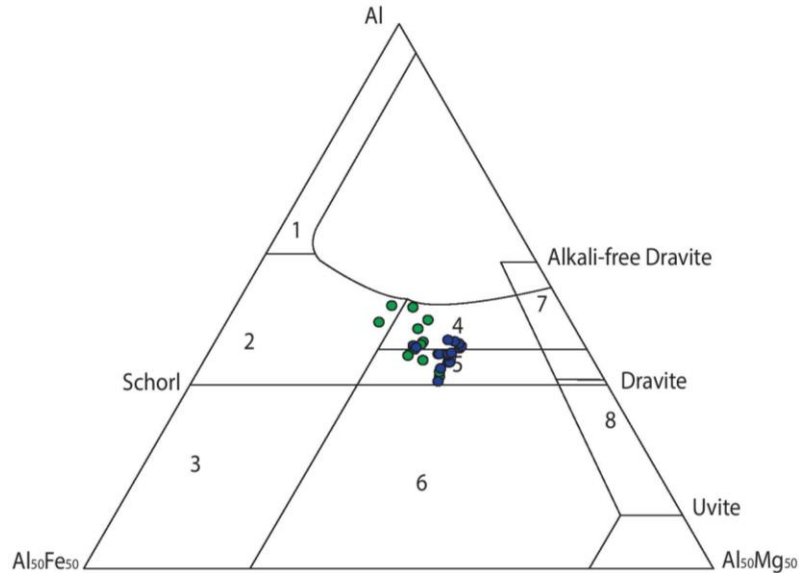


Figure 4.6: A subset of the tourmaline data representing the isolated tourmalines from samples MH2-17 and MH2-43 and their associated core (green) and rim (blue) data. Any intermediate zones between the core and rim are excluded.

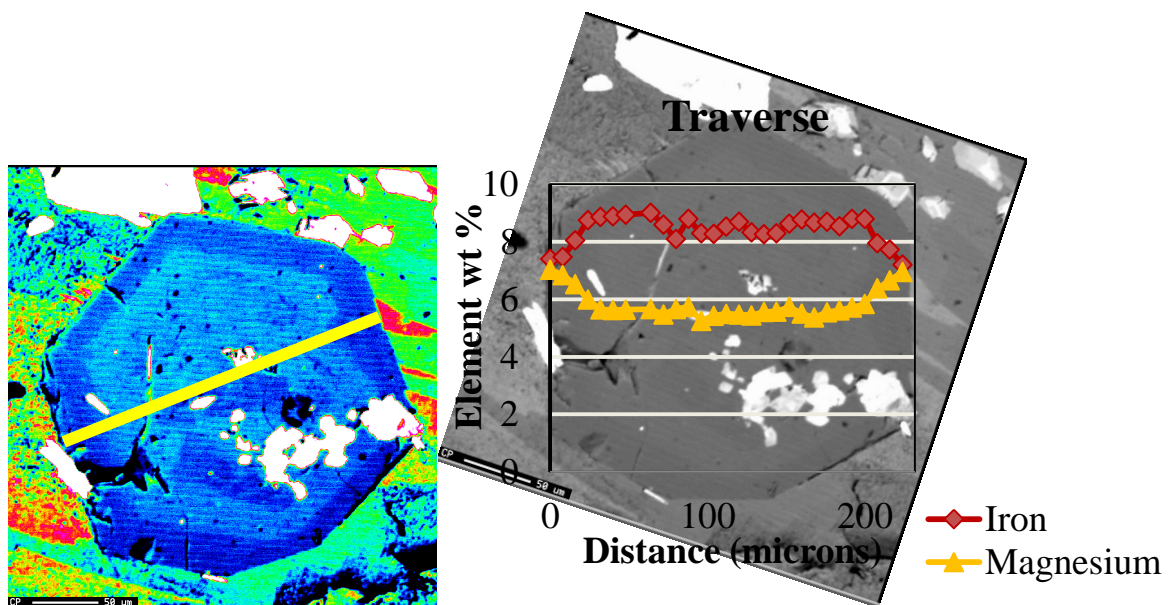


Figure 4.7a: To better display zoning, the tourmaline shown is a pseudo-colored rendition of the accompanying BSE image (4.7b). The yellow line represents the WDS traverse run across the grain to test the variability of zoning.

Figure 4.7b: Figure 4.7n shows the same tourmaline in 4.7a as a BSE image. Mg and Fe weight percent values are shown across the WDS traverse.

Isolated tourmaline have a more variable associated mineralogy, but the primary silicate phases are quartz and muscovite with accessory chlorite, epidote, plagioclase, and

trace biotite and zircon. Magnetite and ilmenite are the dominant oxide phases.

Tourmaline occurrences at both MH1 and MH2 are notably deficient in Ca relative to Na, and both may contain inclusions of epidote and/or magnetite.

In addition to differing mineral assemblages, tourmaline from MH1 is morphologically distinct from tourmaline in MH2. It occurs as isolated grains that are typically very fine-grained, rounded to tabular, and lack observable zoning in contrast to the comparatively large, often euhedral crystals in MH2 that have readily observable zoning. The apparent rims and cores of tourmaline within the MH1 sections were sampled and have very similar Fe/(Fe+Mg) concentrations of 0.409 and 0.419 (Table 4.4), respectively. While there does appear to zoning in some tourmaline crystals in MH1, due to the size of the crystals, it becomes extremely difficult to precisely sample cores and rims using the electron probe microanalyzer. A result of this difficulty may be that although the MH1 tourmaline appear to plot in a similar compositional space to MH2 isolated tourmaline, there is no apparent trend in the composition of MH1 tourmaline when moving from core to rim (Figure 4.8). A mineralogical distinction is that the prevalence of plagioclase and quartz appear to increase in MH1 relative to MH2, and several tourmaline were analyzed either adjacent to or in proximity of quartz. The tourmaline grains at all depths from both cores share the same approximate whole grain Fe/(Fe+Mg) total of ~0.4.

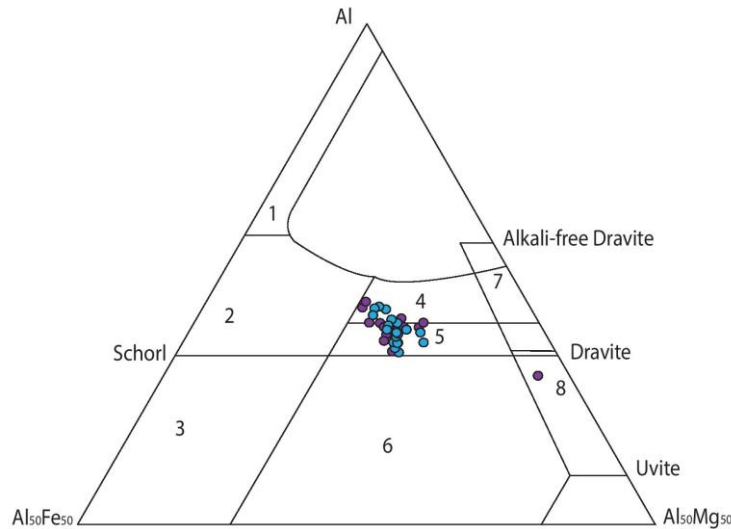


Figure 4.8: The cores (purple) and rims (blue) of isolated tourmalines from samples MH1-03, MH1-19, MH1-13, MH1-14, MH1-07, and MH1-43. Any intermediate zones between the core and rim are excluded.

Exceptions to the clustering do occur in tourmaline from MH1. For example, tourmaline abundance appeared to decrease past the ore zone and only one tourmaline was found and analyzed from MH1-43, a single tourmaline from MH1-13 appears highly dravitic, and several tourmalines analyses from MH1-03 are closer to the schorl endmember.

The crustal abundance of boron is 17 $\mu\text{g/g}$ (Rudnick and Gao, 2003); and the concentration of boron in seawater and in some vent fluids is on the order of 10 ppm (Berndt and Seyfried, 1990; Henry and Dutrow, 2012). The concentration of boron needed to stabilize tourmaline in a fluid at 400°C is on the order of 160 ppm (Weisbrod et al., 1986). Therefore, the boron concentration in a seawater-derived fluid must be augmented if tourmaline is to form in this temperature range (and for the bulk composition studied by Weisbrod et al.). The excess boron needed to stabilize the disseminated tourmaline may be provided by the destruction of the serpentine component in the metasediment, as outlined in the high-boron pelite scenario earlier in this section,

and/or by the boiling of the seawater-derived hydrothermal fluid. If boiling is necessary to achieve the concentrations of boron necessary for tourmaline stability then water depths corresponding to pressures less than the critical pressure of seawater (299 bars or ~3000 m) are required (Bischoff and Rosenbauer, 1988). To further refine the source of boron, isotopic analysis of $\delta^{11}\text{B}$ in tourmaline would be required.

4.2.3 Chlorite

Chlorite is a typically triclinic, hydrous phyllosilicate characterized by the combination of an octahedral brucite-like sheet alternating with a talc-like sheet. Chamosite $[(\text{Fe}_5\text{Al})(\text{Si}_3\text{Al})\text{O}_{10}(\text{OH})_8]$ and clinochlore $[(\text{Mg}_5\text{Al})(\text{Si}_3\text{Al})\text{O}_{10}(\text{OH})_8]$ follow the Fe-Mg continuous solid solution series and are the two most common varieties of chlorite in altered igneous rocks. Other common substitutions for Fe and Mg include Mn, Ni, and Zn, as well as Al variation along the $\text{Al}^{(\text{IV})}\text{Al}^{(\text{VI})}\text{Si}_{-1}^{(\text{IV})}\text{Mg}_{-1}^{(\text{VI})}$ exchange vector. Although chlorite is most commonly green, it may occur in a wide spectrum of colors and is also associated with anomalous blue-violet interference colors in thin section. Chlorite is often found in low-to-medium grade metamorphic rocks, as well as hydrothermally altered ultramafic and mafic rocks (Bailey, 1988).

Chlorite is a common matrix constituent of the rocks in the Mineral Hill core, and occurs in both metasedimentary rocks, and in the metasomatized blackwall zones that formed between the ultramafic and pelitic country rocks (Candela et al., 1989). Common chlorite assemblages in metasomatized ultramafic rock include talc + chlorite \pm serpentine \pm carbonate, and in metapelites the assemblage shifts to muscovite + plagioclase + quartz + chlorite \pm epidote \pm actinolite \pm biotite. Chlorite is of variable grain size, ranging from fine (microns) to coarse (millimeters), in both cores. The chlorite

from MH1 and MH2 tend to be intermediate in the clinocllore-chamosite solid solution series, as show in Table 4.5, and is thus best labeled as ripidolite in the Hey (1954) naming scheme. The grains tend to be anhedral and pleochroic green-light green (although intensity of pleochroism depends upon optic orientation).

Sample	MH2-25-4	MH2-32-2	MH2-15-4	MH2-04a-2	MH2-15b-4	MH2-17-7	MH2-43-4	MH1-24-3	MH1-03-3	MH1-19-3	MH1-14-2	MH1-13-4	MH1-07-5	MH1-43-5
SiO ₂	26.10	30.17	24.92	29.72	24.22	24.94	25.27	40.79	24.06	25.18	25.86	24.98	24.87	25.80
TiO ₂	0.06	0.02	0.03	0.02	0.02	0.05	0.10	0.02	0.05	0.06	0.07	0.05	0.07	0.05
Al ₂ O ₃	22.40	17.89	23.34	18.87	23.35	23.61	22.13	4.07	22.52	23.04	22.01	23.07	22.77	22.57
FeO	24.76	10.24	23.27	11.77	23.43	22.59	25.13	5.38	26.68	24.27	22.19	26.25	20.48	19.71
MnO	0.42	0.21	0.17	0.27	0.19	0.21	0.30	0.10	0.35	0.29	0.42	0.36	0.42	0.48
MgO	14.44	26.33	15.26	24.79	13.76	15.69	14.83	34.07	13.33	15.34	17.36	14.40	16.83	18.24
CaO	0.03	0.02	0.02	0.03	0.45	0.00	0.01	0.01	0.00	0.00	0.00	0.00	0.02	0.02
Na ₂ O	0.03	0.08	0.07	0.07	0.05	0.02	0.06	0.01	0.03	0.06	0.04	0.12	0.07	0.04
K ₂ O	0.18	0.06	0.06	0.02	0.05	0.03	0.06	0.02	0.02	0.07	0.05	0.03	0.02	0.02
Structural formula based on 36 oxygen														
Si	5.41	6.01	5.21	5.93	5.18	5.19	5.30	4.87	5.15	5.22	5.33	5.18	5.23	5.31
Al	5.49	4.21	5.76	4.45	5.90	5.81	5.48	0.36	5.69	5.64	5.35	5.65	5.65	5.48
Ti	0.01	0.00	0.01	0.00	0.00	0.01	0.02	0.00	0.01	0.01	0.01	0.01	0.01	0.01
Fe	4.29	1.71	4.07	1.96	4.19	3.93	4.41	16.31	4.78	4.21	3.83	4.55	3.60	3.39
Mn	0.07	0.03	0.03	0.05	0.03	0.04	0.05	0.01	0.06	0.05	0.07	0.06	0.07	0.08
Mg	4.46	7.82	4.75	7.37	4.39	4.87	4.64	6.07	4.26	4.74	5.33	4.45	5.27	5.59
Ni	0.00	0.00	0.00	0.00	0.00	0.00	0.00	0.00	0.00	0.00	0.00	0.00	0.00	0.00
Ca	0.01	0.01	0.00	0.01	0.10	0.00	0.00	0.00	0.00	0.00	0.00	0.00	0.01	0.00
Na	0.02	0.06	0.06	0.06	0.04	0.01	0.05	0.00	0.03	0.04	0.03	0.10	0.05	0.03
K	0.09	0.03	0.03	0.01	0.03	0.02	0.03	0.01	0.01	0.04	0.03	0.01	0.01	0.01
OH*	16.00	16.00	16.00	16.00	16.00	16.00	16.00	16.00	15.98	15.99	15.98	15.93	15.95	15.95
Wt % Total	88.41	85.01	87.15	85.56	85.52	87.14	87.88	84.47	87.03	88.32	87.99	89.26	85.55	86.93
Fe/(Fe+Mg)	0.49	0.18	0.46	0.21	0.49	0.45	0.49	0.73	0.53	0.47	0.42	0.51	0.41	0.38

Table 4.5: Table of the composition of chlorite. Mineral formulas calculated on the basis of 28 oxygen. Al^{IV} and Al^{VI} in addition to Fe³⁺ and Fe²⁺ have been summed to yield Al(tot) and Fe(tot). OH content is assumed to be 16.

Fe/(Fe+Mg) ratios in chlorite vary between 0.07 mole fraction and 0.61 mole fraction with an average of about 0.40 mole fraction at both MH1 and MH2. There is typically very little variation in the standard deviations of the Fe/(Fe+Mg) concentration among chlorite grains within a thin section. The original expectation was that chlorite may experience Fe/(Fe+Mg) variance in relation to the ore zone as seen at Kidd Creek (Slack and Coad, 1989), although there does not appear to be a trend in Fe/(Fe+Mg) concentration with depth (Figure 4.9) at Mineral Hill. Some Fe/(Fe+Mg) variance that may, however, be loosely attributed to the presence of tourmaline.

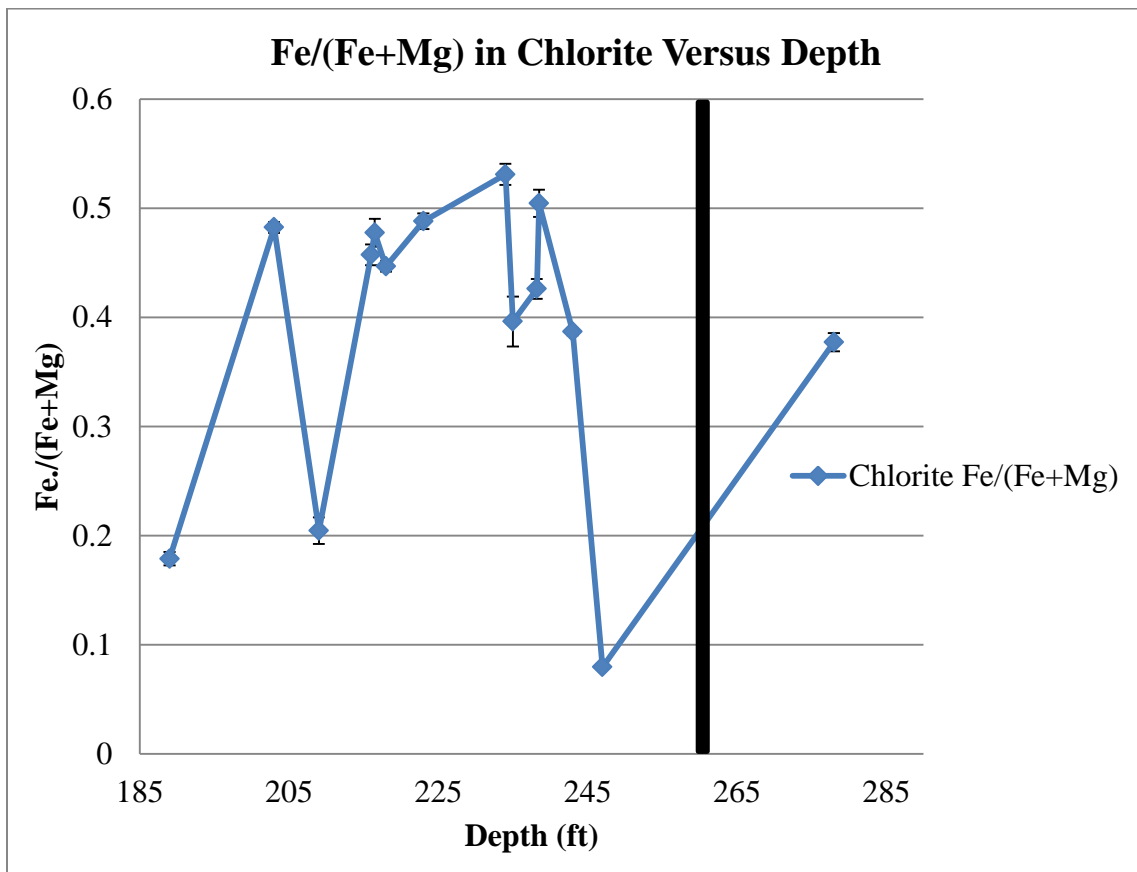


Figure 4.9: Sample-averaged values for the Fe/(Fe+Mg) ($\pm 1 \sigma$) concentration of chlorite grains from all analyzed thin sections against their respective depth. The vertical bar represents the approximate depth of the ore zone at Mineral Hill.

The Fe/(Fe+Mg) ratio of chlorite from MH1 and MH2 (Figure 4.10) appears to be elevated in the presence of tourmaline. This occurs in the nominally metapelitic assemblage (muscovite + plagioclase + quartz + chlorite ± epidote ± actinolite ± biotite). In contrast, where Fe/(Fe+Mg) ratios remain low and where tourmaline is typically absent, the mineralogical assemblage talc + chlorite ± serpentine ± carbonate reflects direct or indirect mafic-ultramafic contributions. This material may have come from an original ultramafic component (talc + serpentine). Aluminum (Figure 4.10) does not appear to exhibit a clear trend as a function of depth at MH2, although there is again a suggestion that Al in chlorite is slightly elevated when coexisting with tourmaline in a metagraywacke assemblage. The varying Fe, Mg, and Al concentrations in chlorite may reflect the variable contributions of continental/arc vs. ultramafic related components in the original depositional environment.

If fluid percolated through the entirety of the stratigraphic column, and given a hydrothermal origin for tourmaline, seawater boron would have facilitated the formation of tourmaline in all horizons; however, we do not observe this. Instead, tourmaline appears stratabound and limited to metagraywacke horizons meaning it may have been local hydrothermal fluid flow that 1) led to the accumulation of boron and 2) may have later mobilized boron trapped in nearby minerals during prograde or retrograde processes that allowed the tourmaline to form. The formation of isolated and aggregated tourmaline could have then been a function of variable porosity and permeability in a given horizon.

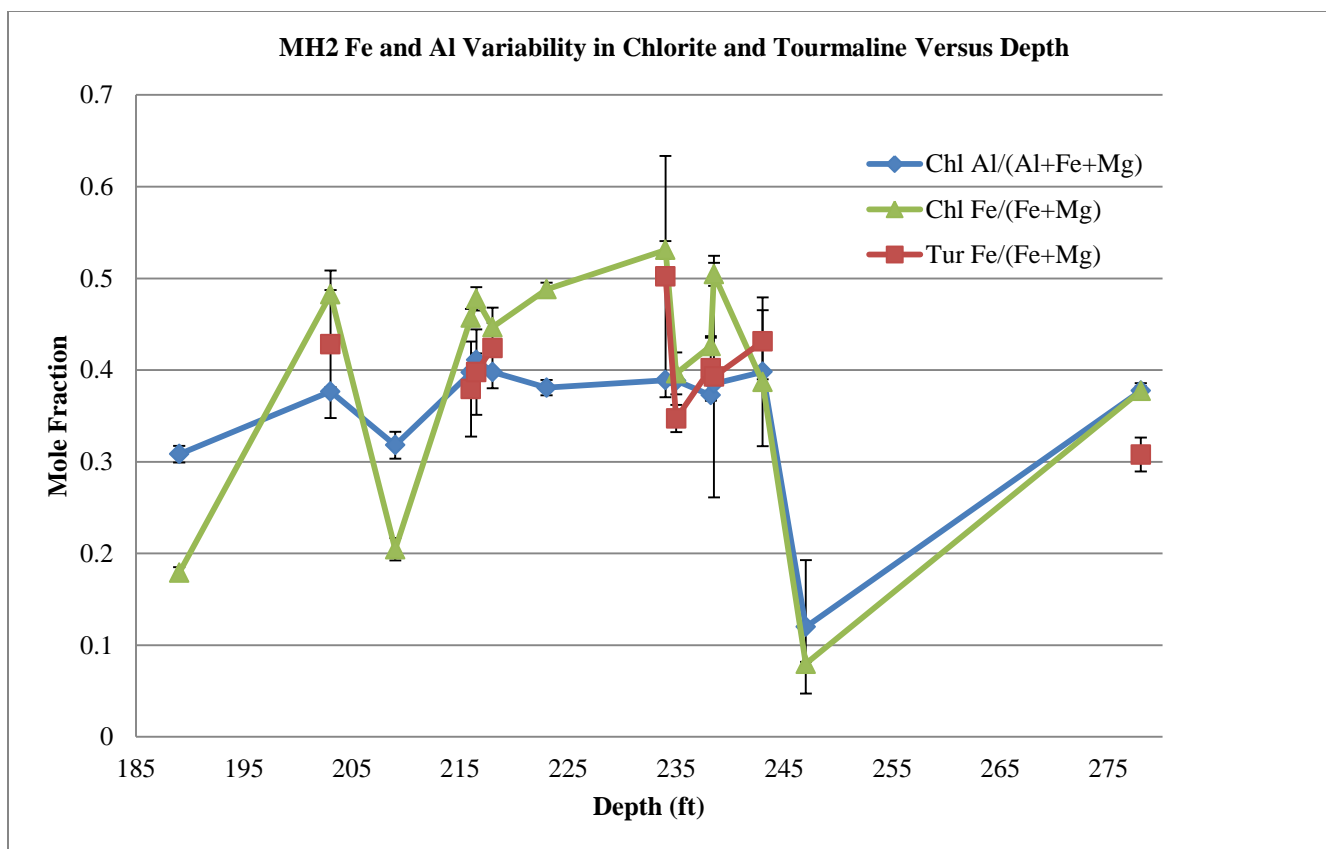


Figure 4.10: Plot of the average $\text{Fe}/(\text{Fe}+\text{Mg})$ ($\pm 1 \sigma$) and $\text{Al}/(\text{Al}+(\text{Fe}+\text{Mg}))$ ($\pm 1 \sigma$) concentrations for chlorite and coexisting tourmaline (where present) versus depth at MH2. Tourmalines from MH2 include both aggregated and isolated tourmaline data. The tourmaline ratios represent averaged concentrations from the cores, zones, rims, and whole grains of tourmalines within a thin section. The tourmaline ratios in this figure represent the values of averaged grains. Due to difficulty of analysis, the chlorite represents averages of several points both within grains and then among several grains in each thin section.

4.2.4 Monazite

In an attempt to determine the age of the rocks associated with the Mineral Hill deposit, and better understand the relationship of the mineralization to regional tectonics, we analyzed monazite for use in U-Pb dating. Although fine-grained, the monazite present at Mineral Hill is suitable for *in-situ* radiogenic dating. Monazite is a dominantly light rare earth element-bearing orthophosphate that is notable for its high closure temperature. A LREE source, such as allanite, must be available to facilitate the formation of monazite. If the rocks at Mineral Hill are, as indicated by the tourmaline source-rock diagrams, related to low Ca-metapelites, then allanite would not have been stable (Spear and Pyle, 2010). The occurrence of allanite is also variable. In addition to forming in grains of zoned epidote –allanite, zoning in the form of monazite cores rimmed by allanite and epidote have also been recorded. The allanite present in the rocks do not appear to exhibit equilibrium textures and are almost ubiquitously anhedral and often corroded without defined grain boundaries.

Hydrothermal monazite has been identified in a number of mineral deposits. Hydrothermal monazite has been identified by, in part, its low thorium concentration (Schandl and Gorton (2004)). Monazite with similar thorium concentrations to those of Mineral Hill occur in highly metamorphosed VMS deposits (e.g. Geco Mine, Greece). If the monazite at Mineral Hill is not igneous or metamorphic, as indicated by the thorium content, it may be hydrothermal. The monazite at Mineral Hill can occur in interior of epidote, separated by an intermediate zone of allanite. This zoning may indicate an early date of formation for monazite. Early formation is further supported by monazite's association in the MH1 core with magnetite (an early stage ore mineral).

More than 70 monazite grains were found at both the MH1 and MH2 cores at a variety of depths including both above and below the ore zone in the case of MH1. They occur primarily as small, irregular, 5-20 μm neoblasts (Figure 4.11) as well as in the monazite-allanite-epidote zoning pattern noted above.

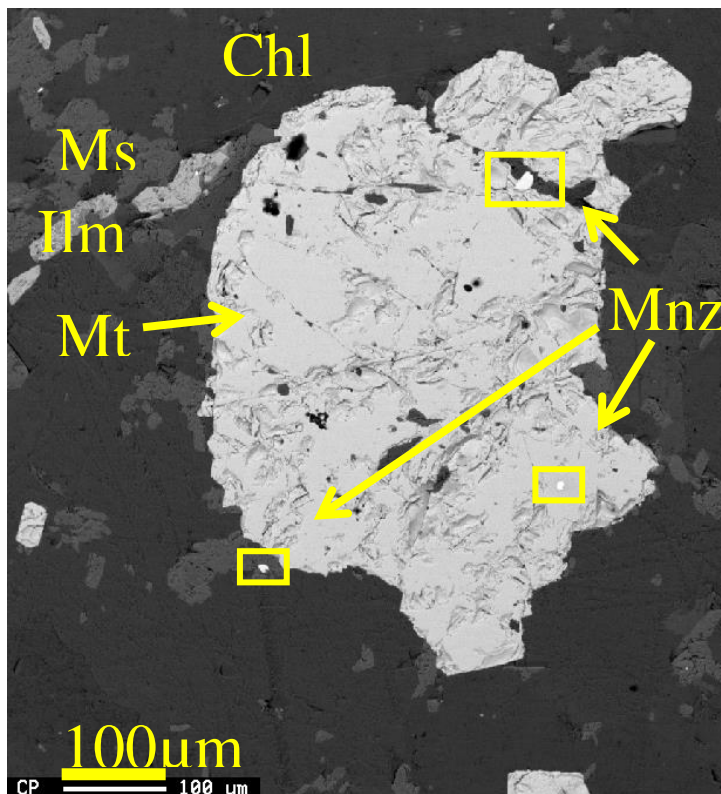


Figure 4.11: Backscatter electron image of a region of sample MH1-11, showing the distribution of monazite. The above figure shows the relative size of the monazite (Mn) at MH2 and their occurrence with magnetite (Mt) in a muscovite (Ms), chlorite (Chl), and ilmenite (Ilm) matrix.

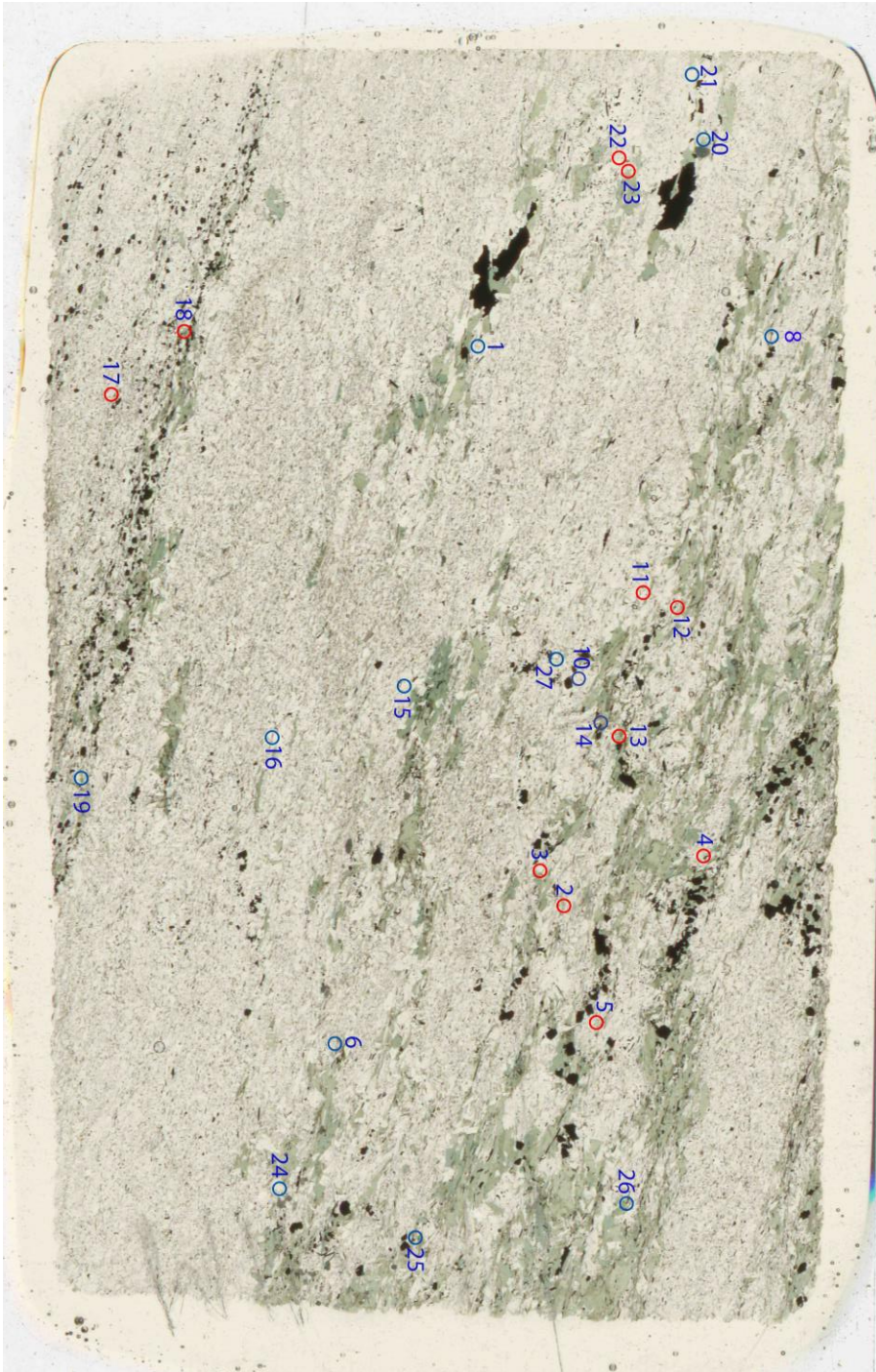


Figure 4.12: Monazites approximately larger than $3 \times 3 \mu\text{m}$ have been circled in slide MH2-17. Blue circles represent monazite that were sampled but did not render useable data, and red circles are monazite that were samples that yielded good quality data. Tables of the associated monazite data including ages, error, mineral chemistry, approximate size, and mineralogical associations are included in Tables A17-A18 in the Appendix as well as maps of the other two samples used for analysis

Monazite grains from 6 samples and 65 points were analyzed for dating. 3 samples contained 28 analyses from 22 grains of sufficient quality for further analysis. Figure 4.12 is a map of a thin section map of the locations of monazite analyses. It is dominantly composed of muscovite, chlorite, epidote, magnetite, with minor ilmenite, tourmaline, chalcopyrite, and trace sphalerite. Layering is moderately well developed and may be original bedding. Tourmaline can be poikiloblastic with magnetite and epidote. Some veining and fluid inclusions also occur. The tourmaline range from anhedral with poor zoning to euhedral with well-preserved zoning. The cores are pleochroic teal blue and the rims are pleochroic green dark-green rims along the c-axis. Maps of the thin sections containing the other monazite samples are included in the Appendix (Tables A1-A2).

Figure 4.13 represents the first attempt to directly date the ore deposit at Mineral Hill and the one of the first uses of monazite dating in the region. Monazite from MH1-11 are in particular notable because some occur as inclusions within magnetite, and the sample occurs within 23 feet of the ore zone. If the magnetite can be taken to be associated with the ore at Mineral Hill, as has been noted by Heyl and Pearre (1965) and Candela et al. (1989), the monazite may place boundaries on the first occurrence of ore at the mean age of 449 Ma (n = 22) followed by progressive metamorphism. Figure 4.14 puts the monazite data into a regional context in a figure modified from Kunk et al. (2005). If the mean is taken as an approximate representation of the monazite data, the monazite become broadly consistent with the Taconian Orogeny (Figure 4.14). This date is corroborated by isotopic analysis of chalcopyrite which yielded $\delta^{34}\text{S}$ values of +12.0 ‰ and +15.4 ‰ and are consistent with a significant component of seawater sulfate in the ore fluid (Robert R. Seal II, personal communication).

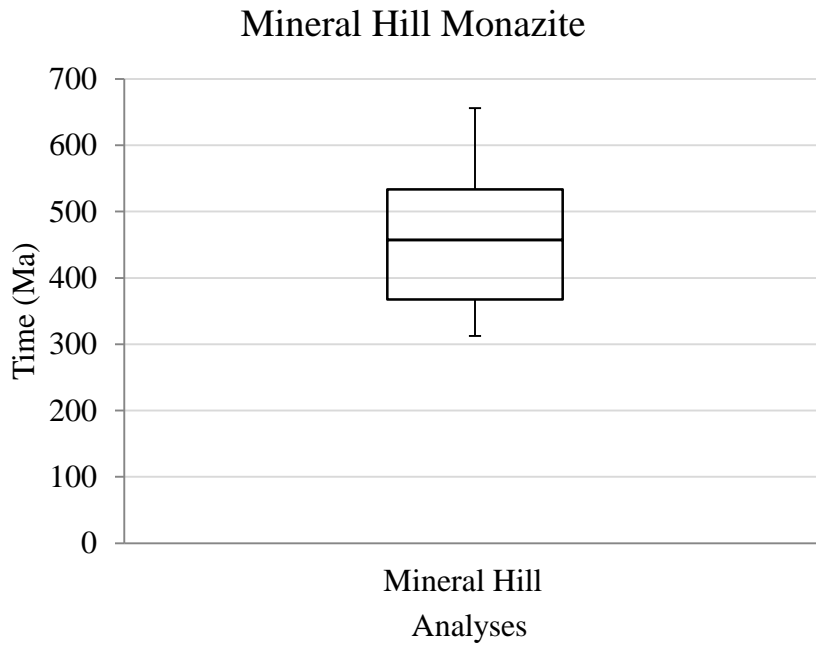


Figure 4.13: Box and whisker plot of the monazite dates ($n = 22$). The box represents the 75th and 25th percentiles, the center bar is the median, and the whiskers extend to the 90th and 10th percentiles. 22 points were used to generate the table and excluded several points with dates of >1 Ga which likely represent spurious data. A table of associated monazite data including ages, error, mineral chemistry, and mineralogical associations is located in the Appendix (Tables A17-A18).

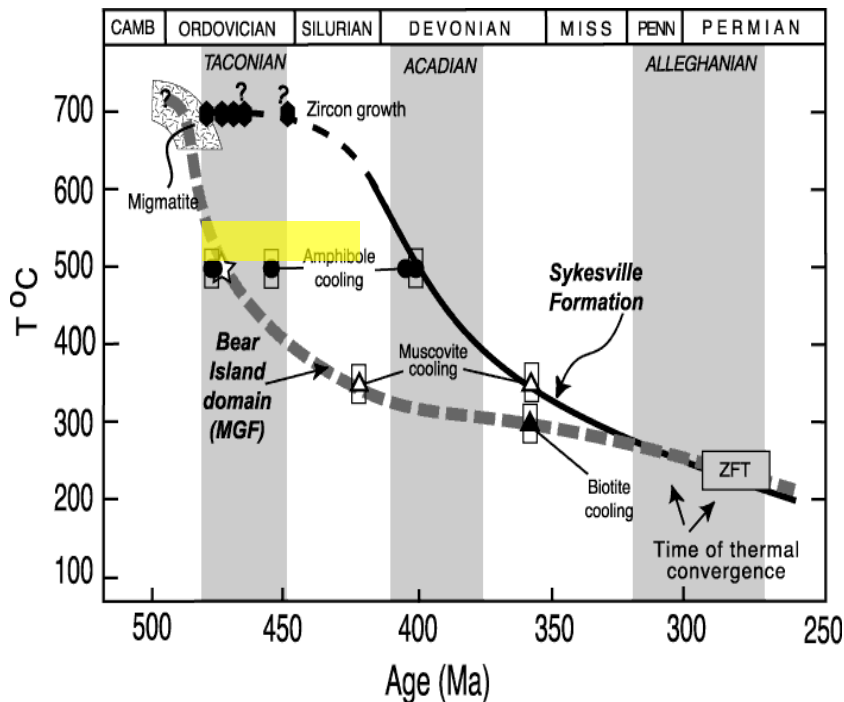


Figure 4.14: K-Ar data from Kunk et al., 2004 who plots the cooling of amphibole (filled circles), and biotite (filled triangle), the cooling and growth of muscovite (filled diamond and open triangle, respectively), the Rb/Sr dates from muscovite (open star), the U-Pb dates from zircon (filled hexagon). Overlain in yellow is the mean (449 Ma) bounded on either side by the standard deviation of the mean. The upper and lower temperature bounds are those found by Candela et al. (1989) using the garnet-biotite geothermometer. The Bear Island domain is a subset of the Mather Gorge Formation in Virginia which is the analog to Maryland's Morgan Run Formation. This figure does not include the more comprehensive temperature and age data from Wintsch et al., 2010 for simplicity.

Although many monazite cluster around 449 Ma, there is a large gap from approximately 450 Ma to 1400 Ma and beyond. This could be the result of the analysis of composite monazite grains, Pb gain, or U loss. Because of monazite's high blocking temperature, analysis of composite grains seems most likely. Points giving dates of >1000 Ma likely represent spurious analyses, and they were not included in Figure 4.13. The results of all monazite analyses are shown in the appendix. However, due to the monazite's spread, the data should be used with caution.

4.3 Mineral Deposit Analogs

Mineral deposit Models allow for the distillation of information, allowing for relationships to be readily established between deposits not only within a district but also globally. These models may then, in turn, be used in exploration as a means of establishing or predicting fundamental criteria and characteristics of an unknown deposit such as location, mineralogy, grade, and tonnage. To quote Cox and Singer (1986):

“Therefore, let us propose a working definition of "model" in the context of mineral deposits, the overriding purpose being to communicate information that helps mankind find and evaluate mineral deposits. A mineral deposit model is the systematically arranged information describing the essential attributes (properties) of a class of mineral deposits. The model may be empirical (descriptive), in which instance the various attributes are recognized as essential even though their relationships are unknown; or it may be theoretical (genetic), in which instance the attributes are interrelated through some fundamental concept.”

Since Mineral Hill was written about by Candela et al. (1989), many researchers have viewed the semi-massive sulfides at Sykesville as an analog to several ore deposits from a variety of regions worldwide, such as Outokumpu, Bou Azzer, Blackbird, and Eastern Metals (Auclair et al., 1993; Peltonen et al., 2008). The intention of Tables A1-A11 listed in the appendix are to provide the best characterization of Mineral Hill possible with the end goal being to establish Mineral Hill in the context of VMS deposits on a global scale, either as part of an existing model schema or separately. The tables contain empirically-based data for VMS

deposits similar to Mineral Hill, as determined by their mineral assemblages, lithologies, and other data.

4.4 Tectonic Interpretation

Muller et al. (1989) proposed the Morgan Run Formation, and by extension the Sykesville District, was an allochthonous subduction complex that formed proximal to a magmatic arc. However, this designation does not explain the origins of the ultramafic rocks, some of which were shown to be detrital (Candela et al., 1989). A more contemporary interpretation that is still in line with the evidence cited by Muller et al. is the interpretation of the Morgan Run Formation as an oceanic core complex (OCC). OCCs are massifs where lower-crustal and upper-mantle rocks may be exposed at the sea floor. They are thought to form episodically through long-lived low-angle detachment faulting rooted beneath the spreading axis of slow and ultra-slow spreading centers (Smith et al., 2006, Ildefonse et al., 2007). The detachment faulting can mylonitize and brecciate the associated rocks, which may include serpentized peridotite and gabbro. Drake (1994) analyzed some serpentized ultramafic rock taken from the Morgan Run Formation and found it was possibly derived from harzburgite, and a study done by Gale et al., 2005 identified ultramafic rock from the nearby Rockville quarry as having a possibly pre-Taconic oceanic lithospheric mantle source rock. Perhaps more importantly, OCCs may also be associated with ore deposits (Cherkeshev, 2013). A possible explanation for the Sykesville District as well as several outlying ore districts (e.g. the Linganore District, Soldier's Delight) is then that mineralization occurred simultaneous to the serpentization and exhumation of ultramafic rocks at a slow-spreading center. The graywacke and schist that characterize the Morgan Run Formation may have been derived, variably, from

both pelagic mud as well as debris shed from a nearby volcanic arc (Presumably the Chopawamsic terrane) that accreted to proto-North America during the Taconian Orogeny. Our collected tourmaline data would be in-line with such an interpretation as most show that they are from metapelites and metapsammites. Many of the primary features of the OCC, such as mullion structures, may have been destroyed by tectonic processes either during accretion or post-accretion by the Alleghanian Orogeny.

This narrative is my current working model for the formation and evolution of the Sykesville mineral deposits, particularly at Mineral Hill. In a setting analogous to an ocean-ridge or back-arc spreading center, ultramafic material was brought to the surface of the seafloor by detachment faulting associated with an oceanic core complex above a slow to ultra-slow spreading center. The pervasively faulted environment typical of a spreading center would allow for the infiltration of seawater leading to serpentinization of the ultramafic rock. The apparently complete serpentinization of ultramafic material at Mineral Hill and the tourmaline aggregates would corroborate with a high water-rock ratio environment. Denudational faulting of the ultramafic material at the core complex may have then caused the formation of an olistostromal, or otherwise brecciated, texture. Evidence for original seafloor derivation of the ultramafic rock comes from the presence of detrital chromite in pelite and other sedimentary units (Wylie et al., 1987).

Detachment and other faults focus hydrothermal fluid that transported ore metal to the seafloor environment. As seawater infiltrates through faults and fissures, it would leach metal from the ultramafic rock, get heated with depth, and rise back to the surface to precipitate the metal on the seafloor in the form of black smokers in a hydrothermal vent field. Similar

processes have been observed at the Rainbow vent field (Marques et al., 2006). The ore fluid contained Fe-Zn-Cu from leaching subsurface basalt, and Co-Ni by leaching of subsurface ultramafic rock. Ultramafic origins would also explain the paucity of minerals such as galena and arsenopyrite, because ultramafic rocks are deficient in Pb and As relative to felsic rocks. Sulfur in chalcopyrite analyzed from Mineral Hill further support seawater origins (Robert R. Seal II, personal communication).

The ultramafic detritus would move further from the spreading center towards the subduction zone outboard of Laurentia (proto-North America). The nature of the metasedimentary rocks (i.e. metapelites) at Mineral Hill suggests proximity to an island arc, which in this case may have been the Chopawamsic volcanic terrane accreted during the Taconian orogeny. As part of a subduction complex in an accretionary environment, the material may have been further deformed when exposed to turbidites and olistostromal processes off Laurentia's coast, accounting for the metagraywacke at Mineral Hill. Following accretion to Laurentia, the rocks composing Mineral Hill would have been exposed to the multiple orogenic events constituting the Acadian and Alleghanian orogenies, further deforming the rocks and their primary features.

The presence of mafic rock and their associated textures (e.g. pillow lava) are common features of spreading centers. Mafic rock does not appear to be a dominant feature at Mineral Hill. However, the remnants of mafic material may be expressed in the amphibolite in the Morgan Run Formation, or perhaps was originally a small magmatic component (as is typical of an ultra-slow spreading center [Dick et al., 2008]).

4.5 Conclusions

This study was performed to better characterize the mineral deposit at Mineral Hill and to identify the characteristics that can be used as exploration vectors to locate similar deposits elsewhere. Increasingly few world class deposits are found worldwide every year despite a general increase in exploration spending (Hronsky and Groves, 2008). This suggests that traditional means of exploration are becoming less effective due to certain strategies and technologies reaching maturation and the limits of their potential. To ensure that resources and reserves are then sufficient to meet the needs of future generations, new exploration vectors must be identified and explored, and nowhere is this more important than under covered terranes.

Preliminary comparisons to other ore deposits show that no other ore deposits are equivalent to Mineral Hill in terms of mineralogy, although several, such as Eastern Metals and Outokumpu, bear striking similarities in terms of their tectonic environments, alteration features, and host lithologies. The listwaenite-birbirite alteration characteristic of Eastern Metals and Outokumpu may be analogous to the banded iron oxide – quartz rock at Mineral Hill. In view of certain analogous deposits, such as Outokumpu and Blackbird, Mineral Hill is anomalously lacking in terms of Pb and As concentrations. The host *mélange* units at Mineral Hill contain clastics and debris that have, at least in part, a continental affinity. The paucity of Pb and As is likely due to the lack of felsic continental material in the source region for the mineralization suggesting a source with oceanic affinity.

Our understanding of the mineralogy of Mineral Hill is now more comprehensive. Several minerals (e.g. hessite, electrum, arsenopyrite) new to the assemblages have been identified through the use of BSE, EDS and WDS analyses by EPMA. The textures and minerals

present at Mineral Hill, such as tourmaline aggregates, and other characteristics listed by (Candela et al., 1989) suggest it may have been part of a black smoker complex on the seafloor. Textures such as zoned tourmaline, if primary depositional features and not products of retrograde metamorphism, may also represent disequilibria during mineral deposition.

WDS traverses indicate the presence of Pb, but not in concentrations high enough for the formation of a Pb-rich phase (e.g. galena). This is a feature similar to other proposed seafloor mineral deposits (Dergamysh, Main Uralian Fault). Of note in the WDS analysis is that MH2 sphalerite contains up to 7 wt % Cd which exhibits a slight negative correlation with Fe content. WDS traverses also indicate that chlorite and tourmaline do not appear to host ore metals (e.g. Cr, Zn) in notable abundance.

An overarching goal of this project is to better define exploration vectors to be used when searching for deposit similar to Mineral Hill. We now know through monazite dating that rocks of an Ordovician age, likely incorporated into a polygenetic mélangé during the Taconian Orogeny, can contain economic mineralization of Fe and Cu, with lesser quantities of Co and Ni, in association with ultramafic rocks; these results define an age, tectonic setting, and associated rock type as exploration vectors. We also know that the ore is associated with the serpentinized and detrital ultramafic material of an ancient VMS deposit that may be analogous to Mid-Atlantic Ridge deposits and oceanic core complexes. There may also have accompanying aeromagnetic anomalies due to the close association of magnetite (i.e. banded iron-oxide quartz rock) with the ore.

The mineral tourmaline also occurs near the ore horizon. This indirect association of aggregated tourmaline, which is commonly dravitic and derived from metapelites and

metapsammites, with the ore may give some indication of mineralization. These tourmalines are seemingly not derived from the ultramafic ore host-rock, but rather hydrothermal processes. As such, the compositional trend of Mg-rich cores to Fe-rich rims may indicate a possible exploration vector. Because it is a resistate mineral, tourmaline could also be collected in stream sampling for further analysis. A second indirect association to the ore is the occurrence of high-cadmium sphalerite, which also occurs in close proximity to the ore horizons. These signatures may be difficult to identify at a deposit as small as Mineral Hill. Moreover, these are all signatures that are identifiable, to a first approximation, in core sampling. In covered terranes, such as the Maryland Piedmont, such identifying characteristics can provide vectors for exploration.

Appendix

Tables A1 - A11 briefly characterizes mines that contain features similar to Mineral Hill.

Table A1

Deposit	Mineral Hill Mine
Location (Town/County, State/Province, Country)	Carroll County, MD, United States
Ore Elements (Mined for)	Fe-Cu
Trace Elements	Zn-Ni-Co
Gangue Elements	S
Ore Element Geochemistry	NA
Trace/Misc Element Geochemistry	NA
Tonnage (of what/where)	NA
Grade (of what)	NA
Production	>18,300 tons Fe ore, ~7500 tons metallic Cu ore
Ore Host Formation and Lithology	Morgan Run formation metaclastic mélange with massive to lensoidal ultramafic clasts, pelitic schist with interlayered amphibolite and metagraywacke, and banded iron
Bounding Strata	(below) Marburg Formation phyllite, metasilstone, quartzite, (above) Sykesville formation metadiamictite and pelitic schist
Ore Mineralogy	magnetite, chalcopryrite, siegenite, pyrite, sphalerite, chalcocite, arsenopyrite, chromite
Gangue Mineralogy	plagioclase, hornblende, quartz, clinozoisite, chlorite, biotite, muscovite, talc, dolomite
Trace Mineralogy	monazite, allanite, apatite, zircon

Ore Alteration Halo	Serpentinization; blackwall zone
Misc. Alteration	Chloritization, talc
Ore Body Shape	NA
Type of Mineralization	Contact, massive
Ore Textures	Dendritic chalcopyrite
Age Range (Numerical/Stratigraphic)	Taconian
Tectonic Setting	Orogen
Depositional Setting	Tectonic mélange
Regional Structures	NA
Local Structures	Thrust faulting
Temp. of Formation	NA
Inclusion Data	NA
Metamorphic Grade	Amphibolite
Crystals syn/epigenetic	Syngenetic sulfides and epigenetic alteration
VMS Label	Besshi
Mode of Formation	NA
Magma Involvement	Ultramafic
Misc.	Ore zones are in contact with blackwall and banded iron formations.

References:	<p>Candela, P. A., Wylie, A. G., and Burke, T. M., 1989, Genesis of the ultramafic rock-associated Fe-Cu-Co-Zn-Ni deposits of the Sykesville District, Maryland Piedmont: Economic Geology and the Bulletin of the Society of Economic Geologists, v. 84.3, p. 663-675</p> <p>Muller, P. D., Candela, P. A., Wylie, A. G., 1989, Liberty Complex; polygenetic mélangé in the central Maryland Piedmont: Geological Society of America Special Papers, v. 228, p. 113-134</p> <p>Burke, T. M., 1987, The petrology and chemistry of detrital ultramafic material at the Mineral Hill mine, Sykesville mining district, Maryland, and the role of accessory chromite in determining the origin of the body and associated sulfide ores: Unpublished M.Sc. thesis, Maryland, United States, University of Maryland, p. 187</p>
--------------------	---

Table A2

Deposit	Bou Azzer (Bou Azer)
Location (Town/County, State/Province, Country)	Taznakht, Ouarzazate, Morocco
Ore Elements (Mined for)	Co-Ni-Fe
Trace Elements	Cu
Gangue Elements	As
Ore Element Geochemistry	(Ore) 2,800 ppm Ni, (veins) 10,000 ppm Ni, Co: 3,000 ppm Co, (serpentinite) 76 ppm Co
Trace/Misc Element Geochemistry	Cu: 8 - 2000 ppb; As: 10 - 45 ppm (in Serpentinite)
Tonnage (of what/where)	NA
Grade (of what)	NA

Production	NA
Ore Host Formation and Lithology	Serpentinized harzburgites with minor dunite and small-scale chromite pods
Bounding Strata	Quartz diorite intrusions, overlain by layered late-proterozoic volcano-sedimentary series
Ore Mineralogy	skutterudite, safflorite, loellingite, nickeline, rammelsbergite, Bornite, chalcocite, chalcopyrite, pyrite, pyrrhotite, sphalerite, tetrahedrite. No native silver.
Gangue Mineralogy	quartz, dolomite, ankerite, calcite, Talc, chlorite, and serpentine
Trace Mineralogy	magnetite, chromian spinel
Ore Alteration Halo	Serpentinite carbonization, silicification, and talc-rich zones
Misc. Alteration	Hydrothermal; quartz diorite chloritization, silicification, carbonization
Ore Body Shape	Lenses, veins, seams, stockworks
Type of Mineralization	Contact, massive
Ore Textures	NA
Age Range (Numerical/Stratigraphic)	~640 Ma (Neoproterozoic)
Tectonic Setting	Orogen (Variscan/Hercynian)
Depositional Setting	NA
Regional Structures	Dome and Basin topography
Local Structures	Layered Ophiolite
Temp. of Formation	"High" and "low" stages
Inclusion Data	NA
Metamorphic Grade	NA

Crystals syn/epigenetic	Five stages of mineralization (in chronological order from earliest): Ni-rich, Co-rich, Fe rich, sulfarsenide, sulfide
VMS Label	NA
Mode of Formation	NA
Magma Involvement	Felsic intrusions
Misc.	No native Ag is present. The highest grade orebodies are associated with intense deformation. Ore mineralization is limited to quartz-carbonate altered serpentinite margins. Co-Ni arsenides appear to have formed between serpentinite and quartz diorite.933008
References:	Ahmed, A H, Arai, S., and Ikenne, M., 2009, Mineralogy and Paragenesis of the Co-Ni Arsenide Ores of Bou Azzer, Anti-Atlas, Morocco: Economic Geology. 104.2: 249-266.

Table A3

Deposit	Outokumpu
Location (Town/County, State/Province, Country)	Outokumpu, Eastern Finland, Finland
Ore Elements (Mined for)	Cu-Co-Zn-Au
Trace Elements	Ni-Ag
Gangue Elements	C
Ore Element Geochemistry	(Kylyyahti prospect) 2.6 wt.% Cu, 0.76 wt.% Zn and 0.39 wt.% Co, 0.13 Ni, and 0.9 g/t Au

Trace/Misc Element Geochemistry	25.3 wt.% S, 0.015 wt.% Sn, 0.005 wt.% Pb, ~0.050 wt.% Mn, 5 ppm Hg
Tonnage (of what/where)	Current (Kyllylahti): 7.85 Ma tons
Grade (of what)	1.17 wt.% copper, 0.24 wt.% cobalt, 0.22 wt.% nickel, 0.48 wt.% zinc, and 0.70 g/t gold
Production	1913-1989: ~28 Mt ore averaging 3.8 wt.% Cu, 1 wt.% Zn and 0.24 wt.% Co, 0.12 Ni, and 0.8 g/t Au
Ore Host Formation and Lithology	Metamorphosed and metasomatized ultramafic massifs enclosed in carbonate
Bounding Strata	Siliceous quartzitic schist; black schist, metaturbidites
Ore Mineralogy	chalcopyrite, pyrrhotite, pyrite, sphalerite, cobaltian pentlandite, stannite, mackinwaite
Gangue Mineralogy	graphite, olivine, tremolite, dolomite, diopside, antigorite, magnesite, talc, rutile, titanite, tucholite
Trace Mineralogy	epidote (tawmawite, allanite), uvarovite, Cr-tourmaline, phlogopite, fuchsite
Ore Alteration Halo	NA
Misc. Alteration	NA
Ore Body Shape	Generally ruler-shaped sheet; lenses bordering skarn-carbonates, skarn-hosted disseminations
Type of Mineralization	Semimassive-massive layered and/or brecciated sulfides
Ore Textures	Chalcopyrite with cubanite lamellae, banded (with quartz) pyrite, pyrite+chalcopyrite blebs in granoblastic quartz matrix, granular pyrrhotite-magnetite ore
Age Range (Numerical/Stratigraphic)	~1.925 Ma (Rhyacian)
Tectonic Setting	Orogen (obduction; Svecofennian)

Depositional Setting	Nearcontinent reducing environment; passive margin
Regional Structures	Thrust belt
Local Structures	Faulted Lense
Temp. of Formation	NA
Inclusion Data	NA
Metamorphic Grade	Lower-Upper Amphibolite (500° to 775°C, at 3–5 kbar)
Crystals syn/epigenetic	Polygenetic
VMS Label	NA
Mode of Formation	Serpentinite was dismembered and tectonically distributed throughout metaturbidites
Magma Involvement	NA
Misc.	Harker diagram trends of major and trace elements indicate mantle peridotite source rock. Selvages of thin carbonate-skarn-quartz rocks exist around serpentinite bodies. Serpentinite-carbonate-skarn-quartz rock assemblages may be analogous to listwaenite-birbirite alteration
References:	Peltola, E., 1978, Origin of Precambrian Copper Sulfides of the Outokumpu District, Finland: Economic Geology, v. 73.4, p.461-477. Peltonen, P, Kontinen, A., Huhma, H., and Kuronen, U., 2008, Outokumpu Revisited: New Mineral Deposit Model for the Mantle Peridotite-Associated Cu-Co-Zn-Ni-Ag-Au Sulphide Deposits: Ore Geology Reviews, v. 33, p. 559-617.

Table A4

Deposit	North Eastern Metals
Location (Town/County, State/Province, Country)	St-Fabien-de-Panet, Quebec, Canada

Ore Elements (Mined for)	Ni
Trace Elements	Zn
Gangue Elements	C
Ore Element Geochemistry	NA
Trace/Misc Element Geochemistry	NA
Tonnage (of what/where)	354,345 tons Ni (Reserves)
Grade (of what)	0.91 wt.% Ni
Production	Not mined
Ore Host Formation and Lithology	St. Daniel mélange and serpentinite
Bounding Strata	Graphitic schist, mélange
Ore Mineralogy	pyrite, violarite-polybdenite, millerite; subordinate sphalerite, chalcopyrite, magnetite
Gangue Mineralogy	quartz, ankerite, calcite
Trace Mineralogy	fuchsite, mariposite, gersdorffite
Ore Alteration Halo	Contacts are surrounded by 5-25m of talc, silicified, or carbonitized rock that grades from sulfide to talc-carbonate schist, to listwaenite, to birbirite, to sedimentary contact.
Misc. Alteration	Hydrothermal CO ₂ -Ca-S-As alteration
Ore Body Shape	Lenses
Type of Mineralization	NA

Ore Textures	NA
Age Range (Numerical/Stratigraphic)	Cambro-Ordovician
Tectonic Setting	Orogen (obduction; Taconian)
Depositional Setting	Tectonic mélange; reducing environment; flysch sequences present
Regional Structures	Brompton-Baie Verte lineament
Local Structures	Ophiolite slice
Temp. of Formation	<350 °C
Inclusion Data	NA
Metamorphic Grade	Greenschist
Crystals syn/epigenetic	NA
VMS Label	NA
Mode of Formation	NA
Magma Involvement	Nearby tholeiitic basalts; local granodiorite dikes
Misc.	Birbirite and listwaenite alteration is present. The deposit is relatively unmetamorphosed.
References:	Auclair, M, Gauthier, M., Trottier, J., Jebrak, M., and Chartrand, F., 1993, Mineralogy, Geochemistry, and Paragenesis of the Eastern Metals Serpentinite-Associated Ni-Cu-Zn Deposit, Quebec Appalachians: Economic Geology. v. 88.1, p. 123-138.

Table A5

Deposit	South Eastern Metals
Location (Town/County, State/Province, Country)	St-Fabien-de-Panet, Quebec, Canada
Ore Elements (Mined for)	Ni-Cu
Trace Elements	Zn-Co-Au
Gangue Elements	C
Ore Element Geochemistry	NA
Trace/Misc Element Geochemistry	NA
Tonnage (of what/where)	870,200 tons Ni+Cu (Reserves)
Grade (of what)	1.52 wt.% Cu, 0.15 wt.% Ni
Production	Not mined
Ore Host Formation and Lithology	St. Daniel mélange and serpentinite
Bounding Strata	Graphitic schist, mélange
Ore Mineralogy	pyrite, chalcopyrite; subordinate cobaltite, galena, sphalerite
Gangue Mineralogy	dolomite, calcite, quartz
Trace Mineralogy	cubanite, loellingite
Ore Alteration Halo	Contacts are surrounded by 5-25m of talc, silicified, or carbonitized rock that grades from sulfide to talc-carbonate schist, to listwaenite, to birbirite, to sedimentary contact.
Misc. Alteration	Hydrothermal CO ₂ -Ca-S-As alteration
Ore Body Shape	Lenses

Type of Mineralization	NA
Ore Textures	NA
Age Range (Numerical/Stratigraphic)	Cambro-Ordovician
Tectonic Setting	Orogen (obduction; Taconian)
Depositional Setting	Tectonic mélangé; reducing environment; flysch sequences present
Regional Structures	Brompton-Baie Verte lineament
Local Structures	Ophiolite slice
Temp. of Formation	>250 °C
Inclusion Data	NA
Metamorphic Grade	Greenschist
Crystals syn/epigenetic	NA
VMS Label	NA
Mode of Formation	NA
Magma Involvement	Nearby tholeiitic basalts; local granodiorite dikes
Misc.	Birbrite and listwaenite alteration is present. The deposit is relatively unmetamorphosed.
References:	Auclair, M, Gauthier, M., Trottier, J., Jebrak, M., and Chartrand, F., 1993, Mineralogy, Geochemistry, and Paragenesis of the Eastern Metals Serpentinite-Associated Ni-Cu-Zn Deposit, Quebec Appalachians: Economic Geology. v. 88.1, p. 123-138.

Table A6

Deposit	Ishkinino
Location (Town/County, State/Province, Country)	Main Ural Fault Zone, the southern Urals
Ore Elements (Mined for)	Cu
Trace Elements	Co-Ni-Au
Gangue Elements	NA
Ore Element Geochemistry	NA
Trace/Misc Element Geochemistry	0.13–0.49 wt.% Ni, 0.01–0.31 wt.% Co
Tonnage (of what/where)	NA
Grade (of what)	NA
Production	NA
Ore Host Formation and Lithology	NA
Bounding Strata	Polymict breccias containing felsic-ultramafic clasts
Ore Mineralogy	NA
Gangue Mineralogy	NA
Trace Mineralogy	cobaltite, gersdorffite, nickeline, safflorite, rammelsbergite, krutovite, pentlandite, violarite, arsenopyrite, löllingite, highly cobaltian violarite
Ore Alteration Halo	Serpentinization
Misc. Alteration	Pervasive serpentinization, local carbonate alteration
Ore Body Shape	Lenses

Type of Mineralization	Veins, banding
Ore Textures	NA
Age Range (Numerical/Stratigraphic)	NA
Tectonic Setting	NA
Depositional Setting	Seafloor; breccia
Regional Structures	Fault zone
Local Structures	Antiforms
Temp. of Formation	Homogenization: bimodal 135 °C & 175 °C
Inclusion Data	Exolution: 150–450 °C
Metamorphic Grade	Greenschist
Crystals syn/epigenetic	Epigenetic sulfides formed through replacement and veining of host rock
VMS Label	NA
Mode of Formation	NA
Magma Involvement	NA
Misc.	Structurally controlled with massive sulfides clustering at antiform limbs.
References:	Herrington, R., Maslennikov, V., Zaykov, V., Seravkin, I., Kosarev, A., Buschmann, B., Oregeval, J. J., Holland, N., Tesalina, S., Nimis, P., Armstrong R., 2005, Classification of VMS deposits: lessons from the South Uralides: Ore Geology Review, v. 27, p. 203–237.

Table A7

Deposit	Dergamysh
Location (Town/County, State/Province, Country)	Main Ural Fault Zone, the southern Urals
Ore Elements (Mined for)	NA
Trace Elements	Au
Gangue Elements	NA
Ore Element Geochemistry	NA
Trace/Misc Element Geochemistry	0.005–0.08 wt.% Ni and 0.006–0.25 wt.% Co
Tonnage (of what/where)	2 Mt (Cu)
Grade (of what)	Not disclosed
Production	NA
Ore Host Formation and Lithology	NA
Bounding Strata	NA
Ore Mineralogy	NA
Gangue Mineralogy	NA
Trace Mineralogy	NA
Ore Alteration Halo	NA
Misc. Alteration	NA
Ore Body Shape	Stacked lenses interfingering with thin layers of brecciated serpentinites and chloritized mafic rocks

Type of Mineralization	Rhythmically graded layers of clastic sulfides
Ore Textures	Colloform, concretionary, and framboidal pyrite-marcasite, "net-like" pyrrhotite, Chalcopyrite with cubanite and mackinawite lamellae
Age Range (Numerical/Stratigraphic)	NA
Tectonic Setting	NA
Depositional Setting	Seafloor-subseafloor transitional; recrystallized chimney materials
Regional Structures	NA
Local Structures	NA
Temp. of Formation	NA
Inclusion Data	NA
Metamorphic Grade	NA
Crystals syn/epigenetic	NA
VMS Label	NA
Mode of Formation	NA
Magma Involvement	NA
Misc.	Supersaturation textures are present along with detrital chromite. Gold occurs in chlorite matrix of pyrite–marcasite globules, in magnetite–chalcopyrite aggregates, in late anhedral chalcopyrite, or it forms small, 20 μm-thick veinlets cutting the marcasite–pyrite clasts.
References:	Herrington, R., Maslennikov, V., Zaykov, V., Seravkin, I., Kosarev, A., Buschmann, B., Oregeval, J. J., Holland, N., Tesalina, S., Nimis, P., Armstrong R., 2005, Classification of VMS deposits: lessons from the South Uralides: Ore Geology Review, v. 27, p. 203–237.

Table A8

Deposit	Ivanovka
Location (Town/County, State/Province, Country)	Main Ural Fault Zone, the southern Urals, Russia
Ore Elements (Mined for)	Cu
Trace Elements	Co-Ni
Gangue Elements	NA
Ore Element Geochemistry	NA
Trace/Misc Element Geochemistry	0.11–0.22 wt.% Ni and 0.02–0.08 wt.% Co
Tonnage (of what/where)	24 Mt Cu
Grade (of what)	0.88 wt.% Cu
Production	NA
Ore Host Formation and Lithology	Ultramafic-mafic (serpentinites-gabbros)
Bounding Strata	Graded sedimentary units
Ore Mineralogy	pyrrhotite associated with variable proportions of chalcopyrite, pyrite, sphalerite
Gangue Mineralogy	NA
Trace Mineralogy	pentlandite, violarite, cobaltite, alloclasite, arsenopyrite, highly cobaltian pentlandite, and gold, bismuth and Bi-tellurides
Ore Alteration Halo	Serpentinization
Misc. Alteration	NA
Ore Body Shape	Layers, lenses, veins, stockworks
Type of Mineralization	NA

Ore Textures	net-like pyrrhotite
Age Range (Numerical/Stratigraphic)	NA
Tectonic Setting	NA
Depositional Setting	Subseafloor
Regional Structures	Fault zone
Local Structures	block mélange
Temp. of Formation	Exolution: 150–450 °C
Inclusion Data	1.2-2.4 wt.% NaCl (low T), ~7.2 wt.% NaCl (high T)
Metamorphic Grade	Hydrothermal/metasomatism
Crystals syn/epigenetic	NA
VMS Label	NA
Mode of Formation	NA
Magma Involvement	NA
Misc.	NA
References:	Herrington, R., Maslennikov, V., Zaykov, V., Seravkin, I., Kosarev, A., Buschmann, B., Oregeval, J. J., Holland, N., Tesalina, S., Nimis, P., Armstrong R., 2005, Classification of VMS deposits: lessons from the South Uralides: Ore Geology Review, v. 27, p. 203–237.

Table A9

Deposit	Blackbird
Location (Town/County, State/Province, Country)	Blackbird Mine, Idaho, United States
Ore Elements (Mined for)	Co-Cu-Ag-Fe
Trace Elements	Y, REE, Bi, Ni, U
Gangue Elements	As
Ore Element Geochemistry	(Ore) All values are in parts per million (ppm) unless otherwise indicated; <i>nd</i> indicates mean was not calculated because of strongly skewed data. 6.6-18 (11.0) wt.% Fe; <1-1.5 (nd) Ag, 37-7 Co, 900 (180), 8-5,000 (250) Cu
Trace/Misc Element Geochemistry	(Ore) All values are in parts per million (ppm) unless otherwise indicated; <i>nd</i> indicates mean was not calculated because of strongly skewed data. <0.1-3.8 (0.2) wt.% S, 7-9,450 (130) As, <10-45 (nd) Bi, <1-<2 (nd) Cd, 22-170 (46) Cr, <1-5 (nd) Mo, 10-380 (33) Ni, 2-15 (2.8) Pb; <0.1-19 (9) Se, 5-19 (11) Th, 14-62 (27) Zn
Tonnage (of what/where)	14.343 million tonnes
Grade (of what)	Co: 0.58 %, Cu 1.24%, Au 0.58 g/t
Production	NA
Ore Host Formation and Lithology	Yellowjacket formation biotitite and, variably, bedded magnetite
Bounding Strata	quartzo-feldspathic meta-clastic strata and granite
Ore Mineralogy	cobaltite, chalcopyrite, pyrite, pyrrhotite, native gold, variable magnetite, lesser arsenopyrite, linnaeite, safflorite, ±native silver, ±enargite, ±sphalerite, ±galena
Gangue Mineralogy	biotite, garnet, chloritoid, tourmaline, muscovite, siderite
Trace Mineralogy	NA
Ore Alteration Halo	Potassic; pyrite-siderite-quartz-muscovite in the core zone grading to quartz-muscovite-(with lesser) pyrite
Misc. Alteration	Silicification, chloritization
Ore Body Shape	Stratabound
Type of Mineralization	Massive and disseminations

Ore Textures	Cobaltite is present in very fine grained layers and thin stringers. Chalcopyrite is present in coarsely crystalline stringers and aggregates commonly enveloping cobaltite. Pyrite is coarsely crystalline, has internal concentric banding, and some contains fine-grained pyrrhotite cores.
Age Range (Numerical/Stratigraphic)	NA
Tectonic Setting	Intracontinental extensional basin
Depositional Setting	Turbidite flows and, minimally, fine-grained marine sandstone
Regional Structures	NA
Local Structures	NA
Temp. of Formation	NA
Inclusion Data	NA
Metamorphic Grade	Greenschist-lower Amphibolite; locally up to Granulite
Crystals syn/epigenetic	NA
VMS Label	Besshi
Mode of Formation	NA
Magma Involvement	Coeval granite (a-type) and gabbro (alkali basalt to tholeiitic basalt) post-formation
Misc.	Tourmaline and tourmalinites are present. There is a well defined oxide zone around the ore. Bedded magnetite is presumed have formed from chemical sedimentation. Isotope analyses show the sulfur is primarily sedimentary in origin.
References:	Evans, K. V., Nash, J. T., Miller, W. R., Kleinkopf, M. D., & Campbell, D. L., 1995, Blackbird Co-Cu deposits: <i>U.S. Geol. Survey Open-File Rep.</i> 95-831, 145-151. Nold, J.L., 1990, The Idaho Cobalt Belt, Northwestern United States: a Metamorphosed Proterozoic Exhalative Ore District: <i>Mineralium Deposita.</i> v. 25.3.

Table A10

Deposit	Limassol Forest
Location (Town/County, State/Province, Country)	Pevkos & Lakxia tou Mavrou, Troodos ophiolite complex, Cyprus
Ore Elements (Mined for)	Cu-Ni-Co-Fe
Trace Elements	NA
Gangue Elements	As
Ore Element Geochemistry	NA
Trace/Misc Element Geochemistry	NA
Tonnage (of what/where)	NA
Grade (of what)	NA
Production	NA
Ore Host Formation and Lithology	Serpentinized harzburgite and subordinate dunite
Bounding Strata	NA
Ore Mineralogy	NA
Gangue Mineralogy	NA
Trace Mineralogy	mackinwaite, molybdenite, sphalerite, oregonite, gersdorffite, Ni-cobaltite, chromite, magnetite, ilmenite, rutile, goethite, graphite, gold
Ore Alteration Halo	NA
Misc. Alteration	NA
Ore Body Shape	Lenticular or irregular bodies and lenses of massive ore
Type of Mineralization	Disseminations and veins
Ore Textures	Cataclastic chromite with ferritchromite rims
Age Range (Numerical/Stratigraphic)	Late-cretaceous
Tectonic Setting	Subduction (obduction)
Depositional Setting	NA
Regional Structures	Arakapas transform fault
Local Structures	Ophiolite, fault zone

Temp. of Formation	400-500 °C arsenide phase followed by 250C sulfide phase
Inclusion Data	NA
Metamorphic Grade	NA
Crystals syn/epigenetic	NA
VMS Label	Cyprus
Mode of Formation	Emplacement followed by deformation and hydrothermal activity + serpentinization
Magma Involvement	Mafic
Misc.	High levels (>0.25wt%) of arsenic and presence of troilite; indications of tensional and compressional stress
References:	Foose, M., Economou, M., Panayiotou, A., 1985, Compositional and mineralogic constraints on the genesis of ophiolite hosted nickel mineralization in the Pevkos area, Limassol Forest, Cyprus: Mineralium Deposita, v.20, p. 234-240.

Table A11

Deposit	Windy Craggy
Location (Town/County, State/Province, Country)	St. Elias Mountains, NW British Columbia, Canada
Ore Elements (Mined for)	Cu-Ag-Co
Trace Elements	NA
Gangue Elements	NA
Ore Element Geochemistry	(North sulfide body averages) 29.3 wt.% Fe, 1.2 wt.% Cu, 0.1 wt.% Co, 1.6 g/t Ag, 0.2 g/t Au, (South sulfide body averages) 33.6 wt.% Fe, 1.3 wt.% Cu, 0.1 wt.% Co, 3.0 g/t Ag, 0.4 g/t Au,
Trace/Misc Element Geochemistry	(NSB averages) <5 wt.% Zn

Tonnage (of what/where)	113 Mt (Reserves '05)
Grade (of what)	1.9 % Cu, 3.9 g/t Ag and 0.08% Co
Production	NA
Ore Host Formation and Lithology	(Graphitic) Turbiditic argillites and intercalated intermediate-mafic flows of the Middle Tats Group
Bounding Strata	Interbedded graphitic and calcareous argillites and intermediate to mafic volcanic flows/dikes
Ore Mineralogy	pyrrhotite, pyrite, chalcopyrite, magnetite, lesser digenite, sphalerite, rare gold, electrum, marcasite, arsenopyrite
Gangue Mineralogy	quartz, albite chlorite, calcite, ankerite, siderite, stilpnomelane, biotite, graphite, stipnomelane
Trace Mineralogy	arsenopyrite, galena, valleriite, marcasite, cubanite, cobaltite, wehrlite, hedleyite, tellurobismuthinite
Ore Alteration Halo	Pervasive chloritization and silicification
Misc. Alteration	Chloritization, carbonatization
Ore Body Shape	Stockworks at syncline hinges and massive sulfides at limbs
Type of Mineralization	Massive, stringer zone
Ore Textures	Massive sulfide is often brecciated. Pyrite occurs as 1) colloform to framboidal spheres and 2) euhedral, equant cubes and pyritohedrons intergrown in boxwork fashion.
Age Range (Numerical/Stratigraphic)	Triassic (Norian)
Tectonic Setting	Accretion of the allochthonous Alexander terrane
Depositional Setting	Back-arc basin
Regional Structures	NA
Local Structures	Synclines
Temp. of Formation	NA
Inclusion Data	140-375 °C temperature of homogenization (quartz); ~12 wt.% NaCl fluid salinity
Metamorphic Grade	Up to greenschist
Crystals syn/epigenetic	NA
VMS Label	Besshi
Mode of Formation	NA
Magma Involvement	Intermediate-mafic

Misc.	Stratigraphic sulfide zoning: (moving from footwall stringer mineralization) massive pyrrhotite, to massive pyrrhotite-pyrite, to massive pyrite, to massive pyrite-calcite-sphalerite, ending in discontinuous chert-carbonate-sulphides. The deposit contains gold-bearing chert-carbonate-sulfide exhalite layer. Sulfide breccias thought to be indicative of talus from chimney collapse.
References:	Peter, J., 1999, Windy Craggy, northwestern British Columbia: the world's largest Besshi-type deposit: Reviews in Economic Geology, v. 8, p. 261-295

Tables A12 – A13 represent quantitative WDS analysis for Fe, In, As, S, As, Cd, Ag, Zn, Pb, Cu, Sn, Co, and Mn in sphalerite (A1.2.1) and chalcopyrite (A1.2.2) across two polished sections (MH2Y5, SpringX2) and two thin sections (MH2-06, MH1-32) taken from Mineral Hill drill cores 1 and 2 and the Springfield mine dump. These tables analyze for potential compositional anomalies and zoning of sulfide and oxide phases in Se, Cu, S, Fe, As, Ni, Pb, Co, Zn, and Mo. Data points, where totals beneath <98% existed were dropped from tabulation as they may represent areas with elemental compositions beyond those listed and/or areas of poor data collection. These unused data points represent 99 of 124 total points in Traverse 1 and 46 of 50 total points in traverse 2.

Table A12

Sample-Grain	Fe	In	S	As	Cd	Ag	Zn	Pb	Cu	Sn	Co	Mn	Total
MH2Y5 -1B	2.09	0.00	31.58	0.00	8.04	0.03	55.41	0.06	1.45	0.00	0.06	0.00	98.72
MH2Y5 -1B	2.48	0.00	31.53	0.00	7.85	0.02	55.31	0.09	1.92	0.00	0.04	0.00	99.23
MH2Y5-2B	1.90	0.00	31.28	0.00	8.72	0.01	56.12	0.07	1.24	0.00	0.04	0.00	99.38
MH2Y5-4G	4.52	0.03	32.37	0.00	5.01	0.05	54.14	0.08	5.67	0.00	0.02	0.01	101.90
MH2Y5-4G	1.84	0.00	31.54	0.00	8.90	0.00	57.08	0.05	1.27	0.00	0.05	0.00	100.72
MH2Y5-4G	1.35	0.01	31.84	0.00	7.02	0.02	58.97	0.07	0.84	0.03	0.04	0.01	100.18
MH2Y5-5G	1.54	0.00	31.52	0.01	7.54	0.09	58.06	0.07	0.93	0.00	0.04	0.00	99.79
SpringX2-1G	5.91	0.01	32.92	0.00	0.12	0.00	58.65	0.07	0.06	0.01	1.05	0.15	98.95
SpringX2-1G	5.74	0.00	32.79	0.00	0.12	0.00	58.90	0.08	0.03	0.00	1.01	0.14	98.81
SpringX2-2G	6.56	0.01	33.25	0.02	0.14	0.00	57.73	0.07	0.17	0.02	1.05	0.16	99.18
SpringX2-2B	6.91	0.00	33.57	0.00	0.15	0.00	56.18	0.05	3.27	0.01	0.77	0.06	100.98
SpringX2-4B	7.05	0.01	33.17	0.00	0.13	0.01	56.88	0.08	1.60	0.01	1.07	0.13	100.14
SpringX2-5B	4.51	0.00	32.66	0.01	0.11	0.00	59.74	0.08	0.16	0.01	0.81	0.05	98.13
SpringX2-7B	6.73	0.00	32.95	0.01	0.13	0.00	58.07	0.07	0.21	0.01	1.09	0.14	99.40
SpringX2-8B	6.50	0.00	32.94	0.00	0.13	0.00	58.31	0.08	0.21	0.00	1.03	0.15	99.36
SpringX2-8B	5.68	0.01	33.00	0.01	0.12	0.00	59.47	0.07	0.06	0.01	1.05	0.14	99.62
SpringX2-9B	6.32	0.01	33.30	0.00	0.12	0.00	58.56	0.07	0.08	0.00	1.04	0.16	99.67
SpringX2-10B	6.29	0.00	33.29	0.00	0.12	0.00	59.08	0.09	0.06	0.01	1.06	0.16	100.15
SpringX2-3G	7.53	0.00	35.73	0.00	0.09	0.00	52.24	0.05	1.72	0.01	1.00	0.15	98.51
MH2-06-1B	1.01	0.00	31.74	0.04	6.12	0.01	60.19	0.07	0.58	0.00	0.08	0.01	99.85

MH2-06-2B	1.08	0.00	32.09	0.00	5.21	0.00	60.92	0.07	0.62	0.00	0.18	0.00	100.16
MH2-06-3B	0.93	0.00	31.82	0.00	5.27	0.00	60.77	0.06	0.56	0.00	0.19	0.00	99.61
MH2-06-4B	1.02	0.00	32.01	0.00	6.01	0.01	60.11	0.05	0.52	0.00	0.06	0.00	99.80
MH2-06-5B	0.64	0.00	31.95	0.00	6.11	0.00	60.57	0.05	0.28	0.00	0.05	0.00	99.67
MH2-06-6B	1.14	0.00	31.85	0.00	6.72	0.01	59.65	0.05	0.67	0.00	0.06	0.00	100.15
MH2-06-7B	1.64	0.00	31.69	0.00	7.74	0.01	58.24	0.04	1.04	0.00	0.04	0.00	100.44
MH1-32-1B	5.79	0.00	32.66	0.00	0.30	0.00	59.13	0.07	0.29	0.00	0.32	0.08	98.65
MH1-32-2B	5.65	0.01	32.72	0.00	0.31	0.00	59.25	0.08	0.28	0.00	0.30	0.07	98.66
MH1-32-3B	5.95	0.00	32.70	0.00	0.29	0.00	58.81	0.07	0.83	0.00	0.25	0.05	98.95
MH1-32-4G	5.33	0.00	32.73	0.00	0.25	0.00	59.66	0.07	0.10	0.00	0.51	0.08	98.76
MH1-32-5B	6.31	0.00	33.04	0.00	0.32	0.00	58.06	0.05	0.89	0.00	0.28	0.05	99.00

Table A13

Sample-Grain	Fe	In	S	As	Cd	Ag	Zn	Pb	Cu	Sn	Co	Mn	Total
MH2Y5-1B	30.09	0.00	34.15	0.00	0.00	0.02	0.02	0.10	35.43	0.01	0.02	0.00	99.85
MH2Y5-2M	30.63	0.00	34.46	0.00	0.00	0.02	0.02	0.09	35.21	0.01	0.03	0.00	100.48
MH2Y5-3T	31.04	0.00	34.57	0.00	0.00	0.02	0.02	0.09	35.28	0.01	0.03	0.00	101.07
MH2Y5-3T	30.97	0.01	34.69	0.00	0.01	0.01	0.02	0.10	35.31	0.01	0.04	0.00	101.15
MH2Y5-3T	31.08	0.00	34.49	0.00	0.00	0.02	0.03	0.09	35.27	0.00	0.02	0.00	101.00
MH2Y5-3T	30.92	0.00	34.45	0.00	0.01	0.03	0.03	0.09	35.35	0.01	0.03	0.00	100.92
SpringX2-1M	30.79	0.00	34.18	0.00	0.00	0.02	0.03	0.09	35.13	0.01	0.03	0.00	100.28
SpringX2-2M	30.64	0.01	34.27	0.00	0.00	0.00	0.04	0.09	35.32	0.00	0.03	0.00	100.41
MH2-06-1B	29.53	0.00	33.16	0.00	0.00	0.01	0.00	0.09	35.40	0.02	0.04	0.00	98.26
MH2-06-2T	31.05	0.00	34.37	0.00	0.00	0.06	0.03	0.09	35.20	0.00	0.03	0.00	100.83
MH2-06-2T	30.95	0.01	34.20	0.00	0.00	0.06	0.02	0.10	35.19	0.00	0.03	0.00	100.57
MH2-06-2T	30.89	0.00	34.52	0.00	0.00	0.05	0.03	0.09	35.26	0.00	0.04	0.01	100.89
MH2-06-2T	30.93	0.01	34.47	0.01	0.00	0.01	0.02	0.09	35.42	0.01	0.03	0.00	100.99
MH2-06-2T	30.87	0.01	34.21	0.01	0.00	0.01	0.03	0.11	35.20	0.01	0.04	0.00	100.48
MH2-06-2T	30.69	0.00	34.19	0.01	0.00	0.03	0.02	0.12	35.31	0.00	0.03	0.00	100.41

MH2-06-2T	30.74	0.00	34.24	0.00	0.00	0.00	0.02	0.08	35.41	0.01	0.03	0.01	100.55
MH1-32-1G	30.32	0.00	34.01	0.00	0.00	0.01	0.03	0.09	35.12	0.00	0.03	0.00	99.62
MH1-32-2G	30.14	0.01	33.85	0.00	0.00	0.00	0.02	0.10	35.20	0.00	0.03	0.00	99.37
MH1-32-3M	30.40	0.00	33.96	0.02	0.00	0.00	0.03	0.10	35.52	0.00	0.04	0.00	100.08
MH1-32-4M	30.27	0.01	33.92	0.00	0.00	0.00	0.05	0.10	35.32	0.00	0.04	0.00	99.70
MH1-32-5M	30.22	0.01	33.84	0.00	0.00	0.00	0.05	0.10	35.20	0.01	0.03	0.00	99.45

Tables A14 – A15 show the results of all WDS tourmaline analyses in wt % from all analyzed samples as well as their position in the tourmaline grain. Those lacking position data did not display readily observable zonation.

Table A14

Core- Section-Sample	Position	B2O3	FeO	F	CaO	Na2O	MnO	MgO	K2O	Al2O3	ZnO	TiO2	SiO2	Cr2O3	Total
MH1-03-1		10.61	8.12	0.41	1.34	2.11	0.02	9.06	0	28.68	0.03	0.92	35.61	0	96.93
MH1-03-1		10.65	7.67	0.19	1.33	2.16	0.02	9.1	0.01	28.72	0.02	0.78	35.43	0.01	96.09
MH1-03-1		11.25	8.93	0.26	1	1.86	0.01	6.52	0.01	31.97	0.02	0.47	34.84	0.01	97.14
MH1-03-1		11.04	9.66	0.18	0.83	2.15	0.02	7	0	29.75	0.02	0.62	35.1	0.02	96.39
MH1-03-1		11.07	9.59	0.27	0.95	1.66	0.03	5.38	0.02	32.68	0.03	0.6	34.71	0.03	97.01
MH1-03-2		11.96	10.42	0.14	0.6	1.67	0.03	4.47	0.02	33.05	0.04	0.46	34.65	0	97.52
MH1-03-2		11.75	10.99	0.09	0.47	2.01	0	5.04	0.04	31.22	0.02	0.67	34.65	0.06	97
MH1-03-2		12.51	10.1	0.07	0.64	1.69	0.02	4.73	0.02	33.25	0.01	0.47	34.67	0.01	98.2
MH1-03-3		11.48	10.11	0.14	0.49	1.98	0.02	5.24	0.01	32.42	0.04	0.44	35.05	0.04	97.46
MH1-03-4		11.92	10.41	0.12	0.48	2.1	0.03	5.04	0	31.95	0.07	0.77	35.02	0.02	97.92
MH1-03-4		11.39	19.01	0.03	0.44	2.05	0.15	1.56	0.06	28.34	0.06	0.27	33.05	0.01	96.43
MH1-03-3		11.33	7.96	0.08	1.23	1.61	0.02	6.1	0.03	32.18	0	1.03	34.25	0.1	95.91
MH1-03-3		11.81	8.56	0.08	0.56	1.87	0.02	5.62	0.01	31.67	0.01	0.41	36.61	0.02	97.26
MH1-03-3		11.56	10.14	0.13	0.97	1.64	0.01	5.11	0.02	32.1	0.03	0.66	34.46	0.02	96.85
MH1-19-1		11.92	8.23	0.15	0.59	2.08	0.03	6.95	0.03	31.96	0.01	0.38	35.18	0.03	97.55
MH1-19-1		12.07	8.11	0.25	0.53	2.15	0.01	6.91	0.03	32.81	0.01	0.4	36.25	0.01	99.55
MH1-19-2	Rim	11.93	8.51	0.06	0.23	2.19	c	5.69	0.06	33.55	0.01	0.52	34.95	0.03	97.74
MH1-19-2	Core	12	8.64	0.15	0.26	2.2	0.01	6.1	0.04	30.78	0.01	0.76	33.75	0.06	94.77
MH1-19-3	Core	12.31	7.89	0.22	0.7	1.88	0.05	6.86	0.04	32.79	0.02	0.44	35.33	0.02	98.57
MH1-19-4	Rim	13.04	8.4	0.2	0.67	2	0.04	6.69	0.05	32.29	0	0.46	35.08	0.04	98.98
MH1-19-4	Core	14.07	9.15	0	0.03	1.52	0	5.1	0.04	33.6	0.02	0.13	35.3	0.06	99.03
MH1-19-5		12.39	8.97	0.23	0.64	2.28	0.05	6.71	0.02	30.44	0.02	0.43	34.73	0	96.94

Core- Section-Sample	Position	B2O3	FeO	F	CaO	Na2O	MnO	MgO	K2O	Al2O3	ZnO	TiO2	SiO2	Cr2O3	Total
MH1-19-5		12.13	8.12	0.12	0.31	2.09	0.02	5.81	0.04	32.7	0	0.43	34.44	0.04	96.26
MH1-19-6	Core	11.58	7.74	0.27	0.32	1.93	0.05	6.61	0.01	33.2	0.05	0.23	35.69	0.02	97.69
MH1-19-6	Rim	11.61	8.08	0.06	0.37	1.95	0.02	6.58	0.02	32.8	0.03	0.31	35.36	0.03	97.23
MH1-19-7		12.1	9.07	0.09	0.12	2.04	0.03	6.01	0.02	32.82	0.03	0.2	35.62	0.03	98.17
MH1-19-7		11.5	8.93	0.01	0.21	1.86	0.03	5.61	0.03	33.83	0.02	0.43	35.31	0.05	97.83
MH1-14-1		12.23	7.02	0.2	0.44	2.2	0.05	7.63	0.04	30.7	0.03	0.22	35.68	0.02	96.45
MH1-14-2	Core	11.31	7.08	0.34	1.1	1.71	0.02	7.43	0.05	33.03	0.05	0.4	35.27	0.01	97.79
MH1-14-2	Rim	12.23	8.8	0.19	1.04	1.79	0.02	6.74	0.08	30.74	0.02	0.58	34.08	0.01	96.31
MH1-14-3	Core	11.37	8.57	0.17	0.77	1.96	0.02	6.41	0.05	32.53	0.04	0.41	35.44	0.02	97.77
MH1-14-3	Rim	12.57	8.54	0.21	0.95	2.19	0.04	6.9	0.04	32.84	0	0.53	36.4	0.05	101.25
MH1-14-4	Core	11.03	9.16	0.13	0.23	2.24	0.04	6.27	0.03	31.06	0.02	0.82	34.65	0.08	95.77
MH1-14-4	Rim	10.92	8.73	0.15	1	1.94	0.01	6.89	0.04	32.65	0.03	0.54	36.17	0.02	99.08
MH1-14-5		11.49	8.71	0.15	0.92	1.97	0.02	6.71	0.03	32.03	0.04	0.55	35.25	0.03	97.91
MH1-14-5		11.49	8.86	0.18	0.98	1.93	0.01	6.75	0.03	31.65	0.04	0.59	34.84	0.01	97.36
MH1-14-6	Core	11.09	8.5	0.15	0.71	2	0.01	6.61	0.03	32.48	0.02	0.42	35.43	0.02	97.47
MH1-14-6	Rim	12.26	7.79	0.11	0.89	1.85	0.05	7.02	0.04	32.54	0.02	0.45	35.04	0.05	98.09
MH1-14-7	Core	11.61	8.37	0.08	0.17	2.19	0.06	6.68	0.04	32.56	0.05	0.19	35.78	0.02	97.79
MH1-14-7	Rim	11.48	7.35	0.21	0.85	2.1	0.06	7.72	0.05	33.48	0.03	0.47	36.79	0.01	100.59
MH1-13-1	Core	12.36	9.49	0.11	0.29	1.97	0.04	5.52	0.02	32.21	0.03	0.31	35.09	0.01	97.47
MH1-13-1	Rim	12.16	8.27	0.17	0.8	1.82	0.06	6.29	0.02	32.77	0.05	0.47	34.9	0.05	97.82
MH1-13-2	Core	11.65	9.53	0.17	0.26	1.8	0.02	5.12	0.02	33.39	0.03	0.28	35.51	0.01	97.8
MH1-13-2	Rim	12.18	8.86	0.23	0.92	1.84	0.03	6.29	0.02	32.28	0.01	0.47	35.02	0.01	98.17
MH1-13-3	Core	12.21	1.71	0.45	1.81	1.77	0	11.79	0.04	29.7	0	2.36	36.47	0.02	98.34
MH1-13-3	Zone	12.33	4.08	0.6	1.82	1.94	0	11.16	0.06	28.31	0.02	2.44	35.78	0.01	98.56
MH1-13-3	Rim	11.86	9.26	0.08	0.5	1.99	0.01	5.65	0.03	33.29	0.02	0.5	35.39	0.03	98.61

Core- Section-Sample	Position	B2O3	FeO	F	CaO	Na2O	MnO	MgO	K2O	Al2O3	ZnO	TiO2	SiO2	Cr2O3	Total
MH1-13-4	Core	12.25	8.95	0.27	0.69	1.99	0.02	6.19	0.03	32.52	0.01	0.46	35.4	0.03	98.8
MH1-13-4	Rim	11.77	8.64	0.19	0.79	1.9	0.02	6.35	0.03	32.73	0	0.36	35.3	0.02	98.1
MH1-13-5	Core	11.04	8.46	0.28	1.15	1.89	0.03	6.76	0.03	31.04	0.02	0.54	33.04	0.06	94.34
MH1-13-5	Rim	11.14	8.72	0.3	1.22	1.8	0.04	6.93	0.02	30.47	0.03	0.59	32.76	0.03	94.06
MH1-13-5	Rim	11.37	8.53	0.24	1.18	1.86	0.01	6.77	0.02	31.06	0.03	0.5	32.92	0.02	94.52
MH1-07-1	Core	12.15	6.43	0.32	0.86	1.71	0.05	7.26	0.01	32.22	0.04	0.36	34.22	0.01	95.65
MH1-07-1	Rim	15.93	6.76	0.47	0.88	1.58	0.04	7.27	0.02	29.81	0.04	0.42	31.73	0.02	94.96
MH1-07-2		12.16	7.07	0.25	0.52	1.96	0.05	6.99	0.02	31.8	0.02	0.26	34.46	0.01	95.55
MH1-07-2		13.38	6.77	0.44	0.93	1.88	0.04	7.49	0.03	32.79	0.02	0.39	35.09	0.02	99.27
MH1-07-3		12	6.48	0.11	0.76	1.79	0.04	7.04	0.19	32.56	0.02	0.34	35.05	0.01	96.4
MH1-07-3		17.18	7.38	0.31	0.9	1.42	0.04	7.09	0.03	29.27	0.02	0.44	30.41	0	94.51
MH1-43-1		11.94	5.77	0.17	0.5	2.09	0.08	7.75	0.05	33.17	0.45	0.28	35.3	0.11	97.65
MH1-43-1		12.68	7.06	0.39	0.57	2.31	0.07	8.39	0.04	30.29	0.05	0.5	35.47	0.01	97.83
MH2-15a-1	Core	12.81	7.41	0	0.9	1.93	0.03	6.8	0.02	33.06	0.04	0.64	35.4	0	99.05
MH2-15a-1	Rim	12.09	9.24	0.08	0.68	2.21	0.02	6.56	0.03	30.85	0.02	0.61	35.93	0.04	98.35
MH2-15a-2	Core	11.8	6.72	0	0.74	1.85	0.02	6.46	0.04	32.75	0.01	0.62	34.66	0	95.66
MH2-15a-2	Zone	12.5	5.82	0.03	0.44	1.68	0.02	6.41	0.02	34.01	0.04	0.16	35.23	0.01	96.38
MH2-15a-2	Rim	11.95	6.44	0.01	0.9	1.88	0.03	7.09	0.02	32.57	0.04	0.37	34.71	0	96.01
MH2-15a-4	Rim	10.99	8.95	0.01	0.59	2.1	0.03	6.31	0.02	29.87	0.04	0.71	34.82	0	94.43
MH2-15a-5	Core	10.86	5.18	0	0.37	1.61	0.02	6.94	0.03	33.67	0.01	0.06	35.49	0	94.23
MH2-15a-5	Zone	11.1	6.6	0	0.93	1.81	0.03	6.82	0.01	32.73	0.01	0.41	33.8	0.01	94.26
MH2-15a-5	Rim	10.82	9.05	0	0.51	2.18	0.01	5.95	0.03	30.24	0.01	0.59	34.66	0.02	94.05
MH2-15a-6	Core	11.32	6.76	0	0.9	1.77	0.03	6.7	0.01	32.09	0.01	0.57	34.03	0.02	94.21
MH2-15a-6	Rim	10.5	9.73	0	0.61	2.22	0.01	6.02	0.03	29.65	0.03	0.24	35	0	94.03
MH2-15a-7	Core	11.1	6.64	0.01	0.95	1.79	0.02	6.47	0.02	33.78	0.05	0.36	34.64	0.01	95.85

Core- Section-Sample	Position	B2O3	FeO	F	CaO	Na2O	MnO	MgO	K2O	Al2O3	ZnO	TiO2	SiO2	Cr2O3	Total
MH2-15a-7	Rim	11.67	6.61	0	0.82	1.89	0.03	6.59	0.03	32.74	0.01	0.38	34.68	0.02	95.46
MH2-15a-8	Core	11.94	6.56	0	0.84	1.88	0.02	6.96	0.01	31.09	0.02	0.4	33.65	0.01	93.39
MH2-15a-8	Rim	11.28	6.8	0	0.98	1.73	0.03	6.62	0.02	32.8	0.01	0.48	34.34	0	95.11
MH2-43-1	Zone	10.88	5.8	0.07	0.57	1.49	0.03	6.63	0.02	32.56	0.03	0.24	35.65	0.01	93.98
MH2-43-1	Rim	10.98	6.74	0.17	0.58	1.89	0.04	6.54	0.04	31.94	0.04	0.39	35.3	0.04	94.69
MH2-43-2	Core	11.27	8.53	0.09	0.26	2.02	0.04	6.09	0.02	30.88	0.03	0.27	35.96	0	95.47
MH2-43-2	Rim	11.46	6.53	0.07	0.76	1.92	0.04	7.12	0.03	32.11	0.01	0.43	35.51	0.04	96.03
MH2-43-3	Core	11.47	8.13	0.14	0.95	1.95	0.04	6.81	0.04	29.94	0.02	0.5	35.2	0.01	95.2
MH2-43-3	Rim	11.07	8.34	0.09	0.99	1.92	0.03	6.86	0.04	29.77	0.02	0.55	35.37	0.04	95.07
MH2-43-4	Core	11.88	8.03	0.19	0.87	1.88	0.02	6.77	0.03	30.43	0.03	0.51	35.29	0.03	95.95
MH2-43-4	Rim	12.12	7.92	0.12	0.9	1.83	0.03	6.77	0.04	30.61	0.02	0.55	35.56	0.01	96.49
MH2-43-5	Core	11.73	7.56	0.16	0.36	1.94	0.03	5.03	0.04	33.2	0.02	0.95	35	0.01	96.05
MH2-43-5	Zone (1)	11.3	8.93	0.08	0.27	1.85	0.04	3.91	0.06	33.38	0.03	0.91	35.21	0	95.95
MH2-43-5	Zone (2)	11.11	8.62	0.02	0.28	1.84	0.06	4.13	0.05	32.98	0.05	0.82	34.98	0.01	94.94
MH2-43-5	Zone (3)	11.81	9.23	0.03	0.38	2.1	0.02	5.42	0.02	31.12	0.03	0.63	35.44	0.01	96.24
MH2-43-5	Rim	11.98	6.5	0.08	0.82	1.8	0.02	7.09	0.02	32.59	0.03	0.42	35.89	0	97.22
MH2-43-6	Zone	10.95	8.37	0.02	0.25	1.81	0.04	3.87	0.05	33.09	0.02	0.85	34.73	0	94.06
MH2-43-6	Rim	12.07	6.52	0.09	0.86	1.68	0.03	6.87	0.02	32.33	0.04	0.41	35.69	0	96.61
MH2-43-7	Core	11.65	8.5	0.12	0.3	1.88	0.05	4.36	0.05	32.92	0	0.8	35.39	0	96.02
MH2-43-7	Zone	10.93	9.47	0.12	0.26	2.18	0.02	5.54	0.02	30.4	0.01	0.37	35.65	0.01	94.98
MH2-43-7	Rim	11.72	6.35	0.14	0.71	1.82	0.03	7.12	0.02	32.2	0.03	0.41	35.83	0	96.38
MH2-17-1	Core	10.69	7.86	0	0.58	1.74	0.01	5.52	0.03	32.33	0.03	0.13	35.31	0.01	94.23
MH2-17-1	Zone	11.48	8.6	0.02	0.77	1.74	0.02	5.38	0.01	32.2	0.04	0.42	35.32	0	95.98
MH2-17-1	Rim	10.87	7.2	0.03	1.02	1.91	0.04	6.85	0.02	31.59	0.03	0.43	35.34	0	95.33
MH2-17-2	Rim	12.01	7.26	0.09	1.05	1.87	0.03	6.9	0.02	31.54	0.05	0.46	35.19	0.05	96.5

Core- Section-Sample	Position	B2O3	FeO	F	CaO	Na2O	MnO	MgO	K2O	Al2O3	ZnO	TiO2	SiO2	Cr2O3	Total
MH2-17-3	Core	11.68	7.19	0.02	0.43	1.9	0.01	5.7	0.01	32.92	0.05	0.34	35.6	0.04	95.9
MH2-17-3	Rim	12.24	8.61	0.02	0.88	1.88	0.02	5.63	0.03	31.53	0.07	0.45	35	0.02	96.38
MH2-17-4	Core	11.65	8.69	0.04	0.75	1.74	0.01	5.35	0.02	31.96	0.02	0.41	35.22	0.01	95.86
MH2-17-4	Rim	11.44	7.63	0.04	0.88	1.93	0.01	6.56	0.03	31.44	0.02	0.45	35.29	0.02	95.73
MH2-17-5	Core	11.97	9.16	0.07	0.98	1.68	0.03	5.7	0.02	31.24	0.04	0.46	35.29	0.03	96.67
MH2-17-5	Rim	11.93	7.46	0	1.09	1.69	0.02	7.01	0.03	31.41	0.04	0.53	35.42	0.03	96.67
MH2-17-6	Core	11.83	8.78	0.11	0.98	1.68	0.02	5.77	0.02	31.68	0.04	0.49	35.14	0.01	96.57
MH2-17-6	Rim	12.3	8.64	0	0.92	1.74	0.02	5.82	0.03	31.91	0.05	0.48	35.39	0.02	97.32
MH2-17-7	Core	11.86	7.26	0	0.91	1.76	0.03	6.89	0.03	31.71	0.04	0.31	35.32	0.02	96.12
MH2-17-7	Rim	12.05	7.4	0.05	0.68	2.01	0.01	7.08	0.02	31.46	0.05	0.49	36.09	0	97.4
MH2-17-8		12.32	8.32	0.01	0.7	2.01	0	5.71	0.01	32.01	0.05	0.53	35.16	0.13	96.96
MH2-15b-1	Core	11.92	6.6	0	1.02	1.92	0.03	7.13	0.01	32.15	0.02	0.42	35.42	0.03	96.66
MH2-15b-1	Zone	11.75	9.41	0	0.65	2.22	0.01	6.16	0.01	29.45	0	1.09	35.41	0	96.16
MH2-15b-1	Rim	12	8.25	0	0.8	2	0.03	6.24	0.02	31.24	0.03	0.58	35.15	0.01	96.34
MH2-15b-2		11.42	7.05	0.07	0.82	1.82	0.02	6.35	0.01	32.52	0.02	0.79	34.6	0.02	95.51
MH2-15b-2		11.89	7.63	0.08	0.72	1.81	0.02	6.31	0.02	32.1	0.04	0.67	35.7	0.02	96.99
MH2-15b-3		10.84	8.9	0.04	0.4	2.11	0.01	6.02	0.02	31.21	0.02	0.32	36.27	0.02	96.19
MH2-15b-3		11.19	6.41	0.02	0.6	1.71	0.02	6.47	0.01	33.27	0	0.5	35.76	0	95.95
MH2-15b-3		10.55	6.5	0	0.73	1.68	0.02	6.42	0.02	33.18	0.01	0.43	35.57	0.02	95.11
MH2-15b-3		10.56	6.71	0.02	0.72	1.76	0.01	6.6	0.02	32.43	0	0.75	35.38	0	94.97
MH2-15b-3		11.35	7.01	0	0.83	1.83	0.02	6.41	0.01	32.66	0.03	0.83	35.48	0.01	96.46
MH2-15b-3		10.94	6.19	0	0.66	1.71	0.03	6.73	0.02	33.24	0.01	0.37	35.93	0.02	95.84
MH2-15b-3		10.51	6.42	0.06	0.85	1.94	0.03	6.68	0.02	33.01	0.01	0.36	35.61	0.01	95.49
MH2-15b--4	Core	12.27	6.62	0	0.81	1.74	0.03	6.56	0.01	33.41	0.02	0.51	35.17	0.01	97.17
MH2-15b-4	Zone	12.81	6.82	0.03	0.84	1.83	0.03	6.67	0.01	32.76	0.05	0.61	35.27	0.02	97.76

Core- Section-Sample	Position	B2O3	FeO	F	CaO	Na2O	MnO	MgO	K2O	Al2O3	ZnO	TiO2	SiO2	Cr2O3	Total
MH2-15b-4	Rim	12.97	7.65	0.06	0.8	1.88	0.01	6.19	0.02	32.42	0.01	0.56	35.42	0.02	98.01
MH2-15b-6	Rim	11.62	9.9	0.01	0.5	2.31	0.01	6.06	0.02	30.04	0.05	0.86	36.15	0	97.52
MH2-15b-7		12.28	9.35	0	0.75	2.2	0.03	6.32	0.03	29.37	0.02	0.69	35.16	0.01	96.2
MH2-15b-9	Core	11.77	6.99	0.01	0.91	1.79	0.01	6.62	0.01	33.06	0.03	0.73	35.52	0.02	97.49
MH2-15b-9	Rim	11.85	8.43	0.04	0.89	1.96	0	6.17	0.03	31.83	0.03	0.51	35.62	0.02	97.37
MH2-15b-10	Core	11.69	6.76	0.05	0.83	1.88	0.03	6.4	0.01	33.02	0.03	0.38	34.7	0.01	95.79
MH2-15b-10	Rim	11.44	10.22	0	0.64	2.24	0.03	6.11	0.02	28.93	0.03	1.3	35.15	0.03	96.12

Table A15

Comment	B2O3	FeO	F	CaO	Na2O	MnO	MgO	K2O	Al2O3	ZnO	TiO2	SiO2	Cr2O3	Total
Line 1 17 Traverse	12.57	7.41	0	1.03	1.98	0.03	7.03	0.02	31.42	0	0.49	34.95	0.06	96.99
Line 2 17 Traverse	12.59	7.48	0.1	1.01	1.93	0.01	6.84	0.01	31.39	0.03	0.48	35	0.05	96.87
Line 3 17 Traverse	12.34	8.05	0.06	0.87	2.01	0.04	6.52	0.02	31.56	0.04	0.5	35.42	0.07	97.46
Line 4 17 Traverse	12.12	8.75	0	0.89	1.91	0.02	5.99	0.02	31.64	0.05	0.57	35.14	0.07	97.18
Line 5 17 Traverse	12.71	8.87	0	0.89	1.82	0.03	5.64	0.02	32.06	0.03	0.52	34.99	0.05	97.63
Line 6 17 Traverse	11.89	8.88	0	0.89	1.85	0.03	5.63	0.02	31.84	0.02	0.5	34.9	0.03	96.48
Line 7 17 Traverse	11.39	8.94	0	0.89	1.89	0.01	5.64	0.03	31.76	0.04	0.49	35.15	0.02	96.25
Line 8 17 Traverse	14.81	13.03	0	0.63	1.83	0.04	5.58	0.05	30.55	0.03	0.44	34.15	0.04	101.17
Line 9 17 Traverse	12.17	9	0	0.65	2.01	0.02	5.66	0.01	31.37	0.04	0.5	35.21	0.01	96.66
Line 10 17 Traverse	12.07	8.6	0.01	0.37	1.84	0	5.47	0.01	31.98	0.02	0.31	35.77	0.02	96.46
Line 11 17 Traverse	12.28	8.1	0.08	0.32	1.85	0.01	5.66	0.01	32.52	0.04	0.12	35.98	0.02	96.96
Line 12 17 Traverse	11.79	8.79	0.02	0.77	1.98	0.01	5.74	0	31.12	0.04	0.5	35.18	0.04	95.97
Line 14 17 Traverse	11.77	8.29	0.05	0.89	1.77	0.01	5.25	0.02	32.05	0.02	0.26	35.64	0.02	96.01
Line 15 17 Traverse	11.94	8.27	0	0.44	1.79	0	5.43	0.01	32.23	0.02	0.26	35.73	0.01	96.14
Line 16 17 Traverse	11.87	8.53	0	0.56	1.86	0.02	5.49	0.01	31.66	0.02	0.35	35.43	0.01	95.81
Line 17 17 Traverse	11.83	8.7	0	0.59	1.9	0.02	5.47	0.01	31.65	0.03	0.43	35.45	0.03	96.11
Line 18 17 Traverse	11.97	8.33	0.01	0.42	1.81	0	5.44	0.01	32.37	0.02	0.24	35.82	0.01	96.44
Line 19 17 Traverse	12.17	8.26	0	0.4	1.92	0.01	5.56	0.01	32.45	0.02	0.17	35.77	0.01	96.76
Line 20 17 Traverse	11.83	8.3	0	0.38	1.91	0	5.57	0.02	32.44	0.02	0.27	35.83	0.02	96.58
Line 21 17 Traverse	12.39	8.63	0.03	0.58	2.03	0.01	5.74	0.01	31.32	0.02	0.4	35.49	0.03	96.66
Line 22 17 Traverse	12.13	8.77	0	0.8	1.86	0.02	5.5	0.01	31.94	0.02	0.46	35.01	0.03	96.54
Line 23 17 Traverse	11.68	8.67	0	0.77	1.79	0.02	5.37	0.03	32.11	0.03	0.43	35.02	0.04	95.94
Line 24 17 Traverse	11.77	8.69	0	0.91	1.82	0.02	5.55	0.01	31.54	0.02	0.44	34.74	0.01	95.54
Line 25 17 Traverse	11.6	8.54	0.08	0.84	1.78	0.02	5.62	0.02	32.1	0.05	0.31	35.23	0	96.14

Comment	B2O3	FeO	F	CaO	Na2O	MnO	MgO	K2O	Al2O3	ZnO	TiO2	SiO2	Cr2O3	Total
Line 26 17 Traverse	11.94	8.79	0.08	0.97	1.89	0.02	5.72	0.02	31.88	0.05	0.4	35.04	0.02	96.78
Line 27 17 Traverse	11.86	8.8	0.06	0.88	1.85	0.01	5.84	0.02	31.43	0	0.45	34.95	0.01	96.13
Line 28 17 Traverse	11.94	7.95	0	0.85	1.92	0.02	6.38	0.02	31.36	0.03	0.43	35.57	0.02	96.48
Line 29 17 Traverse	11.47	7.73	0.07	0.94	1.96	0.02	6.66	0.02	31.36	0.02	0.43	35.2	0.04	95.88
Line 30 17 Traverse	12.62	7.2	0.02	1.06	1.94	0.02	6.95	0.03	31.47	0.04	0.46	35.31	0.05	97.16

Table A16 shows the results of all chlorite WDS analyses in wt %.

Core-Section-Sample	FeO	F	CaO	Na2O	MnO	MgO	K2O	Al2O3	ZnO	TiO2	SiO2	Cr2O3	Total
MH1-03-1	26.14	0.02	0.04	0.05	0.34	12.98	0.01	22.47	0.12	0.07	23.78	0.01	86.02
MH1-03-1	26.72	0.00	0.00	0.05	0.33	12.71	0.02	22.70	0.13	0.07	23.67	0.03	86.42
MH1-03-1	27.00	0.00	0.00	0.02	0.36	13.00	0.02	23.02	0.17	0.09	24.28	0.02	87.98
MH1-03-2	27.30	0.00	0.00	0.02	0.35	13.09	0.02	22.65	0.18	0.06	24.18	0.00	87.85
MH1-03-2	26.94	0.01	0.00	0.01	0.36	13.23	0.02	22.71	0.18	0.06	24.33	0.01	87.87
MH1-03-2	27.04	0.00	0.00	0.02	0.37	13.30	0.02	22.74	0.18	0.05	24.28	0.02	88.01
MH1-03-3	26.60	0.00	0.00	0.05	0.33	13.83	0.02	22.85	0.15	0.03	24.69	0.00	88.55
MH1-03-3	26.34	0.05	0.00	0.02	0.34	13.10	0.03	22.70	0.13	0.03	24.33	0.00	87.06
MH1-03-3	26.89	0.00	0.00	0.03	0.37	12.91	0.02	22.16	0.15	0.06	23.40	0.01	86.01
MH1-03-3	26.88	0.01	0.00	0.04	0.36	13.47	0.00	22.36	0.12	0.07	23.81	0.01	87.13
MH1-03-4	26.29	0.00	0.00	0.02	0.33	13.70	0.02	23.02	0.18	0.04	24.50	0.01	88.11
MH1-03-4	26.65	0.05	0.00	0.02	0.33	13.41	0.03	22.66	0.20	0.07	24.23	0.00	87.66
MH1-03-4	26.14	0.05	0.00	0.03	0.30	13.44	0.03	22.46	0.16	0.06	24.20	0.01	86.88
MH1-03-4	25.78	0.03	0.00	0.04	0.32	13.63	0.03	22.67	0.18	0.06	24.25	0.01	87.00
MH1-03-4	25.92	0.03	0.00	0.02	0.32	14.09	0.02	23.05	0.17	0.05	24.59	0.01	88.26
MH1-03-5	26.32	0.00	0.00	0.04	0.32	12.55	0.00	21.96	0.12	0.05	23.49	0.03	84.88
MH1-03-5	27.61	0.00	0.00	0.05	0.33	13.26	0.01	22.76	0.17	0.06	23.77	0.03	88.04
MH1-03-5	26.72	0.05	0.01	0.05	0.29	13.00	0.02	22.99	0.17	0.05	24.25	0.02	87.63
MH1-03-5	27.20	0.00	0.00	0.04	0.33	13.25	0.01	23.32	0.15	0.06	24.73	0.00	89.09
MH1-03-5	26.99	0.01	0.00	0.04	0.32	12.96	0.01	22.68	0.13	0.05	23.79	0.00	86.98
MH1-03-5	27.14	0.01	0.00	0.04	0.34	13.31	0.01	22.94	0.16	0.07	24.12	0.01	88.16
MH1-19-1	23.61	0.00	0.03	0.04	0.28	15.69	0.02	23.19	0.11	0.05	25.74	0.00	88.77
MH1-19-1	23.29	0.01	0.01	0.02	0.27	16.45	0.13	22.25	0.13	0.05	24.92	0.02	87.53
MH1-19-1	23.03	0.00	0.03	0.06	0.28	14.82	0.22	21.74	0.10	0.04	24.48	0.00	84.81
MH1-19-2	24.41	0.00	0.01	0.02	0.26	14.58	0.05	22.70	0.10	0.06	23.73	0.02	85.93
MH1-19-2	24.36	0.07	0.00	0.02	0.26	15.19	0.03	22.54	0.10	0.05	24.39	0.01	87.03
MH1-19-2	23.97	0.00	0.00	0.01	0.31	15.50	0.04	21.91	0.12	0.09	24.21	0.02	86.17
MH1-19-3	23.94	0.01	0.00	0.07	0.31	15.60	0.03	23.14	0.10	0.07	25.57	0.02	88.86

Core-Section-Sample	FeO	F	CaO	Na2O	MnO	MgO	K2O	Al2O3	ZnO	TiO2	SiO2	Cr2O3	Total
MH1-19-3	24.24	0.01	0.00	0.05	0.29	14.88	0.03	22.32	0.13	0.05	24.87	0.02	86.88
MH1-19-3	24.80	0.00	0.00	0.04	0.29	15.43	0.01	23.02	0.10	0.07	24.75	0.01	88.54
MH1-19-3	24.48	0.00	0.00	0.06	0.29	15.71	0.03	23.64	0.12	0.07	25.23	0.02	89.66
MH1-19-3	23.88	0.00	0.00	0.06	0.28	15.08	0.26	23.10	0.09	0.06	25.46	0.01	88.28
MH1-19-4	24.17	0.00	0.01	0.04	0.29	16.06	0.04	23.04	0.12	0.07	25.66	0.01	89.51
MH1-19-4	23.89	0.01	0.00	0.02	0.29	15.52	0.10	22.13	0.12	0.08	25.16	0.01	87.32
MH1-19-4	23.91	0.05	0.00	0.02	0.30	15.44	0.05	21.47	0.12	0.05	24.06	0.02	85.49
MH1-19-4	23.48	0.02	0.01	0.04	0.24	14.78	0.02	22.71	0.14	0.05	25.96	0.00	87.45
MH1-19-4	6.19	0.07	0.07	0.58	0.03	2.24	8.67	30.84	0.00	0.38	44.02	0.00	93.09
MH1-19-5	23.88	0.03	0.00	0.49	0.28	14.51	0.07	22.21	0.10	0.08	24.00	0.01	85.66
MH1-19-5	23.54	0.02	0.01	0.44	0.28	15.20	0.06	23.21	0.13	0.04	26.09	0.00	89.03
MH1-19-5	24.24	0.00	0.00	0.25	0.27	15.33	0.06	23.01	0.12	0.07	24.66	0.01	88.03
MH1-19-5	24.00	0.00	0.00	0.31	0.29	15.32	0.10	22.78	0.10	0.05	24.79	0.00	87.75
MH1-19-5	24.16	0.00	0.00	0.18	0.29	15.55	0.05	22.91	0.11	0.07	25.08	0.02	88.41
MH1-19-6	23.92	0.01	0.00	0.06	0.28	14.30	0.10	23.03	0.12	0.08	25.13	0.00	87.03
MH1-19-6	23.91	0.00	0.01	0.06	0.29	14.61	0.04	22.35	0.12	0.08	24.56	0.00	86.03
MH1-19-6	24.22	0.00	0.01	0.04	0.29	14.69	0.06	22.60	0.12	0.05	25.07	0.00	87.16
MH1-19-7	24.92	0.03	0.01	0.05	0.26	15.97	0.03	22.66	0.13	0.04	25.65	0.01	89.77
MH1-19-7	24.34	0.01	0.01	0.00	0.28	15.58	0.04	21.76	0.12	0.05	23.84	0.01	86.03
MH1-19-7	24.47	0.00	0.00	0.03	0.29	15.47	0.02	22.49	0.09	0.08	24.57	0.02	87.53
MH1-19-7	24.15	0.00	0.00	0.03	0.28	15.84	0.03	22.36	0.10	0.06	24.49	0.02	87.36
MH1-19-7	24.31	0.00	0.00	0.03	0.24	15.81	0.04	22.90	0.13	0.05	25.44	0.00	88.94
MH1-14-1	22.54	0.00	0.01	0.10	0.42	16.97	0.01	22.24	0.10	0.06	25.32	0.01	87.76
MH1-14-1	22.28	0.01	0.01	0.16	0.39	15.99	0.06	21.78	0.13	0.07	24.96	0.00	85.83
MH1-14-1	22.55	0.03	0.00	0.05	0.44	16.27	0.01	21.69	0.12	0.06	24.80	0.01	86.03
MH1-14-1	22.29	0.00	0.00	0.06	0.41	16.81	0.01	22.20	0.12	0.05	25.59	0.01	87.55
MH1-14-2	22.29	0.04	0.00	0.02	0.42	17.50	0.02	22.12	0.11	0.07	25.85	0.01	88.46
MH1-14-2	22.16	0.00	0.00	0.05	0.43	17.38	0.04	21.60	0.11	0.09	25.27	0.01	87.14
MH1-14-2	22.21	0.00	0.00	0.04	0.42	17.47	0.03	22.18	0.10	0.08	25.94	0.00	88.47

Core-Section-Sample	FeO	F	CaO	Na2O	MnO	MgO	K2O	Al2O3	ZnO	TiO2	SiO2	Cr2O3	Total
MH1-14-2	22.15	0.02	0.00	0.05	0.42	17.32	0.03	22.14	0.12	0.05	26.18	0.00	88.48
MH1-14-2	22.14	0.02	0.00	0.03	0.40	17.10	0.14	21.99	0.12	0.06	26.06	0.00	88.08
MH1-14-3	22.35	0.00	0.07	0.06	0.45	15.96	0.07	20.77	0.11	0.06	24.35	0.01	84.25
MH1-14-3	21.73	0.00	0.02	0.12	0.38	16.99	0.12	21.68	0.12	0.09	25.40	0.00	86.64
MH1-14-3	21.83	0.00	0.00	0.10	0.45	16.79	0.04	21.57	0.10	0.05	24.99	0.00	85.91
MH1-14-3	21.47	0.00	0.04	0.08	0.38	17.11	0.06	21.48	0.10	0.04	24.97	0.00	85.73
MH1-14-3	22.17	0.01	0.00	0.09	0.46	16.15	0.02	21.18	0.08	0.05	24.22	0.03	84.45
MH1-14-4	22.44	0.04	0.07	0.10	0.41	17.42	0.05	22.21	0.11	0.08	25.51	0.01	88.46
MH1-14-3	22.69	0.00	0.04	0.08	0.43	16.86	0.03	22.37	0.12	0.05	25.17	0.00	87.85
MH1-14-4	22.28	0.01	0.04	0.10	0.40	16.75	0.05	21.98	0.08	0.08	24.68	0.00	86.43
MH1-14-4	22.08	0.00	0.06	0.11	0.40	16.66	0.04	22.22	0.11	0.08	24.72	0.00	86.48
MH1-14-4	22.03	0.00	0.12	0.04	0.42	16.13	0.03	22.06	0.10	0.08	24.85	0.01	85.87
MH1-14-4	22.20	0.00	0.15	0.06	0.37	17.04	0.04	22.47	0.07	0.06	25.08	0.00	87.53
MH1-14-5	22.00	0.03	0.01	0.07	0.40	16.14	0.03	21.84	0.12	0.05	24.80	0.00	85.49
MH1-14-5	22.78	0.00	0.02	0.05	0.44	16.03	0.03	22.24	0.11	0.07	24.53	0.02	86.33
MH1-14-5	21.67	0.14	0.00	0.09	0.42	16.81	0.03	21.58	0.09	0.08	24.83	0.01	85.76
MH1-14-5	22.08	0.00	0.13	0.03	0.39	16.42	0.03	22.10	0.11	0.04	25.13	0.00	86.47
MH1-14-6	21.11	0.03	0.03	0.15	0.40	16.49	0.04	21.34	0.12	0.05	24.32	0.01	84.09
MH1-14-6	21.60	0.03	0.00	0.13	0.42	16.61	0.03	22.27	0.08	0.04	25.16	0.00	86.37
MH1-14-6	21.30	0.04	0.01	0.12	0.41	16.89	0.03	22.39	0.10	0.07	25.24	0.01	86.63
MH1-14-6	20.93	0.00	0.00	0.10	0.41	17.13	0.08	21.04	0.10	0.07	24.10	0.03	84.01
MH1-13-1	26.07	0.01	0.02	0.14	0.34	14.72	0.03	23.01	0.12	0.05	25.29	0.00	89.80
MH1-13-1	26.23	0.00	0.02	0.14	0.35	13.83	0.03	22.59	0.10	0.05	24.66	0.01	88.00
MH1-13-1	26.65	0.04	0.01	0.11	0.39	13.71	0.03	22.35	0.10	0.07	24.30	0.01	87.78
MH1-13-1	26.36	0.00	0.00	0.14	0.39	14.00	0.02	23.04	0.13	0.08	25.01	0.01	89.17
MH1-13-3	26.57	0.00	0.00	0.11	0.40	13.92	0.05	23.14	0.13	0.07	24.68	0.01	89.07
MH1-13-3	26.59	0.06	0.00	0.11	0.38	14.14	0.05	23.38	0.11	0.06	24.61	0.02	89.51
MH1-13-3	26.26	0.05	0.00	0.11	0.37	14.28	0.09	22.79	0.08	0.07	24.87	0.02	88.97
MH1-13-3	26.36	0.03	0.00	0.10	0.39	14.18	0.04	23.22	0.12	0.06	24.61	0.02	89.12

Core-Section-Sample	FeO	F	CaO	Na2O	MnO	MgO	K2O	Al2O3	ZnO	TiO2	SiO2	Cr2O3	Total
MH1-13-4	26.72	0.08	0.00	0.11	0.35	14.32	0.03	22.94	0.11	0.05	25.01	0.00	89.73
MH1-13-4	26.33	0.07	0.00	0.15	0.35	14.22	0.02	23.08	0.10	0.03	24.99	0.00	89.34
MH1-13-4	26.03	0.00	0.00	0.12	0.37	14.45	0.03	23.04	0.09	0.05	24.91	0.02	89.11
MH1-13-4	25.92	0.06	0.00	0.11	0.36	14.62	0.02	23.24	0.14	0.06	25.02	0.01	89.56
MH1-13-5	23.48	0.00	0.54	0.33	0.32	15.07	0.09	22.78	0.10	0.06	25.36	0.00	88.11
MH1-13-5	24.84	0.03	0.26	0.29	0.35	14.88	0.07	22.99	0.11	0.05	25.29	0.02	89.18
MH1-13-5	25.59	0.07	0.22	0.26	0.38	14.75	0.07	22.71	0.12	0.05	24.62	0.02	88.86
MH1-13-5	25.26	0.02	0.20	0.25	0.35	14.58	0.07	22.45	0.13	0.05	24.52	0.01	87.88
MH1-13-6	25.81	0.07	0.00	0.14	0.39	14.25	0.01	22.17	0.11	0.06	23.71	0.02	86.74
MH1-13-6	25.95	0.00	0.00	0.11	0.36	14.64	0.02	22.93	0.11	0.04	24.51	0.02	88.70
MH1-13-6	25.91	0.00	0.00	0.08	0.38	14.40	0.01	23.09	0.10	0.04	24.40	0.01	88.43
MH1-13-6	25.94	0.01	0.00	0.13	0.42	14.18	0.02	23.11	0.13	0.07	24.75	0.01	88.78
MH1-07-2	18.15	0.17	0.00	0.03	0.32	19.77	0.00	23.07	0.07	0.07	26.08	0.02	87.75
MH1-07-4	21.07	0.14	0.00	0.03	0.46	17.25	0.01	22.93	0.11	0.06	24.82	0.02	86.90
MH1-07-4	20.78	0.07	0.00	0.02	0.41	16.51	0.00	22.24	0.05	0.03	24.35	0.01	84.48
MH1-07-4	20.84	0.05	0.01	0.03	0.44	16.63	0.01	22.97	0.07	0.08	24.82	0.04	85.99
MH1-07-4	20.57	0.13	0.06	0.02	0.43	17.36	0.01	23.48	0.08	0.08	25.39	0.00	87.61
MH1-07-5	20.58	0.05	0.03	0.06	0.45	17.05	0.02	22.80	0.06	0.10	25.13	0.01	86.34
MH1-07-5	20.39	0.03	0.02	0.07	0.39	16.62	0.01	22.74	0.07	0.04	24.61	0.00	84.98
MH1-07-6	19.56	0.15	0.02	0.05	0.40	16.67	0.02	22.66	0.09	0.03	24.67	0.00	84.31
MH1-07-6	19.18	0.10	0.02	0.06	0.39	17.16	0.02	22.57	0.08	0.04	24.42	0.00	84.02
MH1-43-1	19.85	0.05	0.05	0.03	0.49	17.04	0.04	22.76	0.14	0.05	24.64	0.01	85.16
MH1-43-1	19.25	0.03	0.08	0.01	0.49	18.39	0.01	22.35	0.09	0.06	25.66	0.01	86.43
MH1-43-1	19.24	0.02	0.09	0.03	0.45	17.98	0.20	21.91	0.13	0.09	25.64	0.02	85.79
MH1-43-1	19.52	0.00	0.19	0.02	0.50	17.40	0.02	21.62	0.15	0.05	25.80	0.01	85.28
MH1-43-1	20.01	0.00	0.02	0.03	0.54	18.02	0.02	22.62	0.13	0.06	25.45	0.00	86.89
MH1-43-2	19.35	0.01	0.05	0.00	0.55	18.31	0.01	22.65	0.10	0.05	25.18	0.01	86.27
MH1-43-2	19.31	0.06	0.08	0.02	0.55	17.96	0.01	22.43	0.13	0.04	25.75	0.00	86.35
MH1-43-2	19.45	0.00	0.03	0.01	0.56	17.56	0.02	22.12	0.13	0.07	25.31	0.00	85.27

Core-Section-Sample	FeO	F	CaO	Na2O	MnO	MgO	K2O	Al2O3	ZnO	TiO2	SiO2	Cr2O3	Total
MH1-43-2	19.80	0.04	0.08	0.02	0.56	17.45	0.01	21.73	0.15	0.06	24.75	0.03	84.66
MH1-43-2	19.91	0.02	0.06	0.01	0.54	17.48	0.01	22.24	0.11	0.06	25.36	0.02	85.83
MH1-43-3	19.40	0.04	0.04	0.01	0.52	18.56	0.01	21.85	0.10	0.06	25.70	0.00	86.30
MH1-43-3	19.49	0.03	0.03	0.03	0.50	17.71	0.02	21.76	0.10	0.06	25.67	0.00	85.40
MH1-43-3	19.25	0.06	0.08	0.01	0.48	18.76	0.01	21.54	0.13	0.05	25.73	0.03	86.14
MH1-43-3	20.10	0.08	0.01	0.00	0.53	18.47	0.00	22.43	0.13	0.04	25.94	0.01	87.74
MH1-43-3	19.93	0.06	0.00	0.00	0.50	18.45	0.00	22.38	0.12	0.07	25.62	0.00	87.13
MH1-43-4	17.64	0.09	0.01	0.04	0.37	16.79	0.02	19.63	0.08	0.02	32.11	0.00	86.81
MH1-43-4	19.24	0.00	0.00	0.00	0.41	18.48	0.03	22.09	0.08	0.07	25.57	0.02	85.98
MH1-43-4	19.05	0.00	0.00	0.01	0.39	18.58	0.17	22.56	0.11	0.07	26.10	0.01	87.05
MH1-43-4	19.44	0.00	0.01	0.04	0.39	18.84	0.02	22.94	0.12	0.04	26.53	0.01	88.39
MH1-43-5	19.84	0.10	0.02	0.06	0.45	17.84	0.02	21.82	0.11	0.05	25.87	0.00	86.19
MH1-43-5	20.04	0.00	0.01	0.04	0.50	18.19	0.02	22.98	0.09	0.07	25.79	0.01	87.73
MH1-43-5	19.76	0.00	0.00	0.02	0.48	18.18	0.01	22.69	0.08	0.07	25.58	0.01	86.89
MH1-43-5	19.60	0.00	0.03	0.06	0.47	18.41	0.02	22.84	0.12	0.05	25.87	0.02	87.49
MH1-43-5	19.29	0.09	0.02	0.03	0.48	18.57	0.01	22.55	0.10	0.03	25.89	0.01	87.05
MH2-25-4	24.90		0.02	0.02	0.43	14.78	0.02	22.50		0.06	25.41		88.14
MH2-25-4	24.93		0.00	0.05	0.43	14.50	0.06	22.33		0.05	25.74		88.09
MH2-25-4	24.42		0.08	0.01	0.40	14.48	0.08	21.98		0.06	26.77		88.28
MH2-25-4	24.96		0.00	0.02	0.43	14.78	0.03	22.02		0.06	25.36		87.66
MH2-25-4	24.58		0.04	0.06	0.43	13.63	0.70	23.18		0.09	27.19		89.88
MH2-25-5	24.89		0.00	0.03	0.39	14.67	0.10	21.68		0.09	25.84		87.68
MH2-25-5	24.70		0.02	0.07	0.46	15.28	0.03	22.13		0.05	25.65		88.40
MH2-25-5	24.76		0.01	0.05	0.44	14.73	0.32	21.84		0.13	26.36		88.63
MH2-25-5	23.88		0.03	0.04	0.37	13.64	1.64	20.11		0.58	27.99		88.28
MH2-25-5	24.90		0.02	0.05	0.45	14.88	0.01	22.19		0.00	25.41		87.92
MH2-32-1	9.97		0.00	0.04	0.21	26.29	0.05	18.51		0.04	29.56		84.67
MH2-32-1	10.10		0.01	0.03	0.18	26.52	0.05	17.63		0.01	30.35		84.89
MH2-32-1	10.29		0.02	0.05	0.17	25.63	0.03	18.41		0.03	29.57		84.21

Core-Section-Sample	FeO	F	CaO	Na2O	MnO	MgO	K2O	Al2O3	ZnO	TiO2	SiO2	Cr2O3	Total
MH2-32-1	10.44		0.03	0.03	0.16	26.01	0.04	18.28		0.03	29.93		84.94
MH2-32-1	10.51		0.05	0.07	0.19	25.49	0.06	18.42		0.02	29.32		84.13
MH2-32-2	10.41		0.00	0.07	0.21	25.79	0.06	18.56		0.02	29.71		84.83
MH2-32-2	9.69		0.01	0.07	0.22	26.97	0.07	16.78		0.00	31.07		84.87
MH2-32-2	10.27		0.01	0.08	0.19	26.43	0.04	18.06		0.02	30.01		85.13
MH2-32-2	10.58		0.07	0.10	0.21	26.12	0.07	18.14		0.02	29.90		85.20
MH2-32-4	9.79		0.04	0.09	0.18	27.18	0.06	17.27		0.04	31.11		85.76
MH2-32-4	9.68		0.01	0.05	0.19	25.90	0.04	16.39		0.04	33.20		85.51
MH2-32-4	9.76		0.00	0.05	0.15	25.25	0.09	17.28		0.03	31.87		84.50
MH2-32-4	10.43		0.02	0.06	0.18	26.44	0.06	18.59		0.06	29.44		85.28
MH2-32-4	10.20		0.00	0.05	0.17	26.13	0.04	18.26		0.02	29.57		84.46
MH2-15a-1	23.25		0.00	0.07	0.16	15.22	0.03	24.27		0.07	24.40		87.47
MH2-15a-1	23.31		0.00	0.07	0.15	15.11	0.04	24.14		0.03	24.32		87.18
MH2-15a-1	23.20		0.01	0.04	0.18	15.71	0.04	23.51		0.04	25.17		87.89
MH2-15a-1	22.89		0.00	0.04	0.18	15.09	0.03	24.10		0.01	24.54		86.87
MH2-15a-2	22.71		0.00	0.02	0.21	15.56	0.05	22.72		0.05	25.12		86.45
MH2-15a-2	22.75		0.02	0.05	0.17	15.67	0.05	23.26		0.04	25.19		87.21
MH2-15a-2	22.72		0.07	0.07	0.15	15.39	0.06	23.20		0.03	24.99		86.67
MH2-15a-2	22.45		0.01	0.04	0.17	15.78	0.01	23.35		0.06	25.29		87.15
MH2-15a-3	22.49		0.01	0.06	0.20	15.62	0.10	23.48		0.03	25.23		87.22
MH2-15a-3	22.58		0.00	0.05	0.16	15.67	0.16	23.14		0.07	25.50		87.33
MH2-15a-3	23.07		0.04	0.06	0.17	15.10	0.03	23.61		0.04	24.65		86.77
MH2-15a-3	22.84		0.00	0.06	0.18	15.81	0.06	23.08		0.03	25.44		87.49
MH2-15a-4	23.66		0.00	0.08	0.16	14.79	0.06	23.09		0.05	24.81		86.70
MH2-15a-4	23.39		0.01	0.07	0.18	15.28	0.04	23.51		0.01	24.85		87.36
MH2-15a-4	23.09		0.00	0.05	0.18	15.41	0.03	23.47		0.00	25.11		87.33
MH2-15a-4	23.10		0.00	0.10	0.17	15.42	0.08	23.38		0.08	24.80		87.14
MH2-15a-4	23.11		0.09	0.04	0.18	15.39	0.10	23.27		0.01	25.03		87.23
MH2-15a-5	23.65		0.00	0.04	0.18	14.76	0.00	24.09		0.00	24.69		87.41

Core-Section-Sample	FeO	F	CaO	Na2O	MnO	MgO	K2O	Al2O3	ZnO	TiO2	SiO2	Cr2O3	Total
MH2-15a-5	22.92		0.00	0.06	0.20	15.44	0.04	23.58		0.05	25.29		87.57
MH2-15a-5	23.26		0.00	0.06	0.20	14.99	0.04	23.95		0.05	24.96		87.52
MH2-15a-5	22.77		0.00	0.04	0.19	15.20	0.04	24.11		0.04	24.87		87.26
MH2-15a-6	23.29		0.00	0.05	0.18	15.47	0.03	23.46		0.04	25.00		87.53
MH2-15a-6	22.79		0.01	0.06	0.18	15.80	0.03	23.38		0.04	25.50		87.77
MH2-15a-6	21.72		0.00	0.03	0.17	15.83	0.02	23.27		0.02	25.34		86.40
MH2-15a-6	23.09		0.03	0.07	0.17	15.46	0.03	23.31		0.04	24.82		87.02
MH2-15a-6	22.78		0.03	0.05	0.18	15.45	0.04	23.18		0.00	25.04		86.76
MH2-15a-7	22.95		0.04	0.08	0.18	15.15	0.05	23.34		0.04	24.79		86.63
MH2-15a-7	23.66		0.00	0.06	0.20	15.10	0.02	23.82		0.06	24.75		87.68
MH2-15a-7	23.50		0.02	0.12	0.21	14.47	0.04	23.34		0.02	24.31		86.04
MH2-15a-7	23.75		0.00	0.06	0.18	15.00	0.02	23.78		0.01	24.79		87.58
MH2-43-1	24.20		0.09	0.13	0.24	14.24	0.07	20.83		0.03	24.67		84.50
MH2-43-1	24.17		0.08	0.12	0.28	13.93	0.09	21.29		0.05	24.89		84.90
MH2-43-1	24.65		0.09	0.14	0.27	14.61	0.09	22.24		0.04	25.91		88.05
MH2-43-1	24.42		0.08	0.13	0.28	14.43	0.08	22.25		0.06	25.19		86.94
MH2-43-2	24.86		0.03	0.08	0.28	15.24	0.05	21.60		0.06	25.46		87.65
MH2-43-2	24.42		0.04	0.11	0.29	14.77	0.08	21.68		0.02	25.20		86.62
MH2-43-2	24.81		0.01	0.06	0.28	15.14	0.03	21.74		0.02	25.55		87.64
MH2-43-3	24.48		0.00	0.02	0.32	14.73	0.02	21.31		0.06	25.22		86.17
MH2-43-3	24.31		0.00	0.01	0.27	14.48	0.08	21.79		0.05	25.54		86.53
MH2-43-3	24.67		0.00	0.00	0.26	15.15	0.04	21.10		0.05	25.10		86.36
MH2-43-3	24.26		0.01	0.03	0.26	14.81	0.03	21.32		0.08	25.11		85.92
MH2-43-4	25.31		0.01	0.06	0.30	14.61	0.07	22.04		0.11	25.42		87.92
MH2-43-4	24.97		0.01	0.06	0.30	14.90	0.07	22.31		0.15	25.41		88.18
MH2-43-4	24.96		0.02	0.07	0.29	14.82	0.07	21.82		0.07	24.92		87.04
MH2-43-4	25.29		0.00	0.04	0.30	14.98	0.03	22.35		0.06	25.33		88.38
MH2-43-5	24.74		0.02	0.03	0.30	14.79	0.03	22.22		0.04	25.27		87.44
MH2-43-5	24.44		0.01	0.05	0.33	14.96	0.05	21.46		0.01	24.91		86.23

Core-Section-Sample	FeO	F	CaO	Na2O	MnO	MgO	K2O	Al2O3	ZnO	TiO2	SiO2	Cr2O3	Total
MH2-43-5	24.54		0.00	0.05	0.26	14.79	0.02	21.99		0.05	25.49		87.19
MH2-43-5	24.46		0.00	0.03	0.33	14.35	0.04	22.46		0.07	25.64		87.37
MH2-43-6	24.76		0.03	0.11	0.29	15.04	0.04	22.24		0.08	25.36		87.95
MH2-43-6	24.63		0.00	0.10	0.28	15.12	0.05	22.23		0.07	25.50		87.99
MH2-43-6	24.71		0.00	0.13	0.31	14.92	0.04	21.52		0.06	24.97		86.67
MH2-43-6	24.76		0.01	0.11	0.28	15.06	0.03	21.95		0.02	25.38		87.61
MH2-43-7	24.45		0.00	0.01	0.30	14.47	0.82	21.14		0.18	25.78		87.15
MH2-43-7	24.49		0.00	0.02	0.30	15.14	0.04	21.99		0.05	25.18		87.21
MH2-43-7	24.50		0.00	0.05	0.33	15.17	0.28	22.15		0.10	25.82		88.38
MH2-43-7	24.50		0.00	0.02	0.33	15.18	0.04	22.17		0.06	25.68		87.97
MH2-43-7	24.48		0.00	0.03	0.30	14.97	0.00	21.71		0.05	25.36		86.89
MH2-43-7	24.48		0.00	0.02	0.29	14.87	0.14	21.69		0.08	25.96		87.52
MH2-04-1	12.06		0.02	0.06	0.27	24.66	0.02	19.14		0.02	29.56		85.81
MH2-04-1	11.73		0.00	0.05	0.26	25.19	0.01	18.45		0.04	29.99		85.71
MH2-04-2	11.63		0.03	0.07	0.26	24.88	0.03	18.68		0.01	30.00		85.58
MH2-04-2	11.78		0.03	0.08	0.28	24.87	0.03	19.18		0.01	29.72		85.99
MH2-04-2	11.52		0.06	0.13	0.27	24.21	0.03	18.96		0.01	29.30		84.51
MH2-04-3	11.87		0.07	0.03	0.27	24.28	0.02	19.04		0.02	29.64		85.24
MH2-04-3	11.85		0.14	0.14	0.26	24.75	0.03	18.67		0.04	29.52		85.41
MH2-04-3	11.89		0.12	0.14	0.29	24.11	0.05	19.00		0.00	28.84		84.43
MH2-04-4	11.96		0.11	0.14	0.23	24.49	0.06	18.92		0.02	29.72		85.63
MH2-04-4	11.64		0.06	0.14	0.26	24.89	0.06	18.71		0.01	29.80		85.57
MH2-04-5	11.71		0.11	0.18	0.28	24.29	0.04	18.77		0.09	29.75		85.22
MH2-04-5	11.38		0.03	0.13	0.28	25.12	0.05	18.37		0.24	30.12		85.72
MH2-04-5	11.13		0.02	0.15	0.25	25.86	0.04	17.34		0.13	30.69		85.63
MH2-04-5	11.47		0.07	0.02	0.25	25.14	0.03	19.08		0.09	29.60		85.74
MH2-04-6	9.81		0.00	0.03	0.21	27.05	0.03	15.86		0.00	31.83		84.81
MH2-04-6	10.20		0.01	0.04	0.22	26.35	0.01	15.70		0.01	31.48		84.02
MH2-04-7	11.20		0.06	0.14	0.27	25.15	0.06	18.77		0.03	29.44		85.13

Core-Section-Sample	FeO	F	CaO	Na2O	MnO	MgO	K2O	Al2O3	ZnO	TiO2	SiO2	Cr2O3	Total
MH2-04-7	11.19		0.04	0.13	0.22	24.88	0.06	19.11		0.04	29.44		85.12
MH2-04-7	11.27		0.05	0.09	0.34	24.43	0.04	18.82		0.02	29.60		84.67
MH2-04-7	11.42		0.05	0.07	0.29	24.68	0.06	18.48		0.04	29.30		84.39
MH1-15b-3	22.25		0.03	0.03	0.19	14.25	0.02	23.08		0.03	25.42		85.29
MH1-15b-4	23.39		0.45	0.05	0.19	13.79	0.04	23.28		0.00	24.18		85.37
MH1-15b-4	23.48		0.45	0.05	0.18	13.73	0.06	23.42		0.04	24.26		85.68
MH1-15b-8	22.29		0.05	0.02	0.18	14.33	0.14	24.61		0.00	24.79		86.41
MH2-17-1	22.53		0.00	0.00	0.20	15.56	0.04	23.59		0.04	24.96		86.92
MH2-17-1	22.22		0.00	0.02	0.18	15.32	0.04	23.90		0.03	25.36		87.07
MH2-17-1	22.10		0.01	0.01	0.19	15.10	0.05	23.07		0.06	24.77		85.36
MH2-17-1	22.33		0.00	0.01	0.22	15.28	0.02	23.16		0.06	24.80		85.89
MH2-17-1	22.37		0.00	0.03	0.19	15.09	0.02	23.23		0.03	24.62		85.58
MH2-17-2	22.34		0.00	0.03	0.23	16.01	0.03	24.09		0.04	25.20		87.97
MH2-17-2	21.93		0.00	0.02	0.23	15.71	0.05	23.51		0.09	24.96		86.49
MH2-17-2	22.38		0.00	0.03	0.25	15.21	0.02	23.01		0.05	24.41		85.35
MH2-17-2	21.81		0.00	0.01	0.23	15.67	0.03	23.22		0.05	24.98		85.99
MH2-17-3	22.47		0.00	0.04	0.27	15.67	0.04	23.74		0.04	24.87		87.12
MH2-17-3	22.05		0.00	0.04	0.20	15.80	0.04	23.56		0.02	24.80		86.52
MH2-17-3	22.48		0.00	0.05	0.21	15.50	0.05	23.37		0.06	25.00		86.72
MH2-17-3	22.56		0.00	0.00	0.22	15.70	0.02	23.34		0.14	24.97		86.94
MH2-17-4	22.71		0.00	0.05	0.21	15.43	0.05	23.47		0.03	25.15		87.09
MH2-17-4	22.62		0.00	0.06	0.19	15.44	0.05	23.88		0.02	25.02		87.28
MH2-17-4	22.49		0.00	0.10	0.20	15.64	0.02	23.43		0.08	24.88		86.84
MH2-17-4	22.76		0.00	0.09	0.17	15.52	0.03	23.64		0.02	24.73		86.95
MH2-17-5	22.58		0.00	0.02	0.21	15.58	0.04	23.56		0.03	25.00		87.02
MH2-17-5	22.83		0.00	0.03	0.16	15.59	0.01	23.64		0.01	25.03		87.30
MH2-17-5	22.60		0.00	0.08	0.20	15.58	0.04	23.68		0.04	25.07		87.29
MH2-17-5	22.65		0.00	0.05	0.21	15.72	0.03	23.99		0.04	25.07		87.77
MH2-17-6	22.88		0.00	0.06	0.20	15.64	0.03	23.94		0.04	25.09		87.89

Core-Section-Sample	FeO	F	CaO	Na2O	MnO	MgO	K2O	Al2O3	ZnO	TiO2	SiO2	Cr2O3	Total
MH2-17-6	22.70		0.00	0.05	0.18	15.44	0.05	23.51		0.06	25.09		87.08
MH2-17-7	22.67		0.00	0.00	0.21	15.69	0.02	23.52		0.04	24.74		86.89
MH2-17-7	22.70		0.00	0.00	0.24	15.54	0.04	23.64		0.02	24.94		87.12
MH2-17-7	22.49		0.00	0.04	0.16	15.61	0.03	23.69		0.08	25.13		87.23
MH2-17-7	22.35		0.00	0.01	0.22	15.78	0.03	23.82		0.05	25.05		87.31
MH2-17-7	22.67		0.00	0.02	0.23	15.75	0.03	23.79		0.04	24.85		87.39
MH2-17-7	22.68		0.00	0.03	0.21	15.76	0.05	23.18		0.06	24.95		86.92
MH2-17-8	22.52		0.00	0.01	0.22	15.73	0.03	23.29		0.07	25.06		86.93
MH2-17-8	22.85		0.00	0.04	0.21	15.63	0.05	23.34		0.02	25.00		87.13
MH2-17-8	22.53		0.01	0.02	0.20	15.72	0.02	23.62		0.02	25.02		87.16
MH2-17-9	22.03		0.00	0.08	0.25	15.88	0.07	23.26		0.00	25.05		86.62
MH2-17-9	22.29		0.00	0.05	0.20	15.87	0.05	23.36		0.06	25.02		86.90
MH2-17-9	22.12		0.00	0.04	0.21	16.06	0.04	23.06		0.04	25.07		86.65
MH2-17-9	22.30		0.00	0.08	0.20	15.67	0.07	23.18		0.06	25.24		86.80
MH2-17-9	22.45		0.00	0.02	0.21	15.53	0.03	23.41		0.07	25.07		86.80
MH1-24-1	5.25		0.00	0.00	0.13	34.39	0.02	3.75		0.00	40.84		84.38
MH1-24-2	5.20		0.00	0.01	0.10	34.25	0.02	4.26		0.02	41.02		84.89
MH1-24-2	5.34		0.02	0.00	0.08	33.95	0.03	4.36		0.01	40.47		84.25
MH1-24-2	5.24		0.03	0.00	0.09	34.40	0.02	5.20		0.00	41.08		86.06
MH1-24-2	5.40		0.01	0.00	0.10	33.87	0.00	4.32		0.00	40.65		84.35
MH1-24-2	5.35		0.02	0.01	0.13	34.02	0.03	4.38		0.02	40.36		84.31
MH1-24-3	5.26		0.01	0.01	0.09	34.09	0.02	4.14		0.02	40.74		84.38
MH1-24-3	5.34		0.01	0.00	0.11	34.20	0.01	4.02		0.03	40.72		84.45
MH1-24-3	5.50		0.00	0.01	0.12	33.98	0.03	3.99		0.03	40.74		84.40
MH1-24-3	5.42		0.01	0.00	0.09	34.01	0.03	4.12		0.00	40.96		84.65
MH1-24-4	5.08		0.01	0.00	0.10	34.63	0.03	4.27		0.00	40.53		84.63
MH1-24-4	5.46		0.01	0.01	0.10	33.91	0.00	4.15		0.00	40.71		84.36
MH1-24-4	5.03		0.00	0.02	0.10	33.93	0.02	4.26		0.00	41.05		84.42
MH1-24-4	5.21		0.01	0.01	0.12	34.01	0.03	4.30		0.00	40.81		84.50

Core-Section-Sample	FeO	F	CaO	Na2O	MnO	MgO	K2O	Al2O3	ZnO	TiO2	SiO2	Cr2O3	Total
MH1-24-4	5.16		0.03	0.00	0.09	34.02	0.03	4.11		0.00	41.16		84.61
MH1-24-5	4.57		0.00	0.00	0.05	31.39	0.02	14.62		0.02	33.44		84.12
MH1-24-5	4.92		0.02	0.02	0.04	31.78	0.01	14.88		0.02	33.03		84.72
MH1-24-5	4.68		0.01	0.01	0.03	31.10	0.01	15.13		0.00	33.36		84.33
MH1-24-6	4.77		0.01	0.00	0.04	31.48	0.02	14.68		0.03	33.21		84.23

Table A17 displays all monazite WDS analyses in wt %.

Core-Section-Sample	La2O3	UO2	ThO2	PbO	Y2O3	Ce2O3	CaO	P2O5	Nd2O3	SO3	SiO2	Sm2O3	Pr2O3	Gd2O3	Dy2O3	FeO	Total
MH1-11-1	12.79	0.84	4.02	0.16	2.27	28.47	1.35	32.68	11.57	0.01	0.23	2.23	2.67	1.60	0.55	2.83	104.26
MH1-11-1	14.58	0.47	1.38	0.06	1.60	31.91	0.54	30.52	12.36	0.02	0.14	1.88	3.12	1.26	0.32	2.81	102.96
MH1-11-3	12.65	0.40	3.39	0.10	1.49	28.50	0.85	26.23	11.94	0.02	0.24	1.03	3.15	1.27	0.29	7.49	99.04
MH2-15a-1	14.40	0.33	2.28	0.06	1.08	28.29	4.87	29.79	11.68	0.35	0.16	1.69	3.05	0.95	0.04	5.21	104.22
MH2-15a-10	12.91	0.67	2.71	0.08	1.05	26.05	1.46	24.98	10.86	0.73	2.91	2.12	2.73	1.11	0.46	0.36	91.19
MH2-15a-6	14.26	0.23	2.65	0.08	1.07	28.54	0.74	26.59	11.87	0.66	1.51	1.88	2.99	1.32	0.09	1.34	95.82
MH2-15a-7	14.17	0.21	3.19	0.09	1.33	29.08	1.09	29.91	12.16	0.48	0.45	2.12	2.84	1.37	0.17	0.92	99.58
MH2-15a-8	13.96	0.11	1.27	0.05	0.84	27.00	1.21	25.17	10.56	0.98	6.16	1.47	2.70	0.59	0.21	1.86	94.16
MH2-15a-9	14.94	0.12	2.37	0.06	0.81	30.11	1.46	29.06	12.37	1.94	0.83	1.48	3.25	0.66	0.00	1.60	101.07
MH2-17-11a	14.24	0.68	2.59	0.10	1.49	27.68	0.77	29.71	11.16	0.00	1.72	1.95	2.72	1.00	0.69	0.42	96.92
MH2-17-11b	11.47	0.15	1.87	0.05	1.06	29.03	1.52	29.79	14.63	1.01	0.26	2.81	3.25	1.04	0.48	0.21	98.65
MH2-17-12	13.60	0.58	2.40	0.10	1.42	26.72	0.65	30.90	10.54	0.01	0.86	1.94	2.78	1.15	0.35	0.22	94.23
MH2-17-13	13.95	0.22	3.22	0.07	1.25	27.75	1.30	27.58	11.47	0.08	1.42	2.33	2.84	1.16	0.54	0.75	95.93
MH2-17-17	14.22	0.27	3.15	0.09	1.56	28.54	1.19	30.95	11.48	0.03	0.28	2.23	2.76	1.34	0.02	0.44	98.55
MH2-17-18	14.50	0.52	2.23	0.08	1.41	27.34	0.60	28.73	11.07	0.03	2.72	2.08	2.89	1.07	0.37	0.66	96.30
MH2-17-19	14.14	0.23	3.82	0.08	0.89	27.44	2.27	28.56	11.04	0.27	2.23	1.92	2.86	0.78	0.34	0.32	97.20
MH2-17-22	14.88	0.43	3.31	0.10	1.41	27.68	0.74	29.70	11.34	0.02	0.86	2.45	2.82	1.22	0.42	0.41	97.76
MH2-17-23b	13.75	0.38	3.21	0.09	1.42	27.50	0.70	28.56	11.79	0.02	1.16	2.37	2.97	1.24	0.31	0.33	95.79
MH2-17-24	12.91	0.60	2.64	0.09	1.44	26.45	0.65	29.17	10.93	0.05	4.09	2.18	2.77	0.92	0.42	0.37	95.69
MH2-17-25	14.43	0.28	2.93	0.07	1.24	27.61	0.85	29.33	11.23	0.11	2.83	2.15	2.75	1.01	0.30	0.41	97.53
MH2-17-2a	14.35	0.45	2.88	0.09	1.33	27.80	0.84	28.90	10.91	0.07	0.84	2.17	2.73	1.31	0.75	0.33	95.76
MH2-17-2b	14.23	0.45	3.22	0.09	1.33	26.59	0.76	28.56	10.86	0.07	3.16	2.28	2.75	1.10	0.43	0.36	96.22
MH2-17-3a	14.48	0.35	3.15	0.09	1.40	28.37	0.68	29.79	11.83	0.04	0.38	2.31	2.88	1.37	0.49	0.24	97.84
MH2-17-3b	14.57	0.41	3.49	0.10	1.51	28.58	0.81	29.86	11.52	0.02	0.15	2.49	2.96	1.06	0.16	0.12	97.80
MH2-17-5.5a	14.26	0.45	2.62	0.08	1.17	26.97	0.91	27.66	10.83	0.04	3.46	2.10	2.79	1.28	0.58	0.45	95.65
MH2-17-5.5b	14.60	0.45	2.91	0.08	1.27	28.39	0.72	29.28	12.02	0.06	1.31	2.07	2.92	1.36	0.44	0.41	98.28

Core-Section-Sample	La2O3	UO2	ThO2	PbO	Y2O3	Ce2O3	CaO	P2O5	Nd2O3	SO3	SiO2	Sm2O3	Pr2O3	Gd2O3	Dy2O3	FeO	Total
MH2-17-5b	14.70	0.24	2.72	0.07	1.26	27.68	0.77	31.63	11.55	0.19	1.63	2.37	2.93	0.91	0.70	0.32	99.67
MH2-17-5c	14.08	0.39	2.58	0.07	1.10	25.76	0.62	29.36	10.01	0.12	6.04	1.60	2.63	0.81	0.40	0.43	96.01
MH2-17-9a	14.65	0.41	1.99	0.07	1.24	28.27	0.50	29.12	11.44	0.03	2.59	2.09	2.89	0.83	0.34	0.30	96.76
MH2-17-9b	14.64	0.37	2.07	0.07	1.34	28.59	0.81	29.62	11.61	0.06	1.24	2.27	3.07	1.07	0.00	0.31	97.13
MH2-17-Unk	15.85	0.32	2.72	0.08	1.06	27.77	0.68	28.44	10.28	0.09	4.91	1.96	2.39	0.83	0.19	0.54	98.10

Table A18 shows the calculated dates using Reno's (2009) date equation as well as the associated error, the grain's mineralogical associations, and grain size.

Core-Section-Sample	Date	Error	Approx. Size (µm)	Notes
MH1-11-1	519	16	10x10	Inclusion in magnetite
MH1-11-1	459	20	10x10	Inclusion in magnetite
MH1-11-3	664	50	5x8	Inclusion in magnetite
MH2-15a-1	475	33	5x5	Inclusion in magnetite
MH2-15a-10	106	16	5x8	In muscovite matrix
MH2-15a-6	455	61	5x5	Inclusion in degraded tourmaline
MH2-15a-7	333	42	5x8	Inclusion in tourmaline
MH2-15a-8	474	23	5x5	In degraded tourmaline
MH2-15a-9	522	29	5x8	Inclusion in tourmaline core
MH2-17-11a	1510	34	15x8	In muscovite matrix
MH2-17-11b	492	28	15x8	In muscovite matrix
MH2-17-12	395	20	12x8	In muscovite near ilmenite
MH2-17-13	583	47	8x8	Inclusion in epidote in muscovite matrix
MH2-17-17	455	33	8x8	Inclusion in epidote in muscovite matrix
MH2-17-18	318	14	8x5	In muscovite matrix near magnetite and chlorite
MH2-17-19	312	15	5x5	In muscovite matrix
MH2-17-22	211	7	10x10	In muscovite grain bordering ilmenite
MH2-17-23b	367	103	12x8	In degraded muscovite matrix
MH2-17-24	537	29	12x5	In degraded muscovite matrix
MH2-17-25	2932	NA	12x10	In muscovite matrix
MH2-17-2a	554	26	15x10	In muscovite matrix
MH2-17-2b	112	64	15x10	In muscovite matrix
MH2-17-3a	367	20	15x10	In muscovite matrix
MH2-17-3b	1479	81	15x10	In muscovite
MH2-17-5.5a	669	56	12x8	In muscovite grain near ilmenite; proximal to monazite 5
MH2-17-5.5b	2500	NA	12x8	In muscovite matrix bordering ilmenite
MH2-17-5b	707	52	20x8	In muscovite matrix adjacent to ilmenite
MH2-17-5c	399	63	20x8	In muscovite matrix near ilmenite
MH2-17-9a	1034	17	12x8	In muscovite matrix
MH2-17-9b	1448	37	12x8	In muscovite matrix
MH2-17-Unk	1841	153	10x8	In degraded muscovite matrix

Figure A1 shows the monazites analyzed from MH1-11. As with Figure 4.12, blue analyses are monazites that were analyzed but did not yield good data, and red analyses are monazites that yielded useable data. The matrix is primarily muscovite, epidote, quartz, chlorite, and plagioclase with minor garnet. The opaque phases include magnetite, chalcopyrite, and ilmenite. Trace zircon and apatite are also present. Tourmaline from this sample appears small and homogeneous under both reflected light and backscattered electron imaging.



Figure A2 illustrates the distribution of monazite grains on sample MH2-15a. As with Figure 4.12, blue analyses are monazites that were analyzed but did not yield good data, and red analyses are monazites that yielded useable data. The green pods represent aggregated tourmaline, and the pod's matrix is intergrown tourmaline and chlorite. The matrix of the sample is composed of muscovite, epidote, chlorite, and talc with trace biotite. The opaque phases include magnetite and ilmenite.



Bibliography:

Ahmed, A H, Arai, S., and Ikenne, M., 2009, Mineralogy and Paragenesis of the Co-Ni Arsenide Ores of Bou Azzer, Anti-Atlas, Morocco: *Economic Geology*. 104.2: 249-266.

Aleinikoff, J.N., Horton, J.W., Jr., Drake, A.A., Jr., and Fanning, C.M., 2002, Shrimp and U-Pb ages of Ordovician granites and tonalites in the central Appalachian Piedmont; Implications for Paleozoic tectonic events: *American Journal of Science*, v. 302, p. 50–75.

Auclair, M, Gauthier, M., Trottier, J., Jebrak, M., and Chartrand, F., 1993, Mineralogy, Geochemistry, and Paragenesis of the Eastern Metals Serpentinite-Associated Ni-Cu-Zn Deposit, Quebec Appalachians: *Economic Geology*. v. 88.1, p. 123-138.

Ayers, J.C., Miller, C.F., Gorisch, B., Milleman, J., 1999, Textural development of monazite during high-grade metamorphism: hydrothermal growth kinetics, with implications for U, Th–Pb geochronology: *American Mineralogist*, v. 84, p. 1766–1780.

Bailey, S.W., 1988, Chlorites: Structures and crystal chemistry: *Mineralogical Society of America, Reviews in Mineralogy*, v. 19, p. 347-403.

Barrie, C.T., and Hannington, M.D., 1999, Classification of volcanic-associated massive sulfide deposits based on host-rock composition, in Barrie, C.T., and Hannington, M.D., eds., *Volcanic-associated massive sulfide deposits— Processes and examples in modern and ancient settings: Reviews in Economic Geology*, v. 8. p. 1–11.

Berndt, M. E., and Seyfried, W. E., 1990, Boron, bromine, and other trace elements as clues to the fate of chlorine in mid-ocean ridge vent fluids: *Geochimica et Cosmochimica Acta*, v. 54, p. 2235-2245.

Bischoff, J. L., and Rosenbauer, R. J., 1988, Liquid-vapor relations in the critical region of the system NaCl-H₂O from 380 to 415 C: A refined determination of the critical point and two-phase boundary of seawater: *Geochimica et Cosmochimica Acta*, v.52, p.2121-2126.

Burke, T. M., 1987, The petrology and chemistry of detrital ultramafic material at the Mineral Hill mine, Sykesville mining district, Maryland, and the role of accessory chromite in determining the origin of the body and associated sulfide ores: Unpublished M.Sc. thesis, Maryland, United States, University of Maryland, 187 p.

Candela, P.A., Piccoli, P.M., Wylie, A.G. and Wilks, M., 2015, The Historic Sykesville Ultramafic Rock-Associated, Fe-Cu-Co-Zn-Ni Mineral District: Drill Core and Mine Dump: *Society of Economic Geologists Field Trip Guide #* (in press), 16 p.

Candela, P. A., Wylie, A. G., and Burke, T. M., 1989, Genesis of the ultramafic rock-associated Fe-Cu-Co-Zn-Ni deposits of the Sykesville District, Maryland Piedmont:

Economic Geology and the Bulletin of the Society of Economic Geologists, v. 84.3, p. 663-675.

Cherkashev, G.A., Ivanov, V.N., Bel'tenev, V.I., Lazareva, L I., Rozhdestvenskaya, I.I., Samovarov, M.L., Poroshina, I.M., Sergeev, M.B., Stepanova, T.V., Dobretsova, I.G., Kuznetsov V.Y., 2013, Massive sulfide ores of the northern equatorial Mid-Atlantic Ridge: *Oceanology*, v. 53, p. 607-619.

Cox, D.P., and Singer, D.A., 1986, Mineral deposit models: U.S. Geological Survey Bulletin 1693, 379 p.

Dick, H. J. B., Tivey, M. A., and Tucholke, B.E., 2008, Plutonic foundation of a slow-spreading ridge segment: Oceanic core complex at Kane Megamullion, 23°30'N, 45°20'W: *Geochemistry, Geophysics, Geosystems*, v. 9.

Dobbe, R.T.M., 1991, Tellurides, selenides, and associated minerals in the Tunaberg copper deposits, SE Bergslagen, central Sweden: *Mineralogy and Petrology*, v. 44, p. 89-106.

Drake, A.A., Jr., 1989, Metamorphic rocks of the Potomac Terrane in the Potomac Valley of Virginia and Maryland: 28th International Geological Congress Field Trip Guidebook T202, Washington, D.C., American Geophysical Union, Washington, D.C., 22 p.

Drake, A, and Lyttle, P., 1981, The Accotink Schist, Lake Barcroft Metasandstone, and Popes Head Formation—Keys to an Understanding of the Tectonic Evolution of the Northern Virginia Piedmont, in U. S. Geological Survey Professional Paper 1205, Washington D.C., U.S.

Drake, A., and Morgan, B., 1981, The Piney Branch Complex: a metamorphosed fragment of the central Appalachian, ophiolite in northern Virginia: *American Journal of Science*, v. 281, p. 484-508.

Dutrow, B. L., and Henry, D. J., 2011, Tourmaline: a geologic DVD: *Elements*, v. 7, p. 301-306.

Evans, K. V., Nash, J. T., Miller, W. R., Kleinkopf, M. D., & Campbell, D. L., 1995, Blackbird Co—Cu deposits: U.S. Geol. Survey Open-File Rep. 95–831, 145–151

Flowers, R.M., Bowring, S.A., Tulloch, A.J., Klepeis, K.A., 2005, Tempo of burial and exhumation within the deep roots of a magmatic arc, Fiordland, New Zealand: *Geology*, v.33, p. 17-20.

Foose, M., Economou, M., Panayiotou, A., 1985, Compositional and mineralogic constraints on the genesis of ophiolite hosted nickel mineralization in the Pevkos area, Limassol Forest, Cyprus: *Mineralium Deposita*, v.20, p. 234-240.

Fouquet, Y., Cambon, P., Etoubleau, J., Charlou, J. L., Ondréas, H., Barriga, F. J. A. S., Cherkashov, G., Semkova, T., Poroshina, I., Bohn, M., Donval, J. P., Henry, K., Murphy, P. and Rouxel, O., 2010, Geodiversity of Hydrothermal Processes Along the Mid-Atlantic Ridge and Ultramafic-Hosted Mineralization: a New Type Of Oceanic Cu-Zn-Co-Au Volcanogenic Massive Sulfide Deposit, in Diversity of Hydrothermal Systems on Slow Spreading Ocean Ridges (eds P. A. Rona, C. W. Devey, J. Dymant and B. J. Murton): American Geophysical Union, Washington, D. C.

Franklin, J.M., Gibson, H.L., Jonasson, I.R., and Galley, A.G., 2005, Volcanogenic massive sulfide deposits, in Hedenquist, J.W., Thompson, J.F.H., Goldfarb, R.J., and Richards, J.P., eds., Economic Geology 100th anniversary volume, 1905– 2005: Littleton, Colo., Society of Economic Geologists, p. 523–560.

Franklin, J.M., Lydon, J.M., and Sangster, D.F., 1981, Volcanic-associated massive sulfide deposits, in Skinner, B.J., ed., Economic Geology 75th anniversary volume, 1905–1980: Littleton, Colorado, The Economic Geology Publishing Company, p. 485–627.

Gale, A. and Minarik, W.G., 2005, Soldier's Delight and the Baltimore Mafic Complex: Tectonic clues from osmium isotopes: Geological Society of America Abstracts with Programs, v. 36 (26-7).

Galley, A.G., Hannington, M.D., and Jonasson, I.R., 2007, Volcanogenic massive sulphide deposits, in Goodfellow, W.D., ed., Mineral Deposits of Canada: A Synthesis of Major Deposit-Types, District Metallogeny, the Evolution of Geological Provinces, and Exploration Methods: Geological Association of Canada Special Publication No. 5, p. 141-161.

Gibson, H. L., Allen, R. L., Riverin, G., & Lane, T. E. (2007). The VMS model: advances and application to exploration targeting: Exploration, v. 7, p. 713-730.

Hawthorne, F.C., Henry, D.J., 1999, Classification of the minerals of the tourmaline group: European Journal of Mineralogy, v. 11, p. 201–215.

Henry, D.J., Guidotti, C.V., 1985, Tourmaline as a petrogenetic indicator mineral: an example from the staurolite-grade metapelites of NW Maine: American Mineralogist, v. 70, p. 1–15.

Henry, D.J., Dutrow, B.L., 2012, Tourmaline at diagenetic to low-grade metamorphic conditions: Its petrologic applicability: Lithos, v. 154, p. 16-32.

Henry, D.J., Dutrow, B.L., 1996, Metamorphic tourmaline and its petrologic applications, in: E.S. Grew, L.M. Anovitz (Eds.), Boron: Mineralogy, Petrology and Geochemistry, Reviews in Mineralogy: v. 33, p. 503–557.

Herrington, R., Maslennikov, V., Zaykov, V., Seravkin, I., Kosarev, A., Buschmann, B., Oregeval, J. J., Holland, N., Tesalina, S., Nimis, P., Armstrong R., 2005, Classification of VMS deposits: lessons from the South Uralides: *Ore Geology Review*, v. 27, p. 203–237.

Herrington, R.J., Maslennikov, V.V., Spiro, B., Zaykov V.V., Little C.T.S., 1998, Ancient vent chimney structures in the Silurian massive sulphides of the Urals: Geological Society, London, Special Publications, v. 148, p. 241-257.

Hey, M. H., 1954, A new review of the chlorites: *Mineral Magazine*, v. 30, p.277-292.

Heyl, A., and Pearre, N., 1965, Copper, zinc, lead, iron cobalt and barite deposits of the Piedmont Upland in Maryland: Maryland Geological Survey, Bulletin 28, p. 37-38.

Hezel, D.C., Kalt, A., Marschall, H.R., Ludwig, T., Meyer H.P., 2011, Major-element and Li, Be compositional evolution of tourmaline in an S-type granite–pegmatite system and its country rocks: an example from Ikaria, Aegean Sea, Greece: *The Canadian Mineralogist*, v. 49, p. 321–340.

Horton, J.W, Aleinikoff, J. N., Drake, A. A., and Fanning C. M., 2010, Ordovician Volcanic-Arc Terrane in the Central Appalachian Piedmont of Maryland and Virginia: Shrimp U-Pb Geochronology, Field Relations, and Tectonic Significance: *Memoir*, p. 621-660.

Hronsky, J.M., and Groves, D.I., 2008, Science of targeting: definition, strategies, targeting and performance measurement: *Australian Journal of Earth Sciences*, v. 55, p. 3-12.

Hutchinson, R.W., 1973, Volcanogenic sulfide deposits and their metallogenic significance: *Economic Geology*, v. 68, p. 1223–1246.

Ildefonse, B., Blackman, D. K., John, B. E., Ohara, Y., Miller, D. J., MacLeod, C. J., 2007, Oceanic core complexes and crustal accretion at slow-spreading ridges: *Geology*, v. 35, p.623–626.

Jolly, J. L., van Heyl, A., 1968, Mercury and other trace elements in sphalerite and wallrocks from central Kentucky, Tennessee, and Appalachian zinc districts: *US Geological Survey Bulletin* 1252-F.

Kaliwoda, M., Marschall, H.R., Marks, M.A.W., Ludwig, T., Altherr, R., Markl G., 2011, Boron and boron isotope systematics in the peralkaline Ilimaussaq intrusion (South Greenland) and its granitic country rocks: a record of magmatic and hydrothermal processes: *Lithos*, v. 125, p. 51–64.

Kohn, M.J., and Malloy, M.A., 2004, Formation of monazite via prograde reactions among common silicates: implications for age determinations: *Geochimica et Cosmochimica Acta*, v. 68, p. 101–113.

- Kunk, M. J, Wintsch, R. P., Naeser, C. W., Naeser, N. D., Southworth, C. S., Drake, A. A., and Becker J. L., 2005, Tectonics - Contrasting Tectonothermal Domains and Faulting in the Potomac Terrane, Virginia-Maryland -- Discrimination by $^{40}\text{Ar}/^{39}\text{Ar}$ and Fission-Track Thermochronology: Geological Society of America Bulletin, v. 117.9, p. 1347.
- Large, R. R., 1992, Australian volcanic-hosted massive sulfide deposits; features, styles, and genetic models: Economic Geology, v. 87, p. 471-510.
- Mosier, D.L., Berger, V.I., and Singer, D.A., 2009, Volcanogenic massive sulfide deposits of the world—Database and grade and tonnage models: U.S. Geological Survey Open- File Report 2009–1034, 50 p.
- Leeman, W.P., and Sisson, V.B., 1996, Geochemistry of boron and its implications for crustal and mantle processes: Reviews in Mineralogy, v. 33, p. 645-707.
- Marques, A. F. A., Barriga, F. J. A. S., Chavagnac, V. E., & Fouquet, Y., 2006, Mineralogy, geochemistry, and Nd isotope composition of the Rainbow hydrothermal field, Mid-Atlantic Ridge: Mineralium Deposita, v. 41, p. 52-67.
- Muller, P. D., Candela, P. A., Wylie, A. G., 1989, Liberty Complex; polygenetic mélange in the central Maryland Piedmont: Geological Society of America Special Papers, v. 228, p. 113-134.
- Nold, J.L., 1990, The Idaho Cobalt Belt, Northwestern United States: a Metamorphosed Proterozoic Exhalative Ore District: Mineralium Deposita. v. 25.3.
- Pavlidis, L., 1981, The central Virginia volcanic-plutonic belt: an island arc of Cambrian age: United States Geological Survey Professional Paper 1231-A, p. A1-A34.
- Pavlidis, L., 1989, Early Paleozoic composite mélange terranes, central Appalachian Piedmont, Virginia and Maryland: its origin and tectonic history: Geological Society of America Special Paper, v. 228, p. 135–193.
- Peltola, E., 1978, Origin of Precambrian Copper Sulfides of the Outokumpu District, Finland: Economic Geology, v. 73.4, p.461-477.
- Peltonen, P, Kontinen, A., Huhma, H., and Kuronen, U., 2008, Outokumpu Revisited: New Mineral Deposit Model for the Mantle Peridotite-Associated Cu-Co-Zn-Ni-Ag-Au Sulphide Deposits: Ore Geology Reviews, v. 33, p. 559-617.
- Peter, J., 1999, Windy Craggy, northwestern British Columbia: the world's largest Besshi-type deposit: Reviews in Economic Geology, v. 8, p. 261-295.

Reno, B.L., Piccoli, P.M., Brown, M., 2009, Timing of Orogenesis in the Southern Brasilia Belt: Unpublished PhD dissertation, College Park, Maryland, The University of Maryland, 289 p.

Reno, B.L., Piccoli, P.M., Brown, M. & Trouw, R., 2012, In situ chemical dating of monazite from the Southern Brasilia Belt, Brazil: *Journal of Metamorphic Geology*, v. 30, p. 81–112.

Rudnick, R. L., and Gao, S., 2003, Composition of the continental crust: *Treatise on geochemistry*, p. 1-64.

Sawkins, F.J., 1976, Massive sulphide deposits in relation to geotectonics, in Strong, D.F., ed., *Metallogeny and plate tectonics: Geological Association of Canada, Special Paper 14*, p. 221–240.

Sangster, D., and Scott, S.D., 1976, Precambrian strata-bound massive Cu-Zn-Pb sulfide ores of North America, in Wolf, K.H., ed., *Handbook of strata-bound and stratiform ore deposits: Amsterdam, Elsevier*, p. 129–222.

Schandl, E.S. and Gorton, M.P., 2004, A textural and geochemical guide to the identification of hydrothermal monazite: criteria for selection of samples for dating epigenetic hydrothermal ore deposits: *Economic Geology*, v. 99, p. 1027-1038.

Schoenborn, W.A., 2002, Conditions of deformation in the Mather Gorge and Sykesville Formations, Potomac River, SW Maryland and N Virginia: *Geological Society of America Abstracts with Programs*, v. 34.1, p. A–19.

Schwartz, M., 2000, Cadmium in Zinc Deposits: Economic Geology of a Polluting Element: *International Geology Review*, v.42:5, p.445-469.

Shanks, W.C. P., and Koski, R.A., 2012, Introduction in volcanogenic massive sulfide occurrence model: U.S. Geological Survey Scientific Investigations Report 2010–5070–C, p. 4.

Shanks, W.C. P., and Thurston, R., 2012, Volcanogenic massive sulfide occurrence model: U.S. Geological Survey Scientific Investigations Report 2010–5070—C, p. 345.

Slack, J.F., Coad, P.R., 1989, Multiple hydrothermal and metamorphic events in the Kidd Creek volcanogenic massive sulphide deposit, Timmins, Ontario: Evidence from tourmalines and chlorites: *Canadian Journal of Earth Science*, v. 26, p. 694-715.

Slack, J.F., 1996, Tourmaline associations with hydrothermal ore deposits. in: E.S. Grew, L.M. Anovitz (Eds.), *Boron: Mineralogy, Petrology and Geochemistry, Reviews in Mineralogy*, v. 33, p. 559–644.

- Slack, J.F., and Trumbull, R., 2011, Tourmaline as a Recorder of Ore-Forming Processes: Elements, v. 7, p. 321-326.
- Smith, D K., Cann, J.R., Escartin, J., 2006, Widespread active detachment faulting and core complex formation near 13° N on the Mid-Atlantic Ridge,” Nature, v. 443, p. 440–444.
- Spear, F.S., and Pyle, J. M., 2010, Theoretical modeling of monazite growth in a low-Ca metapelite: Chemical Geology, v. 273, p. 111–119.
- Southworth, S., and Burton, W. C., 2004, Geology of the National Capital Region: Field Trip Guidebook. Reston, Va: U.S. Dept. of the Interior, U.S. Geological Survey.
- Southworth, S., Drake, A. A., Brezinski, D. K., Wintsch, R. P., Kunk, M. J., Aleinikoff, J. N., and Naeser, N. D., 2006, Central Appalachian Piedmont and Blue Ridge tectonic transect, Potomac River corridor: Geological Society of America Field Guides 8, p. 135-167.
- Stepanova, T.V., Krasnov, S.G., Cherkashev, G.A., 1996, Mineralogy, chemical composition and structure of the MIR Mound, TAG Hydrothermal Field, Geophysical Research Letters, V. 23, p. 3515–3518.
- Taylor, C.D., Zierenberg, R.A., Goldfarb, R.J., Kilburn, J.E., Seal II, R.R., and Kleinkopf, M.D., 1995, Volcanogenic Massive Sulfide Deposits: Preliminary compilation of descriptive geoenvironmental mineral deposit models, p. 137-145.
- van Hinsberg, V.J., Henry, D.J., Dutrow, B.L., 2011(a), Tourmaline as a petrologic forensic mineral; a unique recorder of its geologic past: Elements, v. 7, p. 327-332.
- van Hinsberg, V.J., Henry, D.J., Marschall, H.R., 2011(b), Tourmaline: an ideal indicator of its host environment: The Canadian Mineralogist, v. 49, p. 1-16.
- Vils, F., Muntener, O., Kalt, A., Ludwig T., 2011, Implications of the serpentine phase transition on the behaviour of beryllium and lithium–boron of subducted ultramafic rocks: Geochimica et Cosmochimica Acta, v. 75, p. 1249–1271.
- Weisbrod, A., Polak, C., and Roy, D., 1986, Experimental study of tourmaline solubility in the system Na-Mg-Al-Si-BOH: applications to the boron content of natural hydrothermal fluids and tourmalinization processes: Int Symp Exp Miner Abstr, v. 1, p. 140-141.
- Wing, B.A., Ferry, J.M., Harrison, M., 2003, Prograde destruction and formation of monazite and allanite during contact and regional metamorphism of pelites: petrology and geochronology. Contributions to Mineralogy and Petrology, v. 145, p. 228–250.

Wintsch, R.P, Mulvey, B.K., Kunk M. J., and Southworth C.S., 2010, $^{40}\text{Ar}/^{39}\text{Ar}$ Dating of Silurian and Late Devonian Cleavages in Lower Greenschist-Facies Rocks in the Westminster Terrane, Maryland, USA: Bulletin of the Geological Society of America, v. 122, p. 658-677.

Wylie, A. G., Candela, P. A., and Burke, T. M., 1987, Compositional zoning in unusual Zinc-rich chromite from the Sykesville district, Carroll Co., Maryland: American Mineralogist, v. 72, p. 413- 422.

Zaykov, V.V., Zaykova, E.V., Maslennikov, V.V., 2000, Volcanic complexes and ore mineralization in spreading basins of the southern Urals. In: Mezhelovsky, N.V., Morozov, A.F., Gusev, G.S., Popov, V.S. (Eds.), Geodynamics and Metallogeny: Theory and Implications for Applied Geology. Ministry of Natural Resources of the RF and GEOKART Ltd., Moscow, p. 315–337.